ABSTRACT

Title of dissertation: CONTROL PROTOCOLS FOR MANIPULATION OF GROUND-STATE QUANTUM BEATS IN A CAVITY QED SYSTEM

Andrés David Cimmarusti, Doctor of Philosophy, 2014

Dissertation directed by: Professor Luis A. Orozco
Department of Physics

Cavity quantum electrodynamics (QED) captures the essential interaction between two quantum systems, an atom (for example) and the quantized electromagnetic field. The cavity reduces the plethora of spatial modes of the field in free-space to one or two. This simplification facilitates the study and control of atom-light interactions. In this thesis we show results where we control both aspects of the interaction.

Our first measurements demonstrate the implementation of a simple feedback mechanism on a two-mode cavity QED system to preserve the Zeeman coherence of a ground state superposition that generates quantum beats. Our investigation shows how to prevent a shift away from the Larmor frequency and associated decoherence caused by Rayleigh scattering. The protocol consists of turning off the drive of the system after the detection of a first photon and letting it evolve in the dark. Turning the drive back on after a pre set time reveals a phase accumulated only from Larmor precession, with the amplitude of the quantum beat more than a factor of two larger

than with continuous drive.

We present preliminary conditional measurements in a new cavity QED apparatus that show an environment-assisted speed-up of the evolution of our cavity photon state under weak driving. Changes in the number of atoms (N) that can couple to the field is our way of tailoring the environment. Our results indicate that as N increases, the rate of the re-population of the cavity photon state increases.

CONTROL PROTOCOLS FOR MANIPULATION OF GROUND-STATE QUANTUM BEATS IN A CAVITY QED SYSTEM.

by

Andrés David Cimmarusti

Dissertation submitted to the Faculty of the Graduate School of the
University of Maryland, College Park in partial fulfillment
of the requirements for the degree of
Doctor of Philosophy
2014

Advisory Committee:
Professor Luis A. Orozco, Chair/Advisor
Professor Steve L. Rolston
Professor James V. Porto
Professor Gretchen Campbell
Professor Edo Waks

Dedication

Dedicato alla memoria di mia nonna Rosa y a la de mi abuela Teresa

Acknowledgments

My family played a pivotal role in my education. I am grateful to have parents that understood its value and encouraged me. Their loving support made my trips home a period of joy and much needed balance in my life. This balance would not have been possible without the constant support and affection of Maya. It strengthened my resolve during these years and our travels and future plans always kept my mind looking forward.

I have enjoyed the friendship and advice from many friends and fellow graduate students. Among them Jon, Jiehang, Matt, Prem, Misha, Samantha, Wanderson, María Gabriela, Héctor, Jeff and lately a contingent of Latinos: Pablo, Ale, Ana, Dalia, Paco and David. They have all in their way enriched my life and experience at Maryland.

The collective effort that went into this thesis can be difficult to allocate and quantify, but I will give it a try. I owe a great deal to my advisor, Professor Luis Orozco. His indefatigable love for all aspects of science always marked our conversations and instilled a sense of purpose in me. Throughout the years he patiently helped me understand the physics and other technical aspects of our experiment (and beyond!).

I thank Professors Pablo Barberis-Blostein and Howard Carmichael for their continued interest in the project. Their theoretical support and key insights into the physics have been invaluable and have kept us always looking ahead.

The project has been active for many years. The first incarnation was brought

to life by Matt Terraciano and left into the hands of Rebecca Olson Knell, Jietai Jing and David Norris, my former labmate, who taught me how to run “things”. Other key present and past members include Wanderson Pimenta (who helped me through the long upgrading process), Chris Schroeder, Burkley Patterson (cavity builder and PID man who will take the mantle of graduate student upon my departure), Ana Valdés (cavity builder), Josh Crawford (first cavity builder) and many other visiting summer students. A debt of gratitude goes also to Zhihui Yan and Sebastian Deffner for their recent help and support.

I would like to thank Alexander Franzen for sharing his extensive optical drawings under a Creative Commons Attribution-NonCommercial 3.0 Unported License.

I am grateful to the National Science Foundation. Its continued support of the experiment has made this work possible.

Table of Contents

List of Figures

List of Abbreviations

α	alpha
β	beta
AM	amplitude modulation
AOM	acousto-optic modulator
APC	angled physical contact
APD	avalanche photodiode
AWG	american wire gauge
BEC	Bose-Einstein condensate
CF	ConFlat
DAVLL	dichroic absorption vapor laser lock
DC	direct current
EOM	electro-optic modulator
FC	fiber channel / ferrule connector
FM	frequency modulation
FSR	free spectral range
FWHM	full width at half maximum
HV	high voltage
HWP	half-wave plate
JC	Jaynes-Cummings
JQI	Joint Quantum Institute
LVIS	low-velocity intense source
MOT	magneto-optical trap
NASA	National Aeronautics and Space Administration
NIST	National Institutes of Standards and Technology
NSF	National Science Foundation
PBS	polarizing beam splitter
PCB	Printed-circuit board
PDH	Pound-Drever-Hall
PID	proportional-integral-differential
PM	polarization maintaining
PMT	photomultiplier tube
PZT	piezo-electric transducer
QED	quantum electrodynamics
QWP	quarter-wave plate
Rb	Rubidium
RF	radio frequency
TEM	transverse electromagnetic
TTL	transistor-transistor logic
UHV	ultra-high vacuum

Chapter 1: Quantum beats and cavity QED

1.1 Single-mode cavity QED and two-level atoms

The simplest realization of a cavity quantum electrodynamic system consists of a single material particle coupled to a quantized field. Our work in the optical regime couples Rb atoms and a finite number of modes of the electromagnetic field [1]. These systems have numerous applications in quantum information science [2–5], and also enable the study of quantum optics effects difficult to observe in free space [6–12].

The leading term in the interaction between a radiation field and the atom is the induced electric dipole. Equation 1.1 expresses the coupling constant g associated with the induced dipole moment $\vec{\mu}$.

$$g = \frac{\vec{\mu} \cdot \vec{E}}{\hbar} \tag{1.1}$$

The dipole moment depends on the transition selected, but for electric dipole allowed optical transitions in alkali atoms it is of the order of a few times ea_0 where e is the charge of the electron and a_0 is the Bohr radius. The use of an optical cavity with a small mode volume can increase the coupling constant between the atom and the field. Equation 1.2 gives an expression for the electric field associated with

the energy of a single photon of frequency ω_c coupled to a cavity with spatial mode volume V.

$$E = \sqrt{\frac{\hbar\omega_c}{2\epsilon_0 V}} \tag{1.2}$$

The electric field increases as the Volume V decreases, without actually increasing the number of photons through the intensity of the drive. This opens up the possibility of strong interaction with weak driving, potentially revealing quantum effects in the fluctuations. The resonator itself provides an ideal avenue for detec-

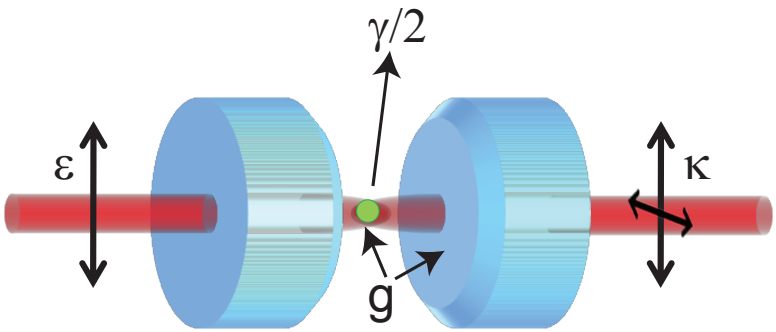

Figure 1.1: Fabry-Perot optical cavity. ε is the drive field, g is the dipole coupling, $\gamma/2$ is the atomic polarization decay rate and κ is the decay rate of the cavity.

tion. In Fig. 1.1, coherent probing of a cavity via vertically polarized light (ε), couples to the atom(s) through the dipole coupling strength g. The spatial mode of the resonator has a finite probability of collecting spontaneous emission, even in the orthogonal polarization that then leaks out at a rate of κ carrying important information encoded in the polarization and the field through their fluctuations.

The Jaynes-Cummings (JC) Hamiltonian is the basic model of choice to describe the interaction between a two-level atom and a mode of the electromagnetic

field, such as the one present inside an optical cavity. It does not include terms for modeling dissipation channels. We write a modified JC Hamiltonian including dissipation and drive for a single-mode optical cavity and and N two-level atoms as in Eq. 1.3 (working in a frame rotating at the frequency of the drive).

$$\begin{aligned} H &= H_0 + H_1 + H_2 + H_3 + H_4 \\ H_0 &= \hbar\omega_a \sum_{j=1}^{N} \sigma_j^z + \hbar\omega_c a^\dagger a \\ H_1 &= i\hbar g \sum_{j=1}^{N} (\sigma_j^+ a - a^\dagger \sigma_j^-) \\ H_2 &= \sum_{j=1}^{N} (\Gamma_A \sigma_j^- + \Gamma_A^\dagger \sigma_j^+) \\ H_3 &= \Gamma_F a^\dagger + \Gamma_F^\dagger a \\ H_4 &= i\hbar\varepsilon(a^\dagger - a) \end{aligned} \tag{1.3}$$

H_0 is the free Hamiltonian. H_1 describes the interaction between field and atoms mediated by g (here we neglect spatial variations of the cavity mode). H_2 is the spontaneous emission of the atoms modeled as a coupling between atom and a reservoir Γ_A. H_3 is the decay of the cavity modeled as a coupling between the field in the cavity and a reservoir Γ_F. H_4 shows a classical driving field ε. The raising and lowering operators of the single mode are $a^\dagger$ and a respectively. The Pauli atomic operators are $\sigma_j^{\pm,z}$. ω_a is the atomic transition frequency and ω_c the frequency of the cavity.

It is not difficult to expand this model to multi-level atoms in a two-mode optical cavity [13], but accurate solutions require numerical methods with photon-number truncation. Certain assumptions allow calculation of a master equation

from Eq. 1.3 (Born and Markov approximations). Tracing over the reservoirs yield non-reversible decays at a rate of γ for the atoms and κ for the cavity mode.

$$\begin{aligned}\frac{d\rho}{dt} =&\varepsilon\left[a^\dagger - a, \rho\right] g\left[a^\dagger J^- - aJ^+, \rho\right] + \kappa\left(2a\rho a^\dagger - a^\dagger a\rho - \rho a^\dagger a\right) \\ &+ \frac{\gamma}{2}\sum_{j=1}^{N}\left(2\sigma_j^-\rho\sigma_j^+ - \sigma_j^+\sigma_j^-\rho - \rho\sigma_j^+\sigma_j^-\right)\end{aligned} \tag{1.4}$$

Equation 1.4 is the master equation we can obtain from the modified JC Hamiltonian of Eq. 1.3. We use the collective raising/lowering operators $J^\pm = \sum_{j=1}^{N}\sigma_j^\pm$.

1.2 Low intensity regime

There is no analytical solution to Eq. 1.4. Two approximate methods are well known. The small noise approximation or the the weak driving approximation [14]. The latter consists of taking $\varepsilon/\kappa \ll 1$.

An expansion of the master equation to powers of ε/κ, leads to the form $\rho = |\psi(t)\rangle\langle\psi(t)|$ where:

$$|\psi(t)\rangle = |0,0\rangle + A_1(t)|1,0\rangle + A_2(t)|0,1\rangle + A_3(t)|2,0\rangle + A_4(t)|1,1\rangle + A_5(t)|0,2\rangle \tag{1.5}$$

The amplitudes A_m obey a set of linear coupled first order differential equations with A_1 and A_2 independent of the rest

$$\begin{aligned}\dot{A}_1 &= -\kappa A_1 + g\sqrt{N}A_2 + \varepsilon \\ \dot{A}_2 &= -\gamma/2A_2 - g\sqrt{N}A_1 \\ \dot{A}_3 &= -2\kappa A_3 + g\sqrt{2N}A_4 + \sqrt{2}\varepsilon A_1 \\ \dot{A}_4 &= -\left(\kappa + \gamma/2\right)A_4 - g\sqrt{2N}A_3 + g\sqrt{2(N-1)}A_5 + \varepsilon A_2 \\ \dot{A}_5 &= -\gamma A_5 - g\sqrt{2(N-1)}A_4\end{aligned} \tag{1.6}$$

The steady state solution to the equations for A_m ($\dot{A}_m = 0$) yields the asymptotic state $|\varphi\rangle$:

$$|\varphi\rangle = |0,0\rangle + \alpha|1,0\rangle + \beta|0,1\rangle + (\alpha^2/\sqrt{2})pq|2,0\rangle + \alpha\beta q|1,1\rangle + (\beta^2/\sqrt{2})qr|0,2\rangle \quad (1.7)$$

with the coefficients:

$$\alpha = \frac{\varepsilon}{\kappa}\frac{1}{1+2C}, \quad \beta = -\sqrt{N}g\frac{\alpha}{\gamma/2} \quad (1.8)$$

and

$$p = 1 - 2C_1', \quad q = \frac{1+2C}{1+2C-2C_1'}, \quad r = \sqrt{1-1/N} \quad (1.9)$$

where $C_1' = C_1/(1+\gamma/2\kappa)$. The concurrent transmission of two photons by the cavity has probability density $|\langle 0,0|a^2|\varphi\rangle|^2 = |\alpha^2 pq|^2$. For a driven cavity ($\alpha \neq 0$) with N atoms, it is possible for the probability density to vanish under certain conditions. This can happen, for example when $p = 0$. This is the signature of non-classical effects such as anti-bunching and sub-poissonian statistics.

The exploration of quantum fluctuations and/or non-classical features of the system yields more insights when looking at photon correlations separated by time τ. The mathematical construct ideal for this task is the second-order intensity correlation function.

1.2.1 Correlation function

The normalized second-order intensity correlation function is generally defined as:

$$g^{(2)}(\tau) = \frac{\langle I(t)I(t+\tau)\rangle}{\langle I(t)\rangle^2} \quad (1.10)$$

Measurements based on Eq. 1.10 include the famous Hanbury-Brown and Twiss proposal for an radio stellar interferometer.

$g^{(2)}(\tau)$ applied to quantum mechanics requires the simple substitution $I \rightarrow a^{\dagger}a$, but we must be careful with the normal and time order of the operators as they act on a quantum state. Under certain conditions $g^{(2)}(\tau)$ will exhibit purely quantum mechanical behavior. A usual example is the anti-bunching $g^{(2)}(0) < 1$ and $g^{(2)}(0) < g^{(2)}(\tau)$ in resonance fluorescence. In this regime, there is suppression of photon emission due to the excited state lifetime.

$$g^{(2)}(\tau) = \frac{\langle \Psi | a^{\dagger}(t) a^{\dagger}(t+\tau) a(t+\tau) a(t) | \Psi \rangle}{\langle \Psi_{SS} | a^{\dagger} a | \Psi_{SS} \rangle^2} \tag{1.11}$$

Eq. 1.11 shows a general expression for a second order correlation function for a quantum system, where $|\Psi\rangle$ is the state of the system and $|\Psi_{SS}\rangle$ the steady state.

Returning to our previous discussion, we can apply Eq. 1.11 to Eqs. 1.5 and 1.7. The system starts in the steady state ($|\Psi\rangle = |\Psi_{SS}\rangle = |\varphi\rangle$). The first photon leaves the cavity at time t causing the collapse of the state (conditional state):

$$|\bar{\varphi}\rangle = \frac{a|\varphi\rangle}{\langle 0,0|a|\varphi\rangle} = |0,0\rangle + \beta q |0,1\rangle + \alpha p q |1,0\rangle \tag{1.12}$$

The detection of the photon projects the system into Eq.1.12. This holds for any photodetection if the system is pure. It represents a good approximation when the rate of photodetection is significantly less than the characteristic rates of the system (γ, κ).

The state evolves a time τ before emitting the second photon. Our $g^{(2)}(\tau)$ is a measure of the probability density of finding a correlated photodetection at time

τ:

$$g^{(2)}(\tau) = |\alpha|^2 \frac{\langle \bar{\varphi}(\tau)|a^\dagger(\tau)a(\tau)|\bar{\varphi}(\tau)\rangle}{\langle \varphi|a^\dagger a|\varphi\rangle^2} = \frac{|\bar{A}_1(\tau)|^2}{|\alpha|^2} \tag{1.13}$$

The evolution of $|\bar{\varphi}(\tau)\rangle$ is governed by Eqs. 1.6, taking the right hand side of Eq. 1.12 as the initial conditions.

The solution to $g^{(2)}(\tau)$ we can express as:

$$g^{(2)}(\tau) = \left(1 + \frac{\Delta\alpha}{\alpha} e^{-\frac{1}{2}(\kappa+\gamma/2)\tau} \left[\cosh \Omega\tau + \frac{1}{2}(\kappa+\gamma/2)\frac{\sinh \Omega\tau}{\Omega}\right]\right)^2 \tag{1.14}$$

with

$$\frac{\Delta\alpha}{\alpha} = -2C_1' \left(\frac{2C}{1+2C-2C_1'}\right) \tag{1.15}$$

and more importantly:

$$\Omega = \sqrt{\frac{1}{4}\left(\kappa - \gamma/2\right)^2 - g^2 N} \tag{1.16}$$

Equation 1.14 shows violation of classical field inequalities, but more importantly for us, it can show photon anti-bunching. The quantum system will undergo vacuum Rabi oscillations when $g^2 N > \frac{1}{4}\left(\kappa - \gamma/2\right)^2$ as it is clear from Eq. 1.16.

$g^{(2)}(\tau)$ are essential for the study of conditional measurements, where the first measurement projects the system into a state and then we let it evolve before measuring again.

1.3 Small noise approximation

In the presence of a large number of atoms and photons, the master equation simplifies to the semi-classical limit, otherwise known as the Maxwell-Bloch equations. For a plane wave ring cavity on resonance with atoms and drive, they are:

$$\begin{aligned}
\frac{dx}{dt} &= -\kappa(x - y - 2CP) \\
\frac{dP}{dt} &= \frac{\gamma}{2}(xD - P) \\
\frac{dx}{dt} &= -\gamma\left[\frac{1}{2}(xP^* + x^*P) + D + 1\right]
\end{aligned} \tag{1.17}$$

Where $x \equiv \langle a \rangle / \sqrt{n_{\text{sat}}}$ is the field inside the cavity with atoms, $y \equiv \langle \varepsilon \rangle / (\kappa\sqrt{n_{\text{sat}}})$ is the field with no atoms, P is the normalized atomic polarization and is proportional to $\langle \sigma_j^- \rangle$. D is the normalized atomic inversion and is proportional to $\langle \sigma_j^z \rangle$ Some important figures of merit that come out Eqs. 1.17 are:

$$n_{\text{sat}} \equiv \frac{\gamma^2}{8g^2} b \tag{1.18}$$

n_{sat} is the saturation photon number. b is the dimensionless effective mode volume and depends of the cavity geometry. For a plane wave ring cavity $b = 1$, but for a Gaussian standing wave $b = 8/3$ [15].

$$C_1 \equiv \frac{g^2}{\kappa\gamma} \tag{1.19}$$

C_1 is the single-atom cooperativity. A similar quantity present in Eq. 1.17 is $C \equiv C_1 N$, the *cooperativity* and N is the number of atoms. The cooperativity gives a measure of the balance between interaction strength and dissipation.

The steady state solution for Eq. 1.17 is known as the state equation.

$$Y = X\left(1 + \frac{2C}{1 + X}\right)^2 \tag{1.20}$$

where $Y = |y|^2$ is the normalized photon number in the cavity without atoms and $X = |x|^2$ is with atoms. The plane wave ring cavity state equation can be simplified

further in the weak driving regime $X \ll 1$.

$$Y = X(1 + 2C)^2 \tag{1.21}$$

Equation 1.21 provides a straightforward way of computing the cooperativity in the cavity if the ratio of photon numbers is known and the system is weakly driven. It is then easy to compute the effective number of atoms in the cavity mode if we know g, κ and γ.

1.4 Two-mode cavity QED and multi-level atoms

The most widely used neutral atomic systems are the alkali metals. Their spectra is relatively simple and their lines are normally within reach of commercially available lasers. They exhibit complex magnetic hyperfine structure. Section 1.1 deals only with two-level atoms. These systems can be prepared by optical pumping techniques, but in this thesis we use the extensive structure available in alkali atoms. The energy level structure of Fig. 1.2 applies to an atom of ^{85}Rb in the presence of a weak magnetic field (linear Zeeman splitting). An effective two-level system is realizable in the structure of Fig. 1.2. The transitions $|F = 3, m_F = 3(-3)\rangle \rightarrow |F' = 4, m_{F'} = 4(-4)\rangle$ serve as two-level systems if the atom can be optically pumped to the initial state and the mode of the cavity is right-σ^+(left-σ^-) circularly polarized. The selection rules only allow transitions and decays between those levels.

Restricting ourselves to the two-level atom approximation neglects the rich physics of the magnetic structure of Fig. 1.2. Ground-state superposition states can have long coherence. We can benefit from the relationship between transitions and

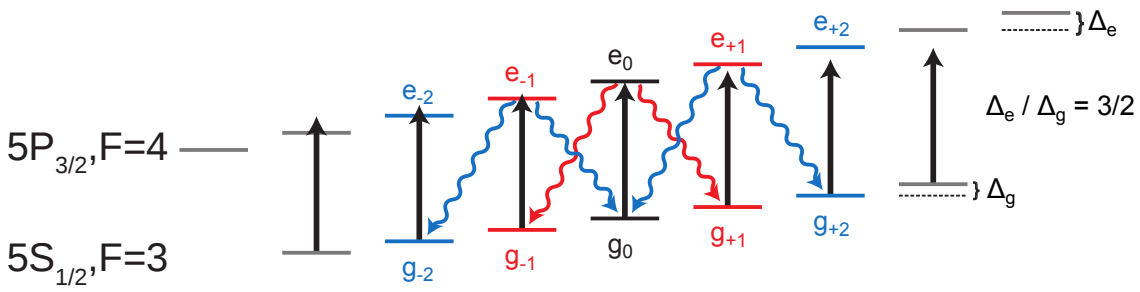

Figure 1.2: $|F = 3, m_F\rangle \rightarrow |F' = 4, m_{F'}\rangle$ transition in the D_2 line of ^{85}Rb with magnetic sublevels.

polarization to explore this rich system, and not just detect the escape of a photon, but also its polarization. Experimentally this entails having great control over the birefringence of the cavity. Figure 1.3 shows a simple photon detection scheme. The driving field, vertically polarized, interacts with a multi-level atom, such as an alkali. After excitation, the atom can undergo different decay paths. The emission of circularly polarized photons ($\sigma^{\pm}$) appear simply as horizontally polarized photons for the detector. This gives us a clear way of distinguishing spontaneously emitted photons from drive photons.

1.5 Conditional quantum beats in a cavity QED system

Our recent work focuses on the long-lived coherences created by spontaneous emission in the ground state [6]. We describe in this section our system and its ground state superpositions.

Our cold atomic beam interacts with the two orthogonal modes of a high

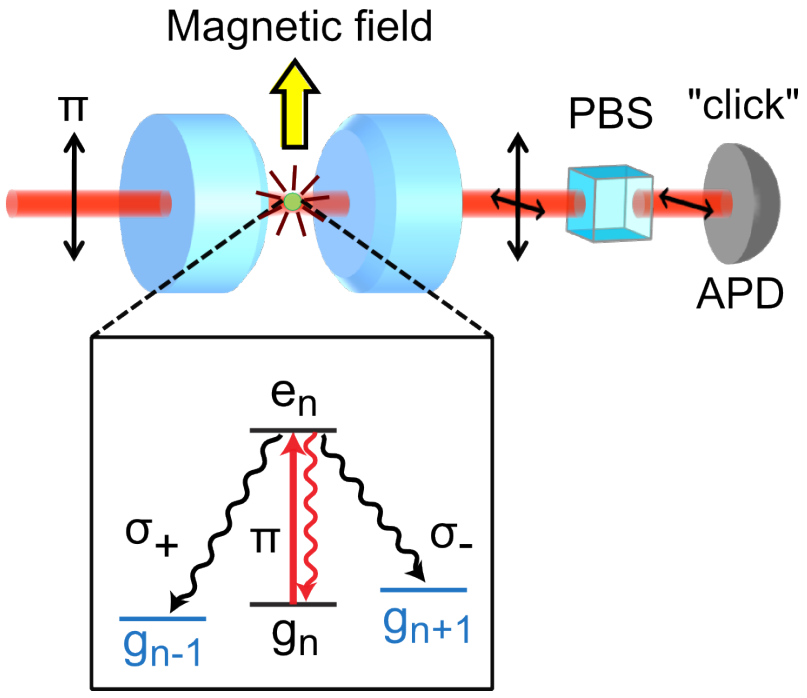

Figure 1.3: Simple photon counting detection scheme using an optical cavity coupled to an atom.

finesse optical cavity. The ^{85}Rb atoms exhibit ground- and excited-state Zeeman structure on the D_2 line with different magnetic g-factors (see Fig. 1.4). The laser drives π (V polarization) transitions, $F = 3, m \rightarrow F = 4, m$, as indicated by the red arrows in the figure. Atomic excitation and decay transfer some of this energy to the orthogonal mode (H polarization). Spontaneous emission generates a long-lived Zeeman superposition in the ground-state (purple and green wavy lines). Its signature is a quantum beat seen in a conditional intensity measurement of the undriven mode. Using the simplified schematic of Fig. 1.4, if an atom enters the cavity in the $m = 0$ ground state, the detection of a photon in the orthogonal mode sets the atom in a superposition of $m = \pm$ ground states. The prepared

superposition then evolves in the magnetic field, acquiring a relative phase, until another π excitation transfers the developed ground-state coherence to the excited state; subsequently, detecting a second (H polarized) photon projects the atom back into its starting state. The sequence overall realizes a quantum eraser [16,17] as the intermediate ground-state is not observed.

Before emitting the second H polarized photon—a σ transition—several intervening π spontaneous emissions (Rayleigh scattering) can occur (orange wavy lines) [18]. Each of these quantum jumps interrupts the atomic dipole and causes a small phase advance on the ground-state coherence, which accumulates over time to become a frequency shift [19]. The accumulated jumps occur randomly in time, so the frequency shift is accompanied by phase diffusion. Eventually, the diffusion dephases the coherence. Of course, a σ spontaneous emission destroys the coherence all in one go for the simplified level structure in Fig. 1.4; not, however, for the considered transition in ^{85}Rb, where there are actually seven rather then three Zeeman sublevels in the ground state.

The diagnostic tool used to understand and modify this spontaneous creation and evolution of ground-state coherence is a conditional measurement of the H-polarized (undriven) mode intensity, i.e., the second-order correlation function $g^{(2)}(\tau)$ of the H-polarized light. Two indistinguishable paths yield "start" and "stop" photons for the measurement: $|g_0\rangle \rightarrow |e_0\rangle \rightarrow |g_+\rangle \rightarrow |e_+\rangle \rightarrow |g_0\rangle$ and $|g_0\rangle \rightarrow |e_0\rangle \rightarrow |g_-\rangle \rightarrow |e_-\rangle \rightarrow |g_0\rangle$. Since the phase advance along each path is different in sign, though equal in magnitude, and the magnitude grows in time, interference between the paths yields oscillations: $g^{(2)}(\tau)$ exhibits a quantum beat at

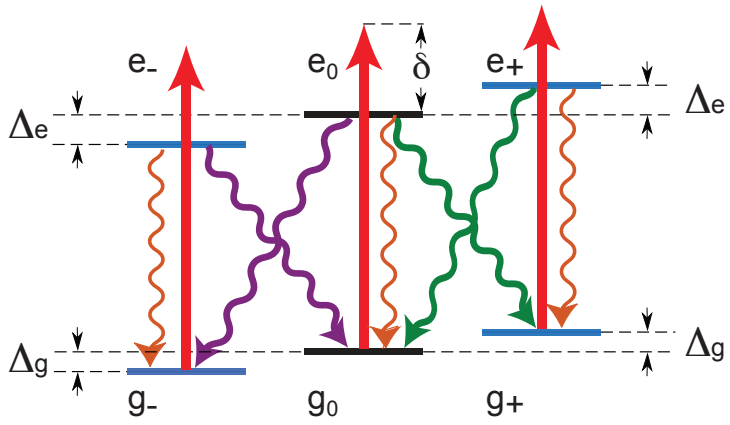

Figure 1.4: Simplified atomic energy level structure of the $F = 3 \rightarrow F = 4$ D_2 line in ^{85}Rb with Zeeman shifts. Different magnetic g-factors yield $\Delta_e > \Delta_g$. Both the π (red and orange) and σ (purple and green) transitions are indicated. We consider only situations with a π drive, which might be detuned by δ.

the Larmor precession frequency or its double.

The difference in time of detection between pairs of photons make up Fig. 1.5. If the two photons come from the same source (single atom) then the contribution is the one-atom interference term (which shows antibunching). If the photons come from different atoms, then we are in the two-atom regime. Both of these terms arise solely from the atoms. The oscillation frequency is $2\Delta_g$. The homodyne term represents the case when one of the photons comes from the driven-mode, while the other comes from the atoms (due to birefringence or deliberate mixing). This causes the beating frequency to decrease to Δ_g (Larmor precession frequency).

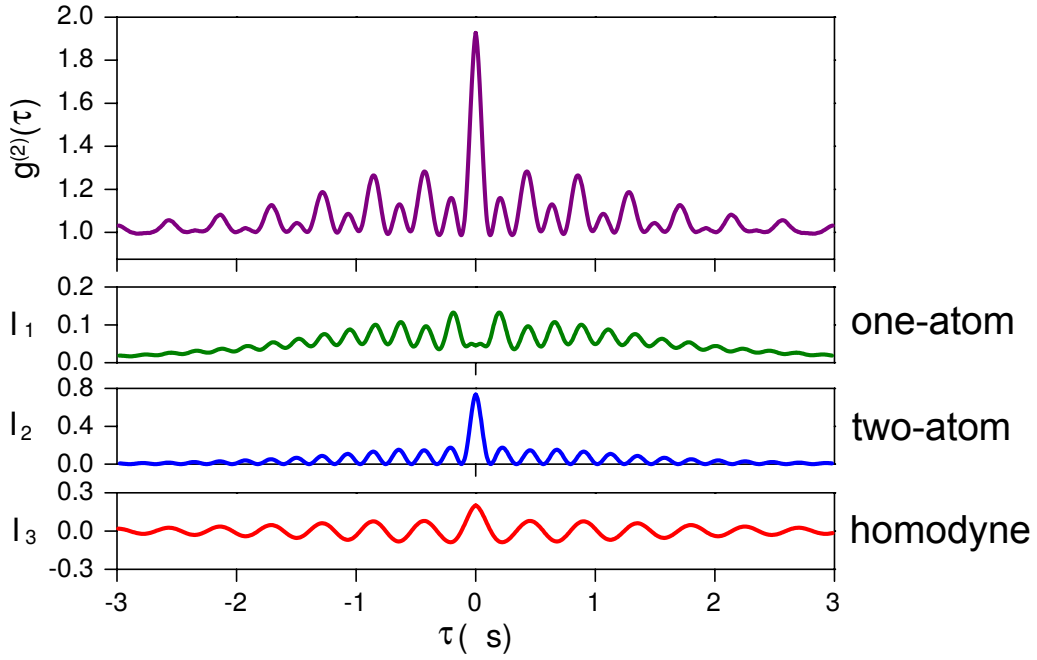

Figure 1.5: Simulation of the leading quantum beat contributions to the $g^{(2)}(\tau)$

Chapter 2: Control of conditional quantum beats in cavity QED: Theory

Preservation of quantum coherence is of fundamental importance in many fields, from atomic clocks to quantum information science. The tension between interaction with an environment to extract information and dissipation is at the heart of quantum open systems [20,21]; attempts to isolate a system usually remove the possibility of measuring and controling its dynamics. Recent developments in quantum feedback [22–24] and its application in quantum optics, however, point to an era where the theoretical tools and experimental time scales needed for control are within reach.

In this chapter we show theoretically that it is possible to preserve the coherences, recovering both amplitude and phase, by following a protocol that starts with the detection of a photon, which then triggers a pulse to turn off the system drive. Chapter 3 describes our experimental implementations.

Decoherence of the ground-state superposition arises from several factors. The simplest to understand is the transit time of the atoms across the mode of the cavity. However, we have other mechanisms, and an important contribution comes from the dephasing process due to random Rayleigh scattering. In this section, we present

–based on the phase shifts from quantum jumps– a simplified model of the rate of decoherence due to this process and the associated shift in the Larmor precession frequency [19].

A π polarized coherent field with amplitude α, resonant with the transition $|g_0\rangle \rightarrow |e_0\rangle$, drives π transitions on the vertical mode of a cavity QED system in the presence of a magnetic field (see Fig. 1.4). The cavity provides two orthogonal modes for drive and detection of the system. Some of the spontaneous emission enters the orthogonal polarization mode H. The input to the correlator consists of the H spontaneous emission mixed with a local oscillator of strength ϵ. The detection of a first H photon prepares a ground-state superposition [6] that evolves in time as

$$|\psi_g(t)\rangle = C_0 \frac{1}{\sqrt{2}}(e^{i(\Delta_g+\Delta_{\rm AC})t}|g_-\rangle + e^{-i(\Delta_g+\Delta_{\rm AC})t}|g_+\rangle) + C_1|g_0\rangle \tag{2.1}$$

where the amplitudes C_0 and C_1 depend on the strength and phase of the local oscillator. The term $|g_0\rangle$ appears because it is not possible to know the origin of the first detected photon in the presence of the local oscillator: it can come either from the local oscillator or from the atomic spontaneous emission. To lowest order in $g^2|\alpha|^2$ (drive intensity) the ground-state AC Stark shifts are

$$\Delta_{\rm AC} = -\frac{g^2|\alpha|^2\Delta}{(\gamma/2)^2 + \Delta^2} \tag{2.2}$$

for state $|g_+\rangle$ and $-\Delta_{\rm AC}$ for $|g_-\rangle$.

The amplitudes in Eq. (2.1) couple to the corresponding excited-state ampli-

tudes, driving a steady-state superposition:

$$|\psi_e(t)\rangle = C_0 \frac{g\alpha}{\sqrt{2}} \left(\frac{e^{i(\Delta_g+\Delta_{\rm AC})t}}{\gamma/2 - i\Delta} |e_-\rangle + \frac{e^{-i(\Delta_g+\Delta_{\rm AC})t}}{\gamma/2 + i\Delta} |e_+\rangle \right) + C_1 \frac{g\alpha}{\gamma/2} |e_0\rangle. \tag{2.3}$$

The excited-state amplitudes follow the ground-state oscillation; the excited-state splitting enters through the factors $\gamma/2 \pm i\Delta$ only, which carry a phase shift. Consider now the effect of quantum jumps from spontaneous emission occurring during the interval in between the detection of a pair of H polarized photons from the cavity, i.e., the π jumps which constitute Rayleigh scattering in Fig. 1.4. With jump rate $\Gamma = 2g^2|\alpha|^2/(\gamma/2)$, the driven dipole between ground and excited states turns off and the amplitudes of Eq. (2.3) are transferred to the ground state. It follows that each time a quantum jump occurs there is a phase advance; if n quantum jumps occur, Eq. (2.1) is replaced by:

$$\begin{aligned} \mathcal{N}_n |\psi_g(t)\rangle \;=\; & \frac{C_0(\gamma/2)^n}{\sqrt{2}} \left\{ \frac{(\gamma/2 + i\Delta)^n}{[(\gamma/2)^2 + \Delta^2]^{n/2}} e^{i(\Delta_g+\Delta_{\rm AC})t} |g_-\rangle \right. \\ & \left. + \frac{(\gamma/2 - i\Delta)^n}{[(\gamma/2)^2 + \Delta^2]^{n/2}} e^{-i(\Delta_g+\Delta_{\rm AC})t} |g_+\rangle \right\} + C_1 [(\gamma/2)^2 + \Delta^2]^{n/2} |g_0\rangle \,, \end{aligned} \tag{2.4}$$

with normalization factor:

$$\mathcal{N}_n = \sqrt{|C_0|^2 (\gamma/2)^{2n} + |C_1|^2 [(\gamma/2)^2 + \Delta^2]^n}. \tag{2.5}$$

The ground-state superposition has acquired a phase advance. The number of quantum jumps increases with time, so the phase advance accumulates over time.

We average against a Poisson distribution with mean Γt to obtain the expec-

tation value of the ground-state coherences for jump rate Γ:

$$\begin{aligned}\rho_{g_+,g_-} &= e^{-2i(\Delta_g+\Delta_{\rm AC})t}\frac{|C_0|^2}{2}\sum_{n=0}^{\infty}\frac{(\gamma/2)^{2n}}{\mathcal{N}_n^2}\frac{(\gamma/2-i\Delta)^{2n}}{[(\gamma/2)^2+\Delta^2]^n}\frac{(\Gamma t)^n}{n!}e^{-\Gamma t} \\ &\approx e^{-2i(\Delta_g+\Delta_{\rm AC})t}\frac{|C_0|^2}{2}e^{-(2\Gamma_{\rm decoh}+i2\Delta_{\rm jump})t} \qquad (2.6)\end{aligned}$$

and

$$\rho_{g_\pm,g_0} \approx e^{\mp i(\Delta_g+\Delta_{\rm AC})t}C_0^*C_1e^{-(\Gamma_{\rm decoh}\pm i\Delta_{\rm jump})t}, \qquad (2.7)$$

where we assume $2\Delta/\gamma \ll 1$ and take $(\gamma/2)^{2n}/\mathcal{N}_n^2 \approx 1$.

The imaginary part of the exponents in Eqs. (2.6) and (2.7) contains terms $-2\Delta_{\rm jump}t$ and $\mp\Delta_{\rm jump}t$, where to first order in $2\Delta/\gamma$:

$$\Delta_{\rm jump} = \Gamma\frac{2\Delta}{\gamma} = \frac{8g^2|\alpha|^2\Delta}{\gamma^2} = -2\Delta_{\rm AC}. \qquad (2.8)$$

These terms represent an additional frequency shift arising from the mean rate of phase accumulation from quantum jumps due to Rayleigh scattering. For the $(g_\pm, g_0)$-coherence, the net differential ground-state light shift, in the low drive limit, becomes:

$$\Delta_{\rm light} = (\Delta_{\rm AC}+\Delta_{\rm jump}) \approx -\Delta_{\rm AC}, \qquad (2.9)$$

and $2\Delta_{\rm light} = -2\Delta_{\rm AC}$ for the (g_+, g_-)-coherence.

The exponent in Eqs. (2.6) and (2.7) also contains a damping term, which decoheres the quantum beats at a rate (to lowest order in $2\Delta/\gamma$)

$$\Gamma_{\rm decoh} = \Gamma\frac{\Delta^2}{(\gamma/2)^2} = 2g^2|\alpha|^2\frac{\Delta^2}{(\gamma/2)^3}. \qquad (2.10)$$

The decoherence arises from the phase diffusion which accompanies the average phase drift responsible for the frequency shift. The two aspects, drift and diffusion,

come together as a package from the stochastic nature of the jump process as we can see in Fig. 2.1.

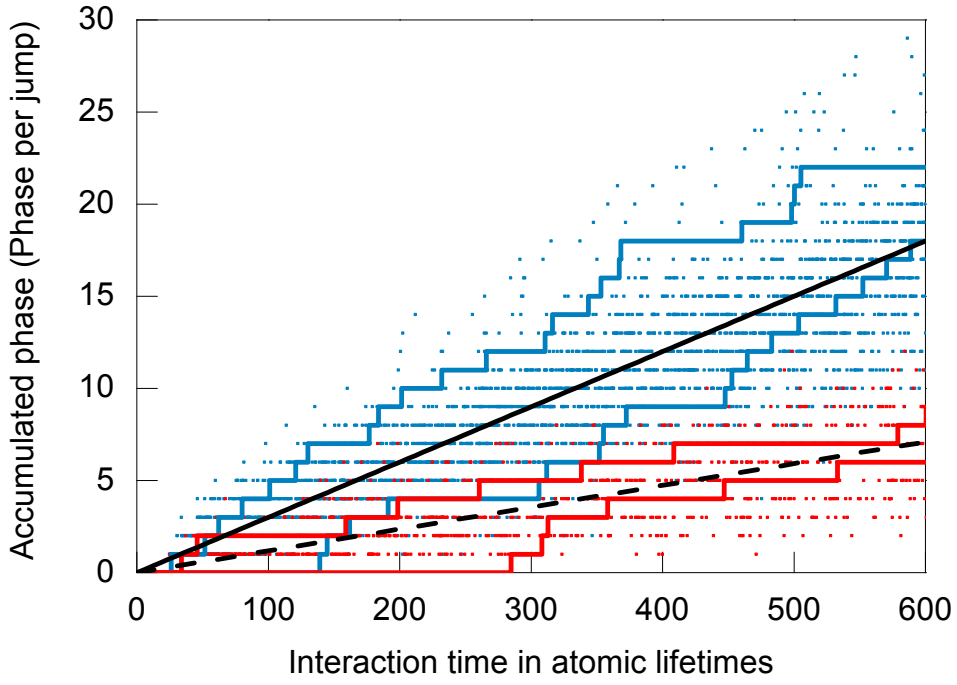

Figure 2.1: Sample quantum trajectories showing the phase accumulated in the ground state through Rayleigh scattering. The points show 200 realizations of an atom (Blue $n = 2.9$ and red $n = 0.7$) while the straight lines show the mean phase accumulation. The continuous red and blue lines represent typical trajectories.

The probability of detecting a second photon with H polarization following a trigger detection is proportional to

$$\langle\psi(\tau)|(\epsilon^* + \sigma_{\mathrm{H}}^\dagger)(\epsilon + \sigma_{\mathrm{H}})|\psi(\tau)\rangle, \tag{2.11}$$

with $\sigma_{\mathrm{H}} = |g_0\rangle\langle e_+| + |g_0\rangle\langle e_-|$, and $|\psi(\tau)\rangle$ the state of the system at time τ after initiation by the trigger jump. The terms $\langle\psi(\tau)|\epsilon^*\sigma_{\mathrm{H}}|\psi(\tau)\rangle$ and $\langle\psi(\tau)|\sigma_{\mathrm{H}}^\dagger\epsilon|\psi(\tau)\rangle$ couple states $|e_\pm\rangle$ with $|g_0\rangle$, and due to the mapping of the ground-state coherence to the

excited state, they oscillate as $\rho_{g_\pm,g_0}$. For ϵ sufficiently large these homodyne terms dominate. We then measure a second-order correlation function whose quantum beats oscillate at the Larmor frequency plus Δ_{light}.

The driving field can control the frequency shift and decoherence induced by Rayleigh scattering. Figure 2.2 shows an example of the proposed protocol, calculated on the basis of the simple model of a fixed atom and two cavity modes. Fig. 2.2(a) displays the time evolution of the intensity correlation function of the undriven mode with no intervention (blue line) and with the drive laser (π polarization) turned off 20 atomic lifetimes after the detection of the first photon (red line); the system then evolves freely until the drive is returned to its previous value after a further 80 lifetimes (blue trace). Note that the amplitude of the red trace returns to the same value as before the turn off, while the phase accumulated is different in the presence of the drive and in the dark. We create and capture the coherence, preserving it in the dark, where it evolves without interrogation, and then we recover it. The phase difference visible after the oscillations return is a measure of the average number of intervening quantum jumps. Figure 2.2(b) shows how the ground-state coherence evolves in the dark for eighty atomic lifetimes, without any change in frequency or loss of amplitude due to Rayleigh scattering.

The model analyzed in this section is idealized as the considered transition has many more levels, and σ and well as π transitions occur. It is nevertheless a good one to gain qualitative understanding of the phenomena. We have also developed a full quantum simulation of the problem including all relevant experimental realities. The details of that model and relevant calculations can be found in Ref. [13].

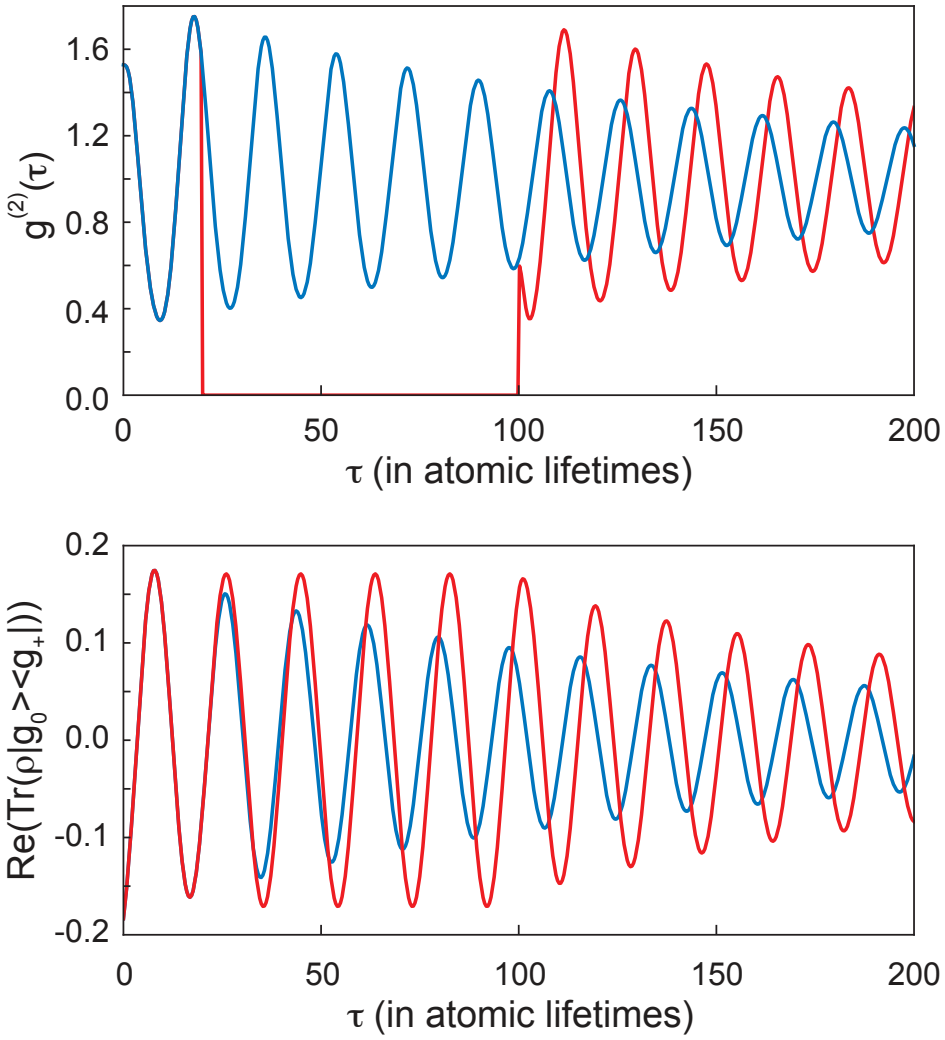

Figure 2.2: Time response of the system when pulsing the drive (red) and with a continuous drive (blue). (a) Conditional intensity $g^{(2)}(\tau)$ (the traces initially overlap). (b) Atomic coherence between $|g_0\rangle$ and $|g_+\rangle$. For a drive strength corresponding to one photon in the driven mode, one fixed maximally coupled atom, and $\epsilon = 0.1$.

Chapter 3: Control of conditional quantum beats in cavity QED: experiments

This chapter contains a series of experiments aimed at controlling the quantum beats and their decoherence. They all respond to a similar kind of experiment where we perform strong feedback. Figure 3.1 shows a simple diagram illustrating the necessary components of strong quantum feedback. A measurement carried out on a quantum system has an associated back-action effect. The feedback is proportional to the measurement.

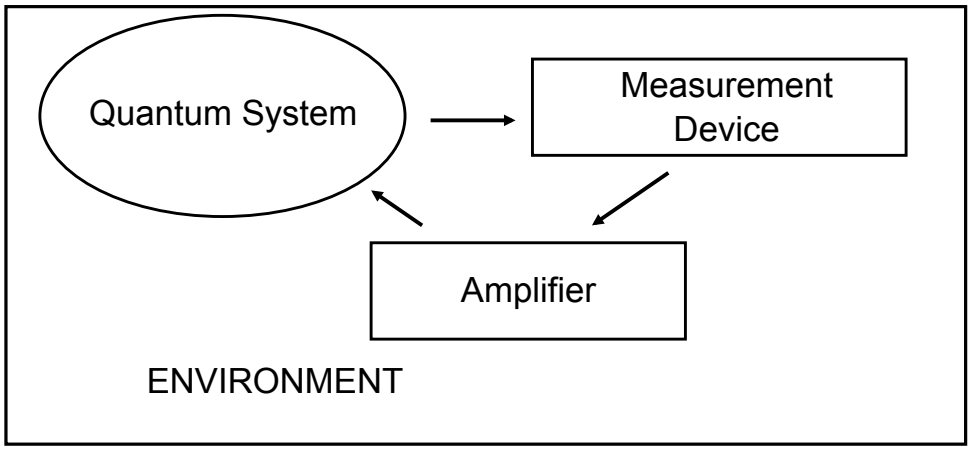

Figure 3.1: Strong quantum feedback diagram. The feedback signal is proportional to the measurement performed on the system, which has a back-action effect

3.1 Preliminary experiment

3.1.1 Introduction

The detection of a photon escaping a quantum system at a random time heralds the preparation of a conditional quantum state. Manipulation of these states is essential in the field of quantum feedback. The preferential probe of this conditional measurement in quantum optics is the intensity correlation function which has been used since the pioneer work of Kimble *et al.* on resonance fluorescence [25].

This section presents the preliminary implementation of quantum feedback in our cavity quantum electrodynamical (QED) system. It acts on the ground state coherences we observed [6]. However, it builds up on extensive literature that has looked into the evolution and control of quantum states such as Refs. [26, 27]. This work closely follows our previous studies [28–30], except our conditional state manipulation is long-lived (~ 5 μs) and it consists of a ground state superposition detected through a homodyne measurement done in photon counting.

Wiseman [31] established the connection between homodyne measurements and weak measurements in cavity QED. Weak measurements reduce the problems of back action in quantum feedback [32, 33]. Our previous work with conditional homodyne detection [34–36] used a strong local oscillator. Recent measurements perform homodyne detection of resonance fluorescence with a weak local oscillator [37]. Our work is moving on that direction and we expect to improve our ability to control the quantum states with new forms of feedback

3.1.2 Experimental setup

Figure 3.2 shows the main features of the experiment. Figure 3.6 presents a schematic of the apparatus. Our optical cavity QED system is in the regime of intermediate coupling, where the dipole coupling constant ($g/2\pi = 1.2$ MHz) is comparable to the cavity and spontaneous emission decay rates ($\kappa/2\pi = 3$ MHz and $\gamma/2\pi = 6$ MHz). Our experiment consists of a 2 mm Fabry-Perot cavity and a source of cold ^{85}Rb atoms [13]. The source delivers, on average, a few maximally coupled atoms within the mode volume of the cavity at all times. This continuous cold atomic beam comes from an unbalanced Magneto-Optical Trap, a technique known as LVIS (Low Velocity Intense Source) [38]. The cavity supports two degenerate modes of orthogonal linear polarization (H and V). During their 5 μs transit, the atoms interact with the orthogonally polarized modes and can spontaneously emit into the cavity. We drive the D_2 line of ^{85}Rb between the ground level $F = 3$ and the excited level $F = 4$ in the presence of a magnetic field of about 2 Gauss. For a more detailed description of the apparatus, see Ref. [7].

Atoms enter the cavity optically pumped to $5S_{1/2}$ $F = 3, m = 0$ which corresponds to our $|g_0\rangle$. A Glan-Thompson polarizer and zero-order half-wave plate (HWP) placed before the cavity linearly polarize the drive with a very good extinction ratio that can reach better than 5×10^{-5}. After the cavity another HWP aligns the output polarization to a Wollaston polarizing beam splitter (PBS) to separate the H and V modes. The H light passes through a regular beam splitter (BS) which divides the light between two avalanche photodiodes (APD). Both detector

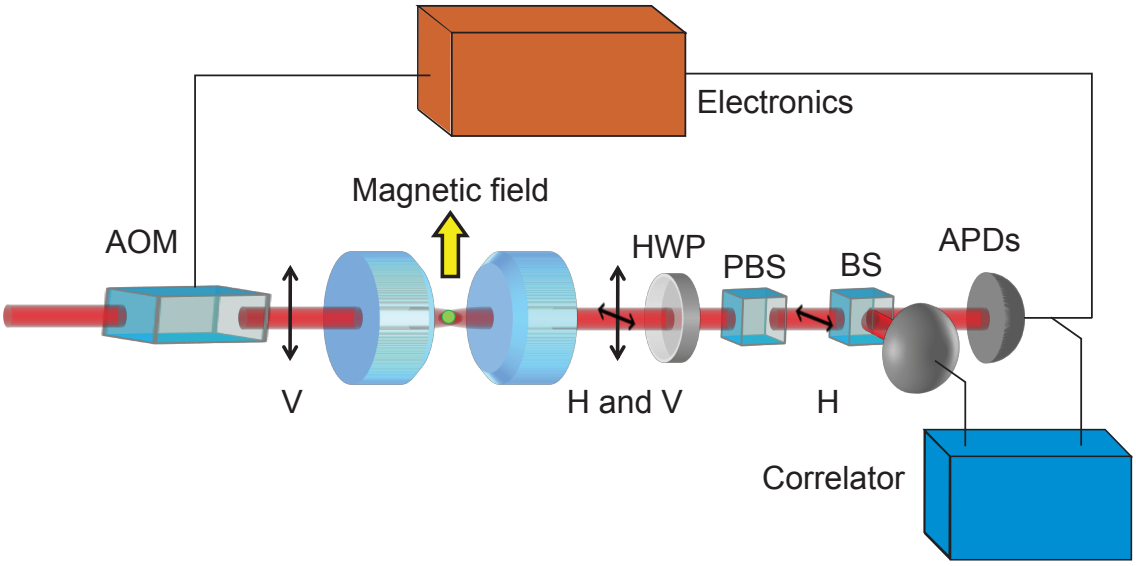

Figure 3.2: Schematic of the apparatus. HWP: Half-Wave Plate, APD: Avalanche Photo-Diode, PBS: Polarizing Beam Splitter, BS: Beam Splitter, AOM: Acousto-Optic Modulator

outputs then go to a correlator card (Becker and Hickl DPC-230) which records a continuous stream of detection times with a resolution of 164 ps.

The pulse from the 'start' APD (designated arbitrarily) is split into two and passed through a Lecroy 688AL level adaptor to produce a clean TTL pulse. This triggers an HP 33120 signal generator whose output controls the amplitude modulation port of an Isomet D323B radio frequency driver box. The driver connects to an 80 MHz Crystal Technology 3080-122 acousto-optical modulator (AOM), whose first-order diffracted beam drives the cavity. In this way, the intensity of the drive can be modulated conditionally, based on the trigger from the 'start' APD.

3.1.3 Results

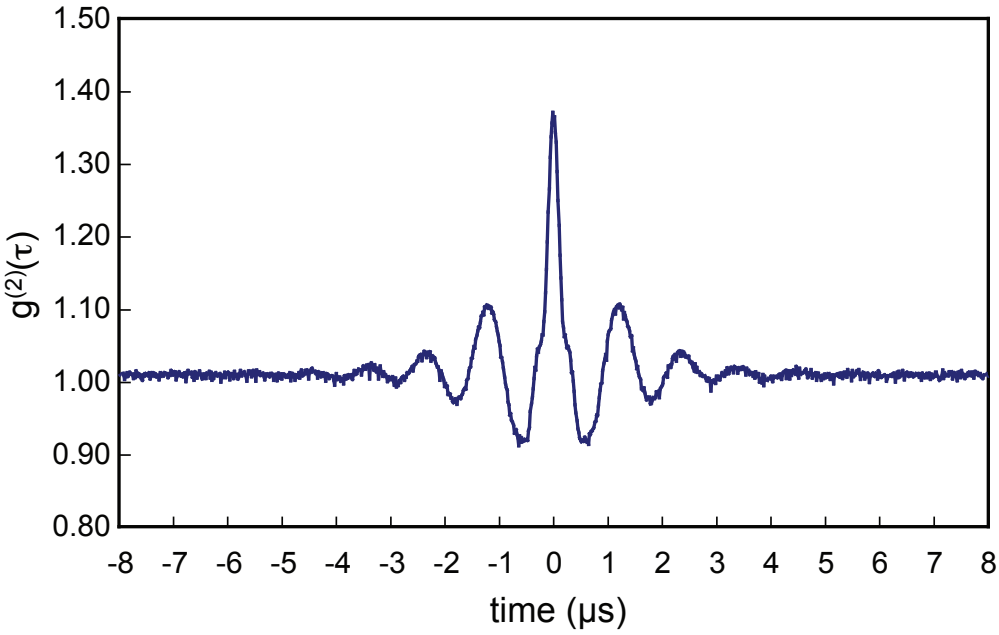

Figure 3.3: $g^{(2)}(\tau)$ exhibiting a homodyne quantum beat oscillation with $f = 860$ KHz, corresponding to a magnetic field strength of 1.8 G

We measure the intensity correlation function $g^{(2)}(\tau)$ from our cavity in a regime where the homodyne quantum beat term dominates, which we achieve by changing the angle on the HWP after the cavity by approximately 2 degrees away from maximum drive extinction. The effective number of maximally coupled atoms in the mode is approximately 2. Fig. 3.3 shows our normalized second-order correlation function due primarily to the beating against the drive; this is apparent because it dips below one.

The basic idea for control is simple. We rely on conditional measurements to set the initial phase of the quantum beat. Since the intensity of the detected light

is proportional to the drive intensity (from both the atomic spontaneous emission and the driven mode response), we can modulate the drive at the same frequency as the conditional output signal but with opposite phase. This way the beat will cancel as long as the modulation amplitude is chosen correctly.

We are able to model the signal (after 0.5 μs) with a simple function that contains an oscillation ($\cos \Omega t$) at frequency $\Omega/2\pi$=860 kHz, Gaussian damping ($\exp -(t^2/\sigma^2)$) with $\sigma = 1.8$ μs, and amplitude and time offsets; the intent is to capture the basic physics, not to fit the exact form. The oscillation corresponds to the Larmor frequency and the characteristic time of the Gaussian reflects the transit time of the atoms through the Gaussian transverse profile of the mode. The sharp peak at the origin is a multiatom contribution (see Fig. 4d in Ref. [6]) that we are not taking into account. We obtain the numbers for the model by looking at the fast Fourier transform (FFT) of the data in Fig. 3.3 as well as at the long term ($\approx$ 8 μs) value of the background. The width of the resonance in the FFT fits well to a Gaussian, but there is an asymmetry on the characteristic width; we average the two numbers and use that for the model. There are other frequencies visible on the FFT, coming from the standing wave modulation of the dipole coupling constant and from the harmonics of the Larmor frequency; we ignore these in the model.

Figure 3.4a illustrates the usual undisturbed signal (red squares) and the signal with the feedback protocol (continuous blue line) based in the model of the signal that we just presented. It is clear that there is a modification of the response during the time that the pulse is applied, but the cancellation is not perfect. The difference Fig. 3.4b between the trace with feedback and that without recovers the applied

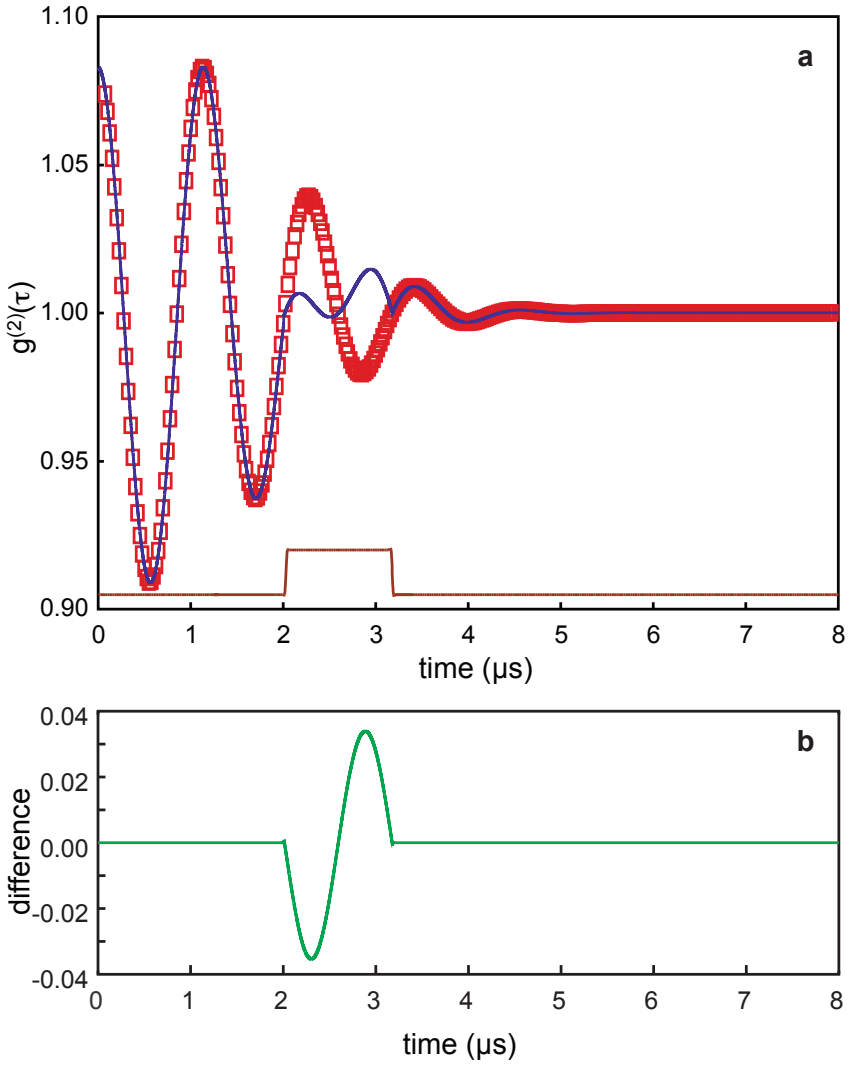

Figure 3.4: Calculated $g^{(2)}(\tau)$ signal from the feedback model with parameters extracted from the experiment. **(a)** The red squares are model without feedback. The blue trace is model calculation exhibiting the effects of our feedback. The brown trace at the bottom identifies the time window where we apply the feedback. **(b)** Shows in green the difference between the red squares (no feedback) and the blue line (with feedback).

modulation to the input drive.

A photon "click" in the 'start' detector triggers the signal generator, which outputs a sinusoidal voltage pulse whose amplitude-to-offset ratio is 8.5%, in a voltage region where the AOM and driver amplitude response is linear. The delay in the application of the modulation to the drive has an intrinsic ($\sim 1.5\ \mu$s) contribution from the signal generator, and a variable part which we use to adjust the phase to match that of the quantum beats.

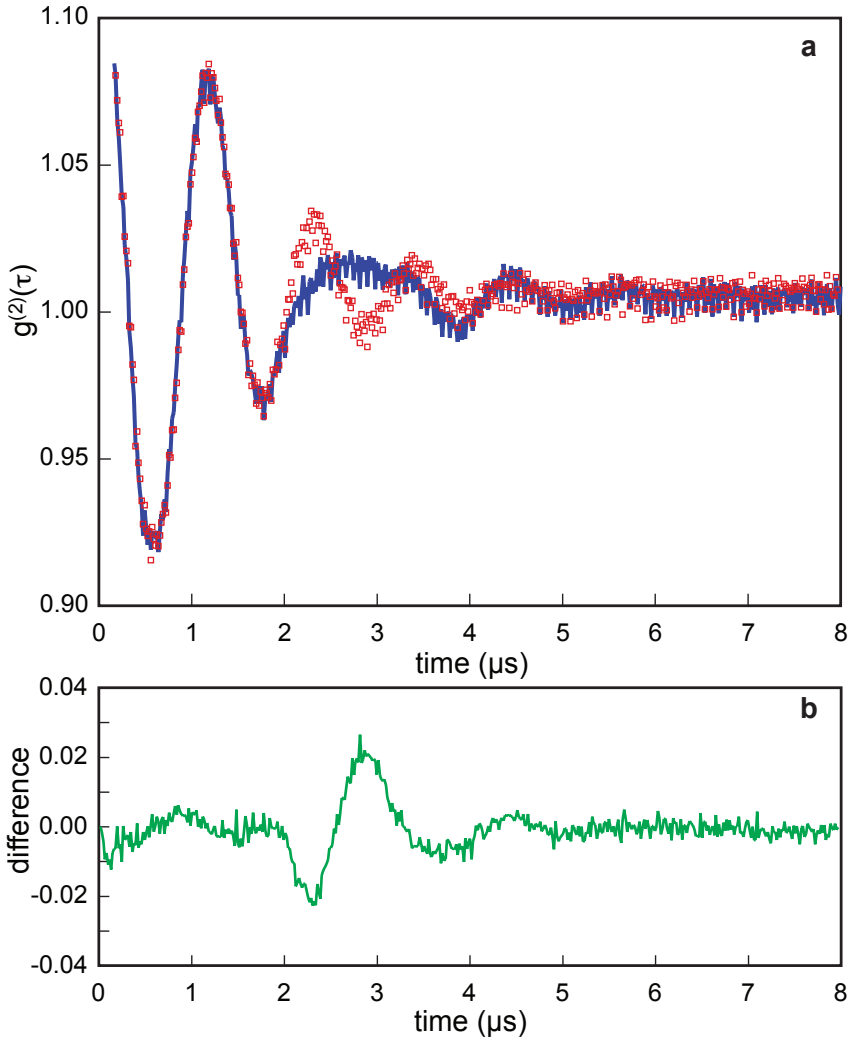

Figure 3.5: Experimental measurements of **(a)** $g^{(2)}(\tau)$. The red squares is the negative-τ portion reflected back across the vertical axis of the data. The blue trace is the positive-τ portion, exhibiting the effects of our feedback. **(b)** shows in green the difference between the red squares (no feedback) and blue traces (with feedback).

The feedback pulse lasts for one period of the quantum beat oscillation (~ 1.2 μs), after which the beat returns with the same phase as before. We obtain a

partial attenuation of the oscillations (See blue line in Fig. 3.5a), owing primarily to the mismatch between the shape of the applied pulse and the measured $g^{(2)}(\tau)$. Performance can be improved with use of a programmable pulse generator that matches more carefully the shape of the decaying exponential. In addition, trigger events missed due to signal generator dead time decrease the effects of the feedback.

3.2 Experiment controlling amplitude decoherence and phase shifts

3.2.1 Introduction

This work goes beyond our previous experiments on quantum feedback in optical cavity QED [28,30] where only the amplitude was recovered, without control over the phase. Moreover, that protocol depended critically on the specific time of feedback application after a photon detection. Our current work shares with it a reliance on strong quantum feedback, where we draw on our knowledge of the conditional dynamics of the system to capture (store) and at a later time release a quantum state.

More recent experiments aim at deterministic quantum control [39, 40]. In contrast, we use spontaneous emission to prepare and detect the ground-state coherence. This renders our control protocol non-deterministic. The implementation of our fast feedback helps us go further in the context of studying the effects of drive duration and strength on the coherence and accumulated phase of our superposition.

The protocol is rather simple. It requires no processing but simply follows from the setting of a quantum beat phase by the detection of a single photon. This is in

contrast with two recent quantum control studies. The first, recent experiments with Rydberg atoms in superconducting cavities [41, 42], performs extensive calculations based on measurement outcomes to create and maintain a Fock state in a microwave cavity. The second reports experiments and theory aiming for quantum control of the full ground state manifold of Cs [26, 43, 44].

3.2.2 Apparatus

This section explains our apparatus, data taking, data processing, and the experimental realization of the feedback mechanism to protect the coherence of the ground-state superposition. The cavity parameters as well as a short description of the atomic beam are in Sec. 3.1.2. For this work, we use a magnetic field strength of 5 G.

Birefringence from the cavity mirrors, vacuum chamber windows and lenses has a small effect on the frequency separation of the H and V modes. At the working intensities of the experiment the two modes are degenerate to better than 0.1κ and the extinction ratio at the output is better than 5×10^{-4}, a negligible contribution.

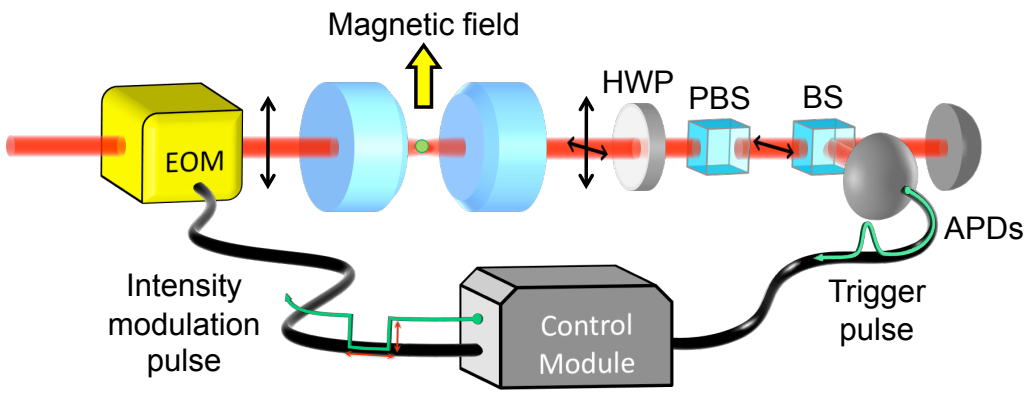

Figure 3.6: Schematic of the experimental apparatus. The detection of a photon generates an electronic pulse that changes the amplitude of the laser drive for a pre-set amount of time. An electro optical modulator (EOM) sets the drive intensity. The light exits the cavity and passes through a half wave plate (HWP), a polarizing beam splitter (PBS), and a beam splitter (BS), which direct photons onto a pair of avalanche photodiodes (APDs). The photo-pulses from the APDs are correlated aginst the initial photon detection to obtain $g^{(2)}(\tau)$ (corrrelator not shown).

The light at 780 nm passes through an EOSpace fiber electro-optic modulator before reaching the cavity. This device generates amplitude modulation sidebands at 227 MHz on the light. The upper sideband acts as the drive of the system and the carrier and the lower sideband reflect back from the cavity. The setup allows us to rapidly manipulate the amplitude of the drive. We use an SRS digital delay generator DG645 to generate an electronic pulse (risetime less than 10 ns) that opens a minicircuits ZAD-1-1 double balanced mixer, operating as an RF attenuator, to generate the 227 MHz RF frequency that feeds the EOM. The output of the APDs

(SPCM-AQR Perkin Elmer), in the form of TTL pulses, travels to a correlator card (Becker & Hickl DPC-230), where each pulse arrival is time stamped and stored. We split one of the APD TTL pulses before reaching the correlator card and use it to trigger the DG645, which then drives the mixer. We set the length of the pulse and its amplitude with the DG645. The intrinsic electronic delay of the system is 325 ns, limited by the internal delay of the DG645 between external trigger and gate output.

The process of random photon emission via spontaneous decay translates into a stream of TTL pulses, which causes the DG645 to miss some triggers. The device can handle trigger rates up to 10 MHz, but from a synchronous source. Our photon detection rate of $\sim$ 20 kHz (start APD) causes about 2% of missing triggers. We only keep the photon arrivals that successfully trigger the DG645 by implementing a software filter when processing the data. The DG645 produces a copy that we also send to the correlator card and use for the software filter [1].

We detect the atomic coherence by directly looking at the light in the undriven mode of the cavity or using a homodyne process where a small part of the light exiting the drive mode is mixed with the signal using a half wave plate (HWP in Fig. 3.6). The latter case allows us to look directly at the Larmor frequency in the Zeeman ground state superposition, and the oscillations show the interference of two fields, one that has the oscillation and one that does not, while in the former case the interference takes place between fields coming from the same source.

[1] auto-correlation and filtering computer code available at: `http://hdl.handle.net/1903/13306`

The loss of coherence of the superposition is a degradation that is intimately related to the interrogation by the drive laser [19]. The protocol that we present in this section to eliminate it consists of reducing the amplitude of the π drive to the cavity after a pre-set time from the detection of the first photon, and then returning the amplitude to the previous level after a fixed time to look at the oscillations. Since the frequency of oscillation is, to first order, set by the Larmor precession frequency; the atoms preserve the phase without interrogation, continuing their oscillation in the ground state.

3.2.3 Results

We now present the results of the feedback protocol: an increase in coherence time of the ground-state superposition, *i.e.* an increase in beating amplitude, and the contrast in accumulated phase due to different precessing frequencies in the presence or absence of drive.

Figure 3.7 shows two experimental traces using the homodyne process. Each pair of traces represents an average over a little more than 20 million photon arrivals. The time that elapses for each dataset, at an average rate of 60,000 counts/second (count rate of detectors A and B), is about $\sim$6 minutes. Each bin of 16 ns can have between 3000 and 4000 counts. The blue trace corresponds to no feedback pulse, and the red to a pulse of 2.5 μs, which is equivalent to 96 atomic lifetimes. The amplitude of the red trace is clearly larger when it returns, and there is a phase shift. Our two qualitative predictions are represented in the data.

Looking only at the undriven mode yields Fig. 3.8. The smaller SNR requires more averaging, which comes to 40 million photon arrivals. A rate of detection of 60,000 counts/second translates into a data taking time of about ∼12 minutes and twice as many coincidence counts per bin as the homodyne data run. The red trace shows a pulse of 1.4 μs.

The quantitative behavior depends on the exact mixing of the driving field and scattered light in the homodyne detection ($1.2 \pm 0.2^\circ$ at HWP), the number of photons in the driven mode ($n = 1 \pm 0.3$), as well as details of the number ($N_{\text{eff}} = 0.4 \pm 0.2$), velocity ($10 \leq v_p \leq 15\,\text{ms}^{-1}$), and angular distribution ($\theta \leq 20$ mrad) of the atoms. At any given time many atoms are present in the cavity mode. This gives rise to a peak (bunching) in $g^{(2)}(0)$. The data shows a count rate with the "off" position greater than zero due to a background unrelated to light scattered from the cavity V mode. The source of the background is scattering off the cavity mirrors of photons from the Magneto-Optical Trap laser beams and APD dark counts. These photons are uncorrelated and we set this level as the zero in the displayed experimental $g^{(2)}(\tau)$. The amount of background suppressed is the distance between the mark where $g^{(2)}(\tau) = 0$ and the bottom line of the frame in the figure (about 0.05 in this figure).

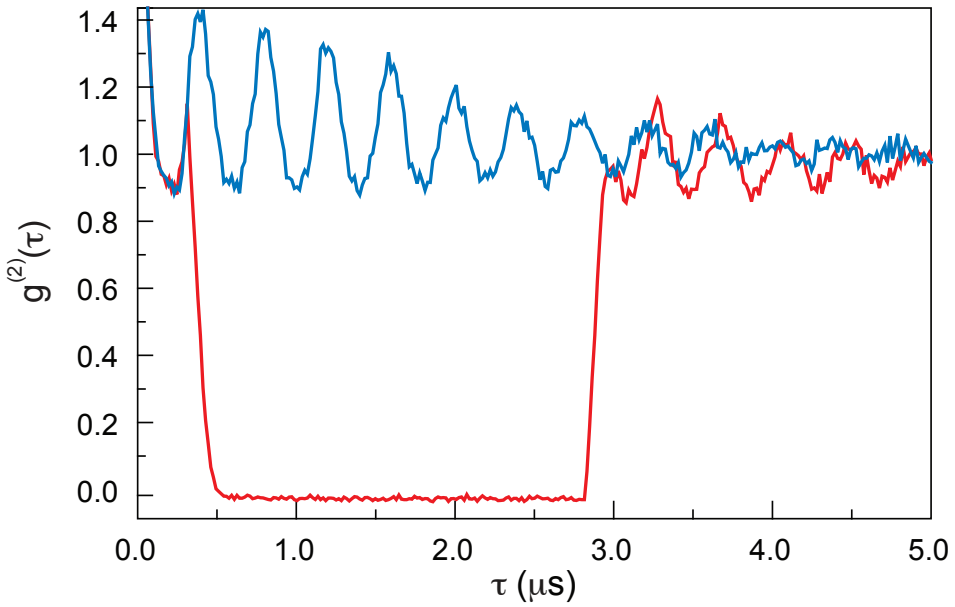

Figure 3.7: Measured conditional intensity evolution, $g^{(2)}(\tau)$ at Δ_g, of the undriven cavity mode in the presence of feedback (red) and with no feedback (blue). See text for a discussion of background suppression. For an effective atom number $N_{\text{eff}} = 0.4$, rotation of 1.2° at HWP, and mean number of photons in the driven cavity mode of $n = 1$.

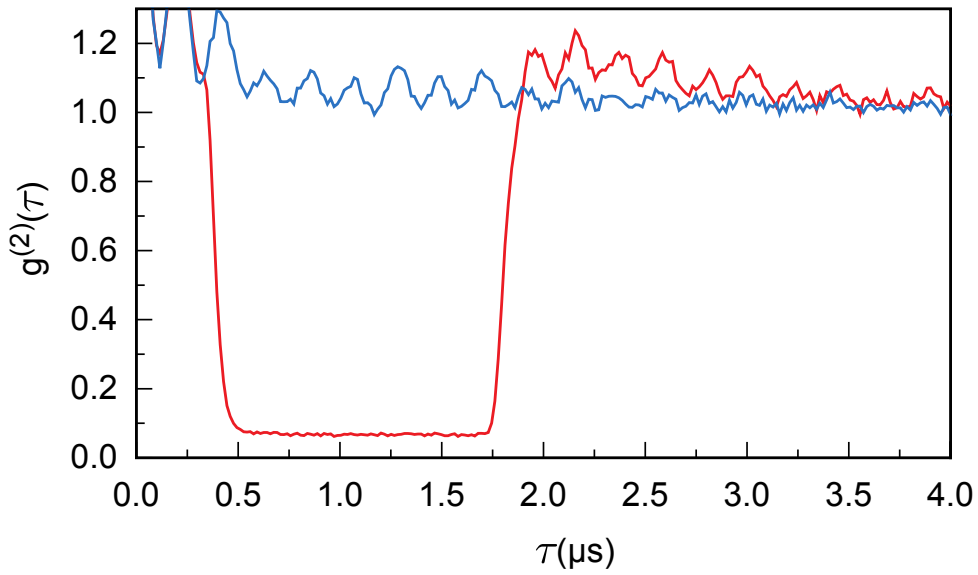

Figure 3.8: Measured conditional intensity evolution, $g^{(2)}(\tau)$ at $2\Delta_g$, of the undriven cavity mode in the presence of feedback (red) and with no feedback (blue). For an effective atom number $N_{\text{eff}} = 2.3$ and mean number of photons in the driven cavity mode of $n = 0.5$.

We estimate the intra-cavity driven mode photon number using an independent calibration of the efficiency and the size of the signal when we mix the polarizations in the undriven mode. The result is a photon number of $n = 1$ with an uncertainty of 30% based on traces similar to that of Fig. 3.7.

We derive a similar estimate for the other type of beat [45]. A value of $n = 0.5$ is obtained for traces similar to that of Fig. 3.8. The uncertainty is of the same order as our other calculation.

We repeat the measurements for different delay times as Fig. 3.9 shows. We extract the amplitude of the oscillation as a function of pulse width. Each trace taken has one side with no feedback and one with feedback. We perform a least

squares fit between the no feedback case and the feedback case making adjustments to match the amplitude and phase of the oscillation after the drive returns to its steady state. This is done with an algorithm and allows us to determine an error for the amplitude scaling and the phase shift.

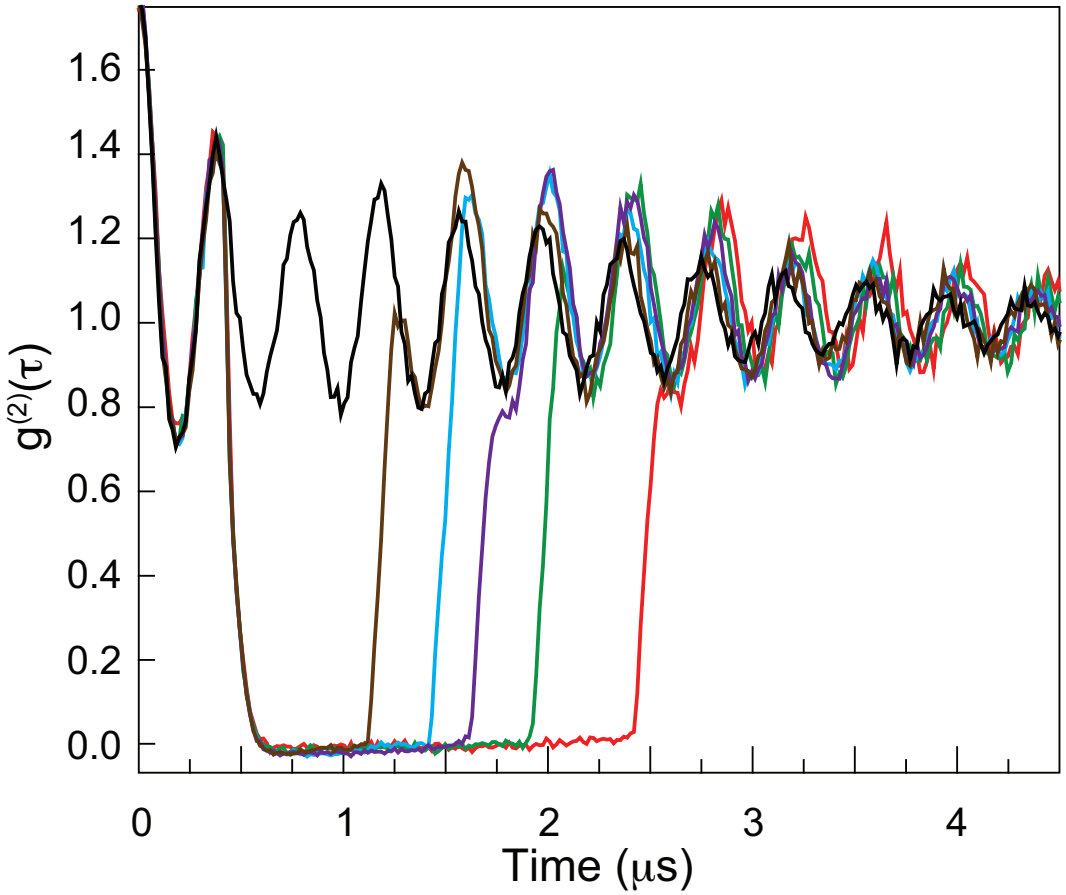

Figure 3.9: Measured conditional intensity, $g^{(2)}(\tau)$ at Δ_g , with various feedback pulse lengths for the homodyne beat

Figure 3.10 explains the fitting process. First, we restrict the fitting to a limited range of the data [Fig. 3.10(a) and (b)]; for all data sets we use the time of the drive turn-on as the starting point and a fixed ending point at $4.7\,\mu$s. We then fit a second-order polynomial to the maxima and minima of the oscillations.

We take an average of these curves and subtract them from the data [Fig. 3.10(c)]. This effectively removes differing backgrounds between the sides of the data. In the final step we perform the least-squares fit between the two batches, using two parameters: a time shift [Fig. 3.10(d)] and a scaling [Fig. 3.10(e)]; the residuals are shown in Fig. 3.10(f). We bin the data in 1.64 ns (16.4 ns) to optimize the phase shift (amplitude) extraction. Figure 3.10(g) illustrates the results of the process [2].

[2] MATLAB script available at: `http://hdl.handle.net/1903/13307`

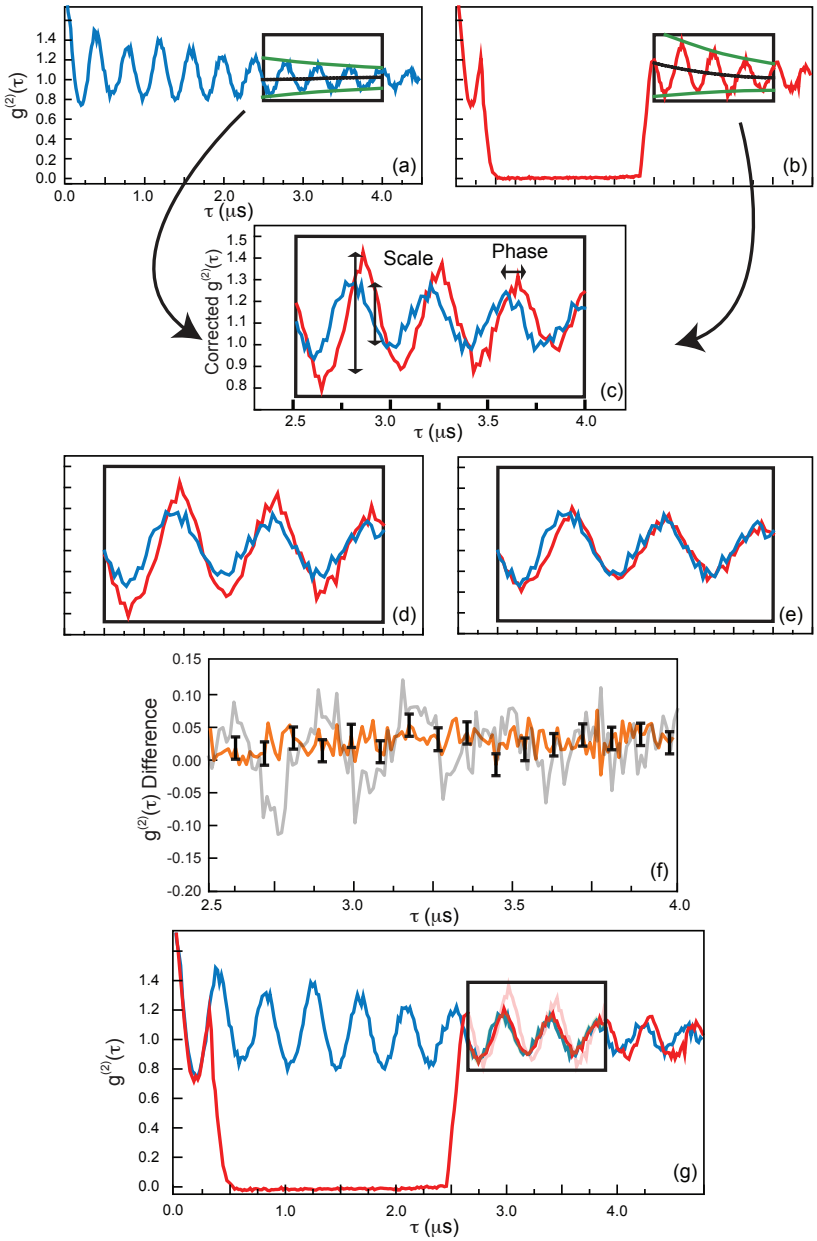

Figure 3.10: Least-squares fitting process. (a) $g^{(2)}(\tau)$ with no feedback and polynomial fits to maxima and minima in the restricted range. (b) $g^{(2)}(\tau)$ with feedback and similar polynomial fits. (c) Fitting region after removing backgrounds to show phase and amplitude difference. (d) After shifting. (e) After scaling. (f) Difference between the traces before (gray) and after (orange) the fitting. (g) End result with the original trace for comparison.

The fitting yields a phase shift and an amplitude change. First, we look at how the phase shift changes as the width of the feedback pulse is increased. The beat frequency is lowest (equal to the Larmor precession frequency) when the drive is off, and higher when it is on. The phase accumulated by the two $g^{(2)}(\tau)$ branches at a time τ after the feedback pulse is

$$\phi_- = \omega_{\rm on}\tau, \tag{3.1}$$

$$\phi_+ = \omega_{\rm on}\tau_0 + \omega_{\rm off}(\tau_{\rm f} - \tau_0) + \omega_{\rm on}(\tau - \tau_{\rm f}), \tag{3.2}$$

for the phase accumulated without (-) and with (+) feedback, where τ_0 is the time when the drive turns off and $\tau_{\rm f}$ is the time when the drive turns back on. We take the difference to obtain an expression for the phase shift:

$$\Delta\phi = \phi_- - \phi_+ = (\omega_{\rm on} - \omega_{\rm off})\,(\tau_{\rm f} - \tau_0) = \Delta_{\rm light}(\tau_{\rm f} - \tau_0). \tag{3.3}$$

The expression is linear in $\tau_{\rm f}$, and similar behavior is shown by the data in Fig. 3.11. A least-squares fit (continuous line) yields a slope of $\Delta_{\rm light}/2\pi = 0.073 \pm 0.004\,\mathrm{MHz}$, consistent with the prediction from the simple model, Eq. (2.8), of $\Delta_{\rm light}/2\pi = 0.075 \pm 0.025\,\mathrm{MHz}$ for $n = 1 \pm 0.3$.

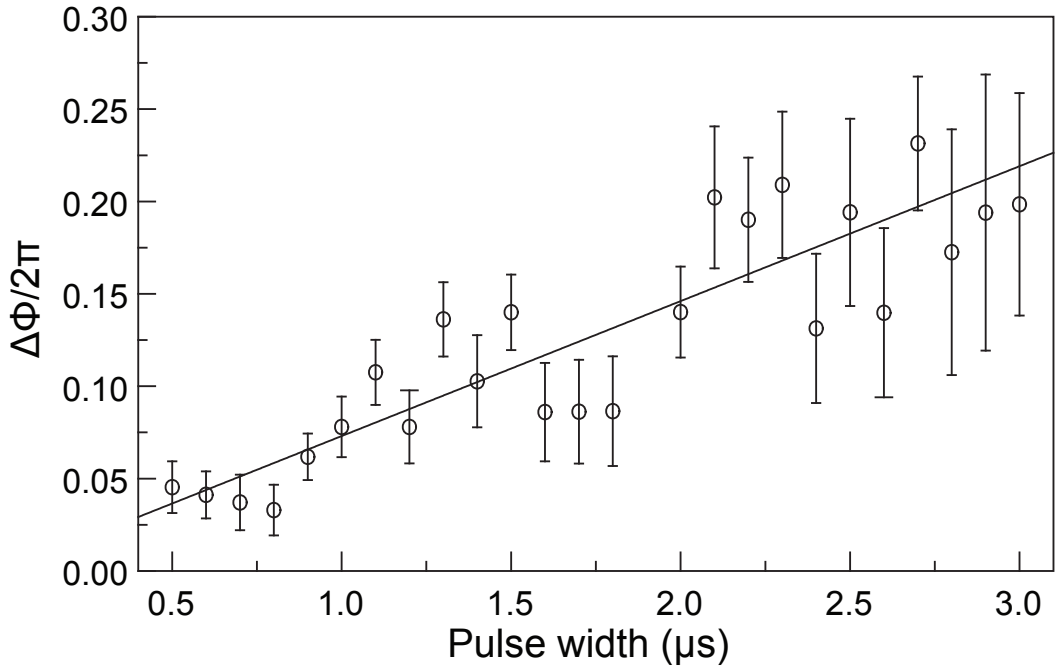

Figure 3.11: Accumulated phase shift as a function of feedback pulse width. The continuous line is the least-squares fit to the data (reduced $\chi^2 = 1.1$). Analysis done on the homodyne beat of frequency Δ_g

Equation 2.8 also applies to the purely atomic quantum beat. Figure 3.12 shows the evolution of the phase shift as a function of pulse duration. The linear fit gives us a value for the light shift of: $2\Delta_{\text{light}}/2\pi = 0.105 \pm 0.007\,\text{MHz}$ which is also consistent with our simple model: $2\Delta_{\text{light}}/2\pi = 0.103 \pm 0.009\,\text{MHz}$ for $n = 0.5 \pm 0.2$

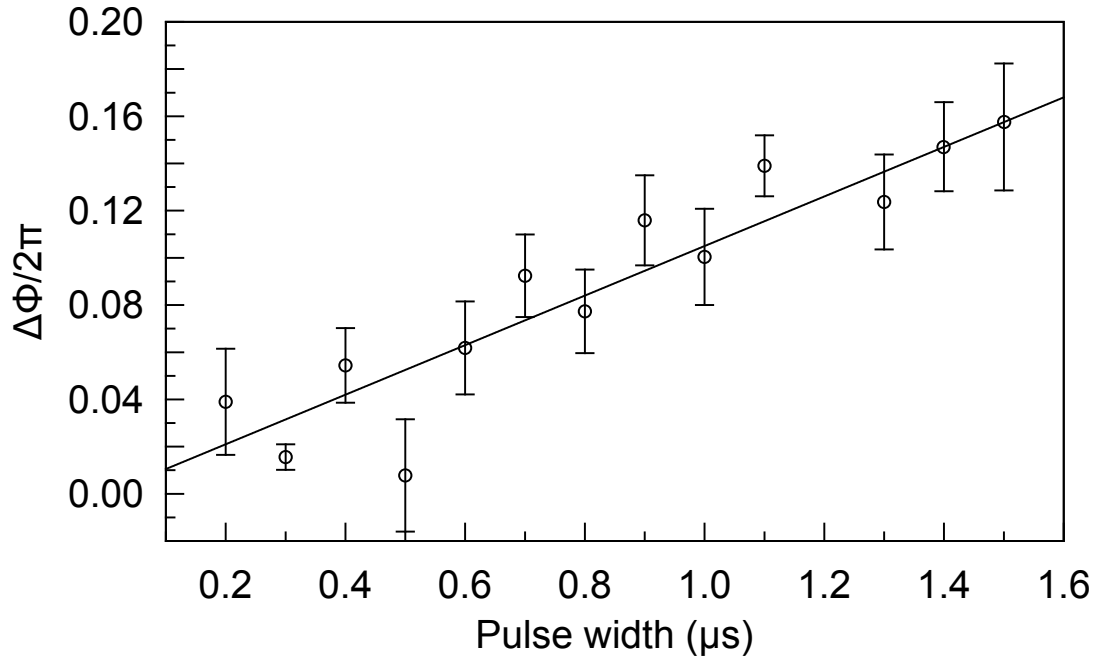

Figure 3.12: Accumulated phase shift as a function of feedback pulse width. The continuous line is the least-squares fit to the data (reduced $\chi^2 = 1.65$). Analysis done on the atomic beat of frequency $2\Delta_g$

Figure 3.13 presents results for the scaling of the oscillating in $g^{(2)}(\tau)$ as a function of feedback pulse width. This is a quantitative measure of the suppression of decoherence. If, for example, we let the system evolve in the dark for more than $2.5\,\mu$s, the amplitude of the oscillation is found to be a factor of two larger than without the feedback pulse; the protocol is clearly successful in suppressing decoherence. There other sources of decoherence, though, the dominant ones being the transit time of the atoms through the cavity mode and the angular distribution of their trajectories. We take the following simple additive model for decay of decoherence due to quantum jumps, rate $\Gamma_{\rm decoh}$, in the presence of other sources,

rate $\Gamma_{\rm other}$:

$$g^{(2)}(\tau) \propto 1 + e^{-\Gamma_{\rm other}\tau} e^{-\Gamma_{\rm decoh}\tau} \cos(\omega\tau). \tag{3.4}$$

It predicts the scaling $[g_+^{(2)}(\tau)-1]/[g_-^{(2)}(\tau)-1] = e^{\Gamma_{\rm decoh}(\tau_{\rm f}-\tau_0)}$, with $\tau_{\rm f}-\tau_0$ the feedback pulse width. The decoherence rate obtained from the data is $\Gamma_{\rm decoh}/2\pi = 0.037 \pm 0.001\,$MHz, compared with an expected value of $\Gamma_{\rm decoh}/2\pi = 0.032 \pm 0.010\,$MHz from Eq. (2.10), at $n = 1 \pm 0.3$.

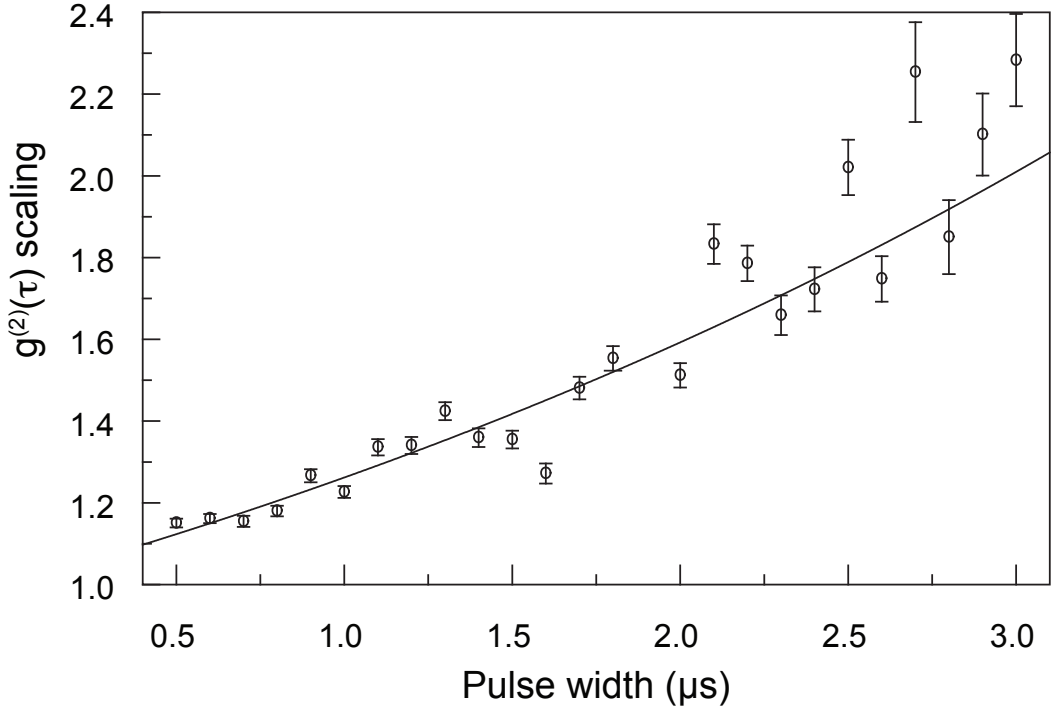

Figure 3.13: Measured scale factor for the amplitude of the oscillations in $g^{(2)}(\tau)$ as a function of feedback pulse width. The continuous line is the expected result from Eq. (3.4). This is a compilation of several data runs using homodyning

The striking result for the homodyne beat is even more appreciable when looking at the purely atomic quantum beat. Figure 3.14 shows that the scaling rises almost a factor of two more rapidly for this type of beat as a function of the pulse

duration. The exponential fit of Fig. 3.14 yields a value for the decoherence rate of $2\Gamma_{\rm decoh}/2\pi = 0.059 \pm 0.004\,{\rm MHz}$. The similarity between the theoretical prediction and experiment is clear: $2\Gamma_{\rm decoh}/2\pi = 0.064 \pm 0.005\,{\rm MHz}$, at $n = 0.5 \pm 0.2$.

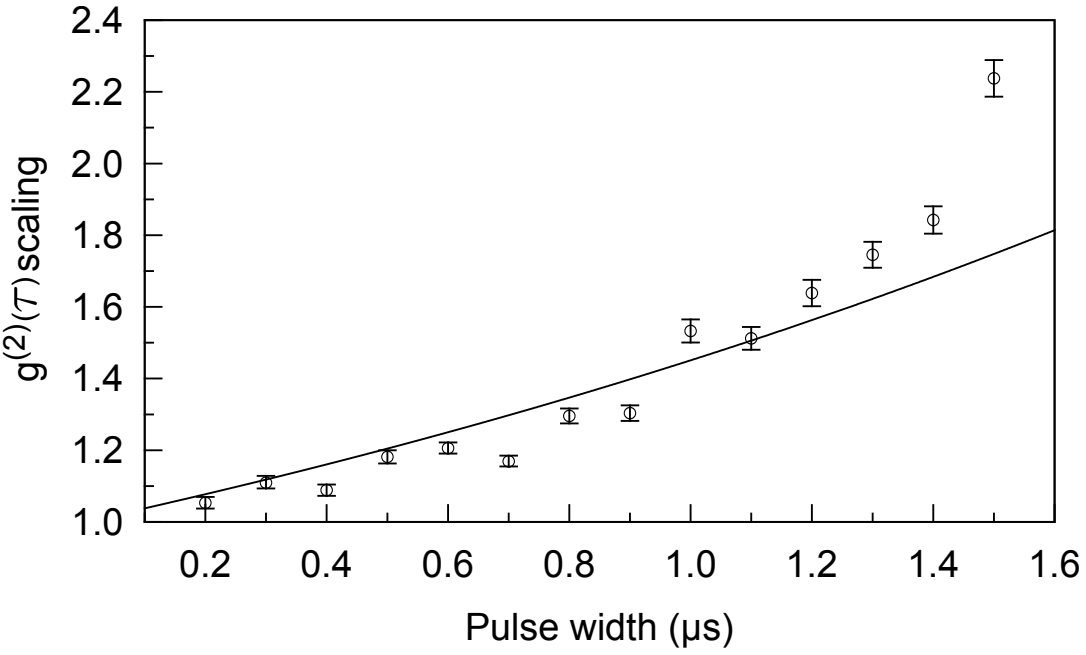

Figure 3.14: Measured scale factor for the amplitude of the oscillations in $g^{(2)}(\tau)$ as a function of feedback pulse width. The continuous line is the expected result from Eq. (3.4).

A different way to carry out the investigation is to fix the feedback pulse width at $3\,\mu$s and change the size of the drive, from the full drive (100%) to smaller values, noting how the amplitude and phase of the oscillations change. Figure 3.15 presents a set of measurements with five different turn-off ratios. As the background suppressed in this figure is different for each trace, the distance between the mark for $g^{(2)}(\tau) = 0$ and the bottom of the frame (about 0.1) shows the maximum amount we had to suppress. Once the drive returns to its starting level the changes in the

amplitude and phase of the oscillations are significant, particularly for the 5% case, and ordered according to color as we would expect.

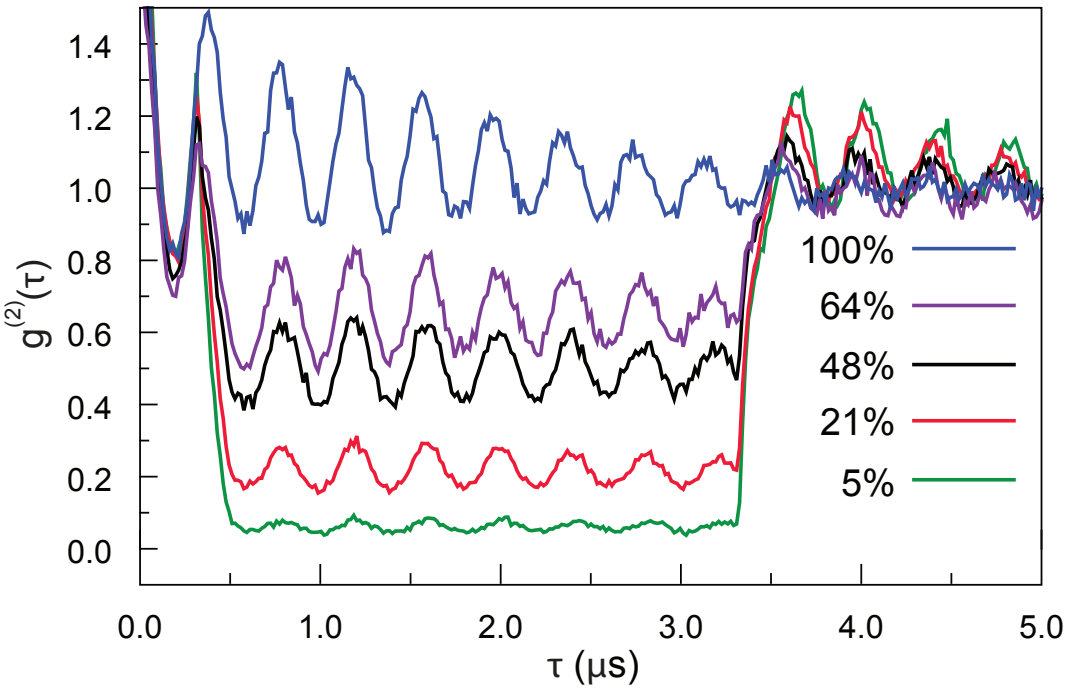

Figure 3.15: Measured conditional intensity, $g^{(2)}(\tau)$, with fixed feedback pulse length ($3\,\mu$s) and variable amplitudes as indicated by the color code. For an effective atom number $N_{\text{eff}} = 0.4$, rotation of 1.2° at HWP, and mean number of photons in the driven cavity mode of $n = 1.3$.

Figure 3.16 shows how the amplitude of the frequency component in Fourier space of the recovered oscillations, scales as a function of normalized drive intensity (normalized against the no feedback case). It analyzes the data runs of Fig. 3.15. If we completely turn the drive off, we obtain the largest amplitude, as observed both in the simulation of the experiment. With the drive turned off for $3.0\,\mu$s, the largest amplitude we observe is more than a factor of three greater than in the continuously

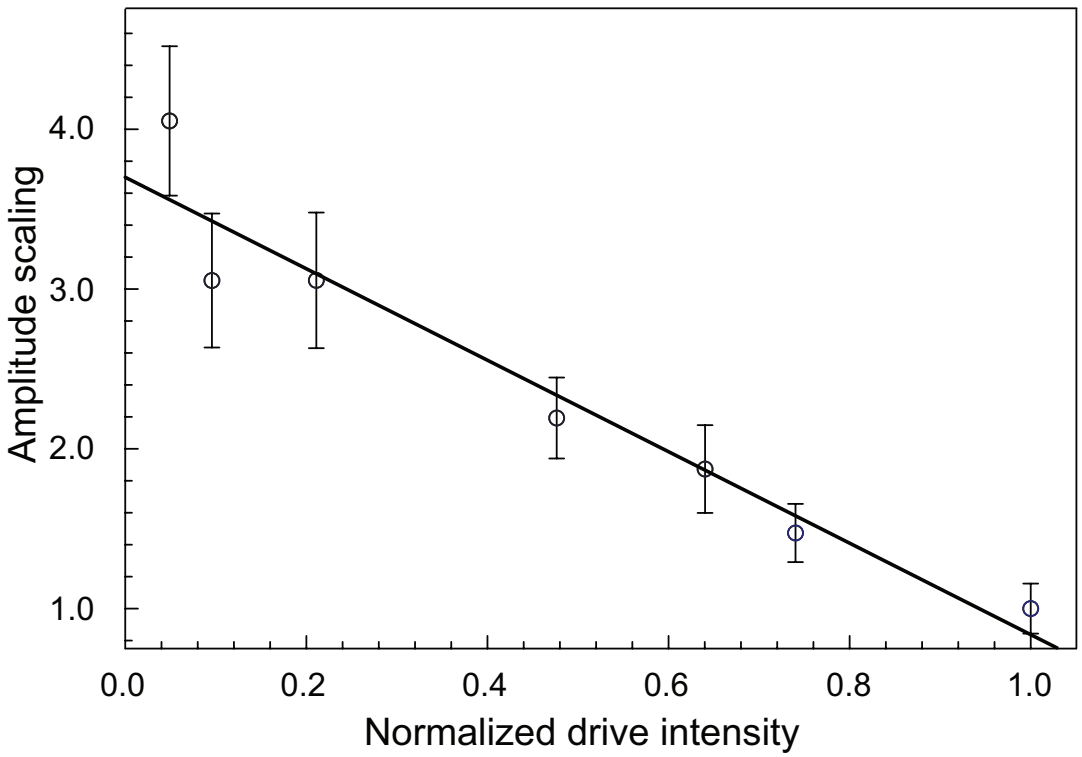

Figure 3.16: Amplitude of the recovered oscillation as a function of normalized feedback intensity after $3\,\mu$s of lower drive. We take a linear fit with reduced $\chi^2 = 0.732$

driven case. The discrepancy between the results of Fig. 3.13 and Fig. 3.16 stems from the slightly stronger drive used in the latter and the analysis is different.

Figure 3.17 shows the phase shift as a function of normalized intensity (obtained by calculating the discrete Fourier transform of the recovered oscillations). For the smallest drive (about 5%) the phase shift differs by more than 2 radians compared to the continuously driven case. The effective frequency shift is of the order of 100 kHz per drive photon in the cavity which is in agreement with a calculation for $n = (1.3 \pm 0.4)$ using Eq. 2.8 that yields (96 ± 7) kHz. The continuous line in Fig. 3.17 is to guide the eye.

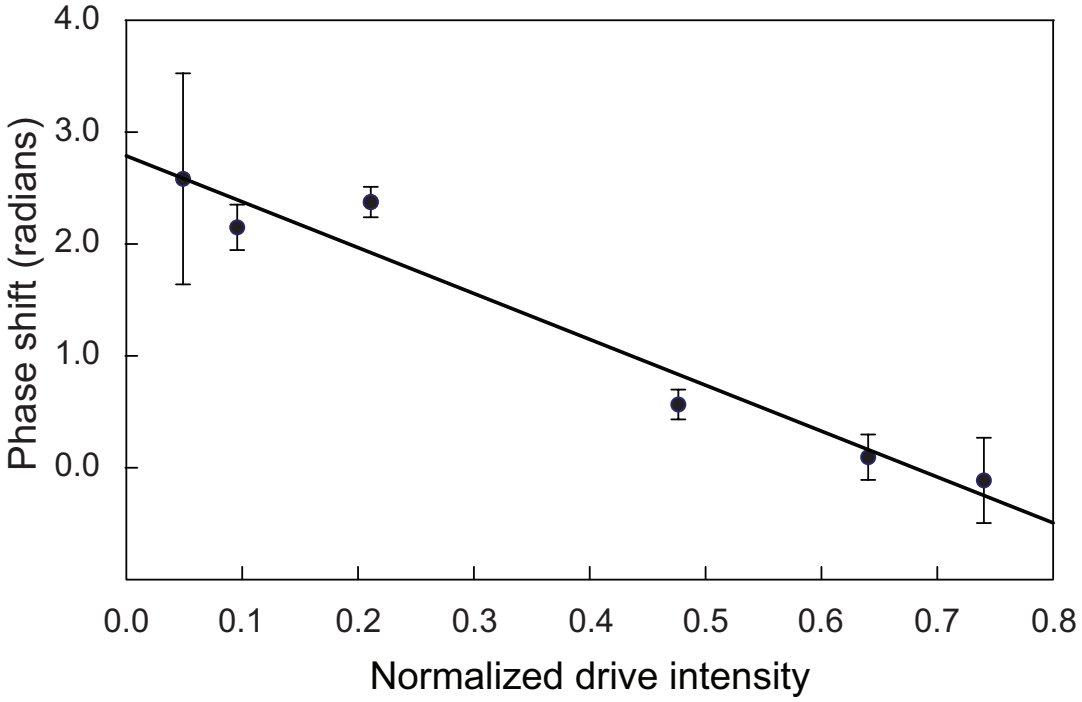

Figure 3.17: Phase shift as a function of normalized feedback intensity after 3 μs of lower drive. The line is just a guide for the eye

3.2.4 Discussion

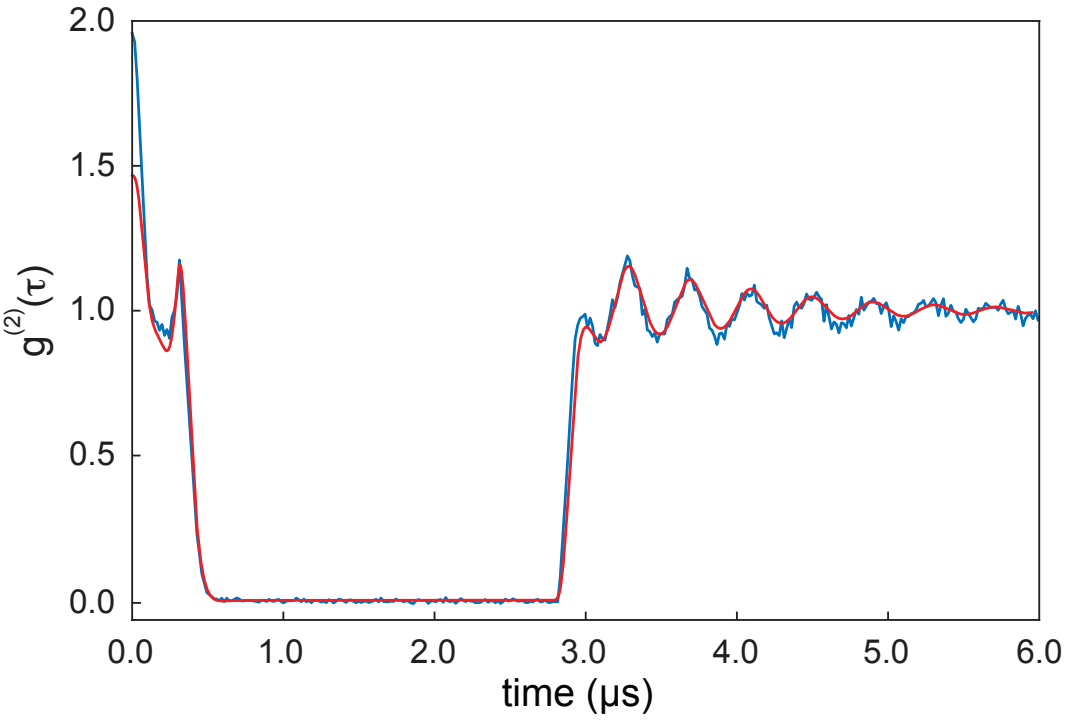

Figure 3.18: Comparison of theory and experiment for controlled excitation. The fit uses effective atom number $N_{\text{eff}} = 0.55$, a rotation of 1.2° at HWP, mean atomic speed $v_{\text{p}} = 13.5\,\text{ms}^{-1}$, a deviation of the atomic beam from perpendicular to the cavity axis $\theta = 0.017\,\text{rad}$, and mean number of photons in the driven cavity mode $n = 1.21$.

The comparison with theory starts with a numerical simulation of the experiment in the absence of feedback to obtain the best parameters for the effective number of atoms, number of photons in the driven mode, average atomic velocity, and the angle between the atomic beam and cavity axis. We make this fit after subtracting from the experimental data any background that prevents the signal

from going to zero when the drive goes to zero, as is done for all the data figures in our results section. We first adjust the background following a procedure similar to the first stage [Fig 3.10(a) and (b)] of the fitting process. The amount of background suppression is equal to the distance between the mark for $g^{(2)}(\tau) = 0$ and the bottom of the figure frame (about 0.05).

Using the fit parameters we calculate the controlled case. Fig. 3.18 shows an example of the results. The qualitative features of the data are all present in the model. Quantitatively, the model captures the phase shift and does an excellent job with the time constant of the cavity, which controls the decay and the rise of the signal when the pulse is applied. The difference between at $\tau = 0$ may come from unaccounted contributions from multiple atoms and/or additional background. Modeling all decoherence processes is difficult; the model captures most of the decoherence, but makes a slight overestimate as the figure shows. The decoherence rate is very sensitive to the atomic velocity distribution, which is difficult to reproducibly control in the experiment to better than ten percent.

Considering comparisons with earlier work, the evolution of the ground state coherence takes place on time scales that allow implementation of feedback protocols with available laboratory equipment. This broadens the scope for experimental exploration compared to the hardware (time response) limitations of the quantum feedback previously implemented on the vacuum Rabi splitting [28, 30]. Working with this same ground state coherence we have shown in Ref. [46] how it is possible to modify the behavior by giving some time dependence to the drive. The combination of that idea with the current results points to new directions, which include the

possibility of incorporating direct RF drives of the Larmor oscillation.

3.2.5 Conclusions

We have shown in this work the idea pioneered by Ramsey [47] of letting quantum coherence evolve in the dark, is valid for conditional coherences, those not visible in the mean transmitted light and requiring the measurement of higher-order correlations for their study. Our use of feedback to counteract and measure the effects of Rayleigh scattering (both frequency shift and decoherence) shows that the qualitative behavior of our system is well understood, while we continue to better our quantitative understanding and detailed modeling. The reported protocol is simple, robust, and can improve the lifetime of a spontaneously generated coherence by a significant amount. It is an advance along the path to a new class of quantum feedback and control.

Chapter 4: Construction of new apparatus

This is a description of recent improvements to enhance our experimental apparatus.

Our goal is to further enhance the intra-cavity interactions between the electromagnetic field and increase the number of atoms at any given time in the cavity mode. This will open the parameter space that we can explore and improve the signal to noise ratio achievable in a second. We achieve this by building a new, improved, optical cavity and a new atomic beam source.

We have built a new vacuum chamber with improved geometry and capabilities. The goal is to make the apparatus more versatile and easier to use in future explorations of the physics in cavity QED, including the implementation of more elaborate control protocols than the one described in Chap. 3.

4.1 Optical cavity

A high finesse (low loss) resonator lies at the heart of every optical cavity QED apparatus. The transmission coefficients for the mirrors used in the resonator may be as low as a few parts per million, reducing the absorptive losses to this level is a great experimental challenge [48, 49].

4.1.1 Limitations

Our old cavity [50] (brief descriptions in Sec. 3.1.2 and Sec. 3.2.2) suffers from higher than expected losses, reducing its finesse by about a factor of two from the calculated value based only on the transmission of the cavity mirrors.

The mirrors that form this cavity are part of a large batch of mirrors our group sent to Research Electro-Optics (REO) in Boulder, CO to apply highly reflective coatings nearly two decades ago. REO guaranteed transmissions of $T_1 = 15$ ppm and $T_2 = 270$ ppm for the particular mirrors in question.

We expect a finesse of $\mathcal{F} = 21000$ from the above transmission parameters. We can also estimate the linewidth (FWHM) of $2\kappa/2\pi = \text{FSR}/\mathcal{F} = 3.2$ MHz for a separation of 2.2 mm between the mirrors. Our experimental measurements show $\mathcal{F} = 12000$ and a FWHM linewidth of 5.6 MHz [51]. We believe this additional loss stems, primarily, from glue residue deposited on the mirrors during the cavity building process, but also coating aging.

The dipole coupling strength for the field in this cavity and ^{85}Rb atoms at a wavelength matching the energy of the D_2 line transition yields a value of $g/2\pi = 1.5$ MHz using Eq. 4.4 and weighing the Clebsch-Gordan coefficient for the transition $|F = 3, m_F = 0\rangle \rightarrow |F' = 4, m'_F = 0\rangle$. We wanted to increase this quantity where the coupling rate between a single atom is similar to the decay rates through spontaneous emission and escape of the cavity (intermediate coupling regime).

4.1.2 Construction process

Our new cavity has small and well-characterized losses, as well as almost a factor of two stronger coupling to the atoms and enhanced vibration isolation.

Our experiments require great control of the mode of the electromagnetic field inside the cavity. It is very important to have great precision in the positioning of the mirrors that form the resonator. We use shear piezoelectric transducers (PZTs) from Channel Industries, Inc. for this purpose. We use lead zirconate titanate as material, specifically model C-5800. We start by using a conductive epoxy glue to adhere these piezos to a non-magnetic stainless steel base (with a reasonably large hole in the middle), taking care to orient them along the direction of motion (shear). After the glue is dry, we also attach thin copper wires to the top of the PZTs (LIVE) and to the stainless steel base (GND) as can be seen in Fig. 4.1 and 4.4).

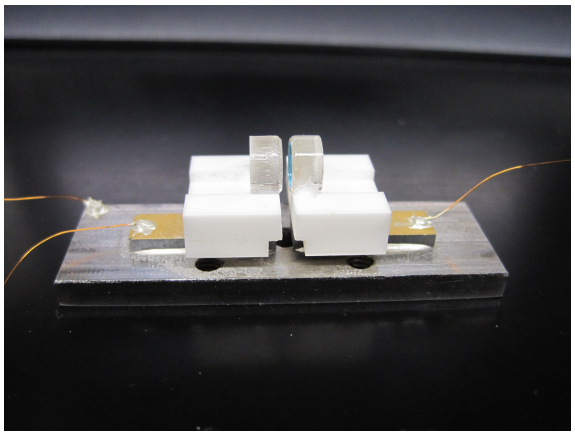

Figure 4.1: Side picture of a Fabry-Perot cavity built using the procedure outlined in this section.

Two spherical mirrors with Research Electro-Optics (REO) high-reflectivity

coatings form the cavity. We glue these circular mirrors on V-shaped pieces of MACOR, a low-outgassing, machinable ceramic that can withstand high temperatures and provides electrical isolation. Our goal is to obtain a small separation between the mirrors of the cavity. It is important to glue the mirrors on the bases so that they stick out noticeably. This is the most delicate gluing phase. If not careful it is rather easy to touch the mirrors with the tool used to apply the glue.

We glue the input mirror and its base to one of the PZTs. We use a crane-like mount (Fig. 4.2) to hold the output mirror by its MACOR base and place it as shown in Fig. 4.3.

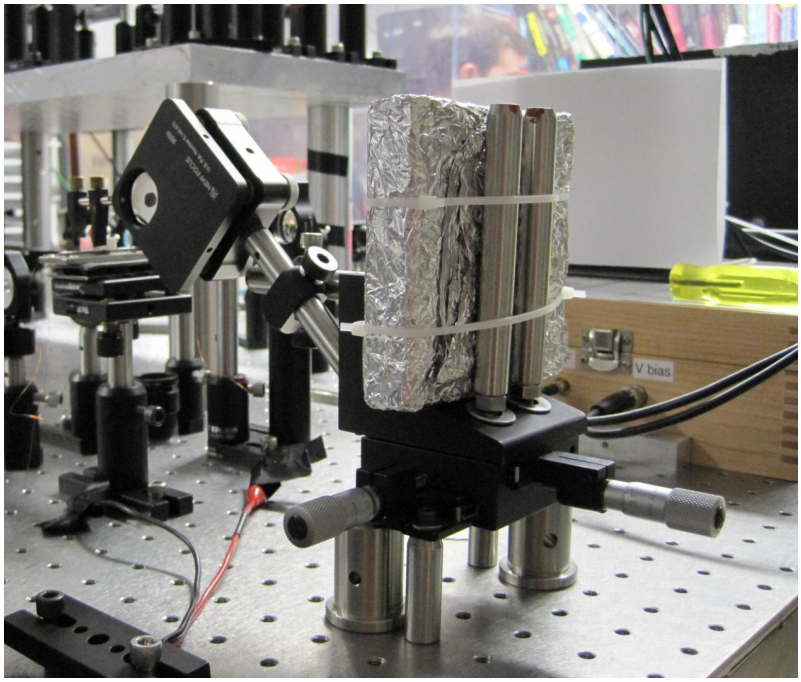

Figure 4.2: Full structure for the gluing of the new cavity

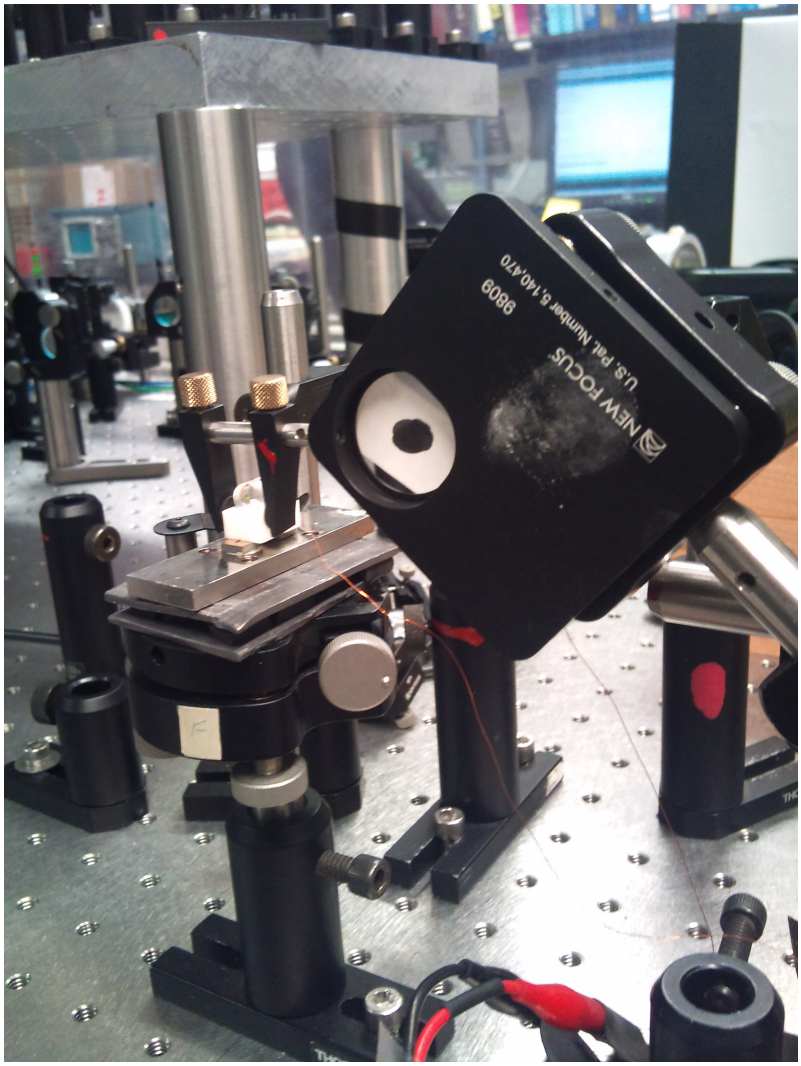

Figure 4.3: Crane holding output mirror of cavity previously glued to MACOR V-block

We set up a Helium-Neon diverging laser beam using a short focal length lens before gluing the output mirror and V-block base. We aim this beam at the input mirror, so that the back reflection overlaps the incoming beam and also the beam diameter covers the mirror diameter (7 mm). We also connect a high voltage ramp power supply to the input mirror PZT and ground. The PZT displacement as a

function of applied voltage is given by:

$$\Delta x = d_{15} V \tag{4.1}$$

where $d_{15} = 390^{-12}$ m/V, for material C-5800. We can expect displacements of roughly $\lambda/2$ for an amplitude of the ramp of 1 kV. We use the crane to move the output mirror to a position such that we can see a changing interference pattern on the output beam (moving Fabry-Perot fringes). This pattern is localized and corresponds roughly to the position of the TEM_{00} mode. We place the interference as centered as possible using the crane. We simply lift the mirror to allow room to apply glue and then lower the mirror again, taking care of re-positioning the interference rings in the middle of the output beam. We constantly monitor the output screen for changes and use the crane tilt knobs to re-center the pattern during the curing of the glue.

We use only adhesives that NASA rates as low-outgassing [1] based on percent total mass loss at low pressure such as Loctite Hysol 1C. These glues are compatible with high vacuum requirements ($\sim 10^{-8}$ Torr or lower). We use EPO-TEK H20E, a silver-filled electrically conductive low-outgassing epoxy, to bond the PZTs to wires and the stainless steel base. Figure 4.4 shows a picture of the finished cavity.

[1] NASA outgassing data for selecting spacecraft materials 06/01/2011 `http://outgassing.nasa.gov/`

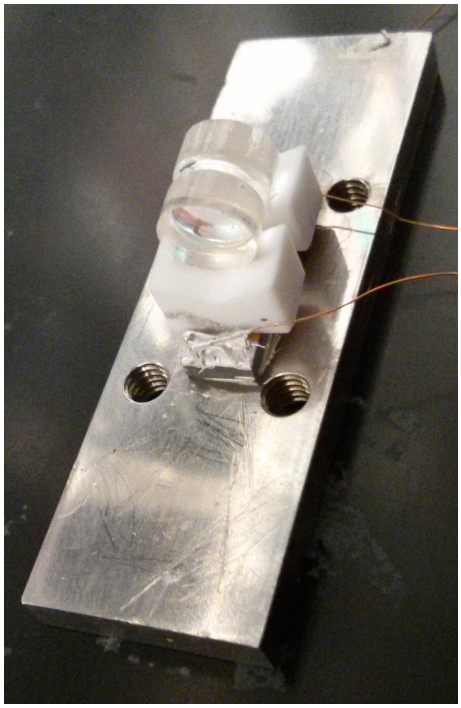

Figure 4.4: Picture of new Fabry-Perot cavity

4.1.3 Properties

The objectives of building a new optical cavity is two-fold: experimentally obtain a projected finesse of ~ 20000 and enhance our coupling strength.

We are aware of the aging effects in the reflective coatings of the mirrors, so we first determine carefully the new transmissions from a batch of mirrors with promising advertised parameters.

We choose a pair of mirrors with the following properties: $T_1 = 242 \pm 2.4$ ppm and $T_2 = 9 \pm 1$ ppm and radius of curvature of both mirrors of 45 cm. We use a 5 mW, 780 nm laser beam and a mounted optical power meter to measure the intensity transmission coefficient T directly. A 780 nm filter reduces background light into the

detector to below 0.01 nW. After measuring the power of the unimpeded beam, we move a mirror into the path of the laser such that it is incident on the coated side, and the mirror reflects the majority of the power back through the optical isolator before the laser. Finally, we use an aperture after the mirror to carefully block as much of the scatter as possible (without clipping the transmitted beam itself), and record the intensity of transmitted light. Taking the ratio of the transmitted optical power to the incident optical power (over several independent trials), we determine the current transmissions of the high-reflectivity mirrors. The labeled T values for the mirrors did not always agree with our measurements [52].

We start the building process as outlined before with the goal of having a intra-cavity mirror separation of ~ 1 mm. We replace the HeNe laser with a 780 nm laser beam frequency modulated by an EOM at a known value, for example 230 MHz. The lens should now be chosen so as to mode-match the beam with the predicted mode-waist in the cavity, $w_0 = 58$ μm. We place a detector (Photo-multiplier tube, PMT) at the output. We connect the PMT to an oscilloscope, triggering on the HV ramp. This shows the allowed transmission modes through the resonator. Careful alignment and mode matching are necessary to couple the light mostly into the TEM_{00}.

We can use the known frequency separation between carrier and side band (*e.g.* 230 MHz) provided by the fiber EOM in the experimental setup to measure, with the oscilloscope, the linewidth (FWHM) of the cavity. We can estimate the FSR from the rough estimate of the separation between the mirrors. This yields a value of finesse of the order of 20000, as we want. The reason we do not pursue

more accuracy with this method is because we know the environment (cavity in air with no mechanical isolation) has an adverse effect on the linewidth. We proceed to place our cavity in vacuum in order to minimize the effect of the environment.

We discuss the vacuum chamber assembly in Sec. 4.3. The estimation of our resonator properties *in vacuo* follows exactly the procedure described above, except we find indirectly the value of the FSR.

We measure on the oscilloscope the frequency difference between two TEM modes. Our cavity is in the non-confocal regime. The radius of curvature is much larger than the mirror separation $R >> \ell$, then this frequency (in vacuum) is given by [53]:

$$\Delta\nu = \frac{c}{2\pi z_0} \tag{4.2}$$

where z_0 is the Rayleigh length of the cavity mode. It depends on the resonator mirror separation, and for a symmetrical cavity as ours, it is related by:

$$z_0^2 = \frac{(2R-\ell)\ell}{4} \tag{4.3}$$

Solving Eq. 4.2 for z_0, substituting it in Eq. 4.3 and solving for ℓ yields an intra-cavity mirror separation of 0.790 ± 0.001 mm. It is easy to compute the FSR $= c/2\ell = 189.6 \pm 0.2$ GHz. We also measure on the scope a value for the linewidth (FWHM) of $2\kappa/2\pi = 9.09 \pm 0.01$ MHz. A direct measurement of FSR is possible, but this makes the EOM side bands very difficult to resolve on an oscilloscope, making it complicated to correctly convert FSR to frequency units.

Our estimate of the finesse is $\mathcal{F} = \mathrm{FSR}/4\pi\kappa = 20863 \pm 35$ by combining two numbers, which reaches our goal. This number is a reasonable estimate, though it

is likely to increase as our cavity length stabilization controls improve.

We combine Eq. 1.1 and Eq. 1.2 to obtain a simple expression for calculating the dipole coupling for our cavity:

$$g = \frac{\mu}{\hbar}\sqrt{\frac{\hbar\omega}{2\epsilon_0 V}} \tag{4.4}$$

The dipole moment contains the appropriate Clebsch-Gordan coefficient for the transition involved (not included in Eq. 4.4) [54]. Tables 4.1.3 and 4.1.3 show the values for $g/2\pi$ as well as important figures of merit for the most important transitions.

	$F=3$	$F'=4$	CG	$g/2\pi$ [MHz]	C_1	n_{sat}
π	$m=0$	$m'=0$	$-\sqrt{2/7}$	2.4	0.21	2.1
	$m=3$	$m'=3$	$-\sqrt{1/8}$	1.6	0.09	4.8
σ^+	$m=0$	$m'=1$	$\sqrt{5/28}$	1.9	0.13	3.3
	$m=3$	$m'=4$	$\sqrt{1/2}$	3.2	0.37	1.2

Table 4.1: Clebsch-Gordan (CG) coefficients, single-atom coupling constants g and cooperativities C_1, and saturation photon numbers for different transitions in the D_2 line of ^{85}Rb from $F = 3 \rightarrow F' = 4$ for different drive polarizations (π or σ^+)

	$F=2$	$F'=3$	CG	$g/2\pi$ [MHz]	C_1	n_{sat}
π	$m=0$	$m'=0$	$-\sqrt{3/10}$	2.5	0.22	2.0
	$m=2$	$m'=2$	$-\sqrt{1/6}$	1.8	0.12	3.6
σ^+	$m=0$	$m'=1$	$\sqrt{1/5}$	2.0	0.15	3.0
	$m=2$	$m'=3$	$\sqrt{1/2}$	3.2	0.37	1.2

Table 4.2: Clebsch-Gordan (CG) coefficients, single-atom coupling constants g and cooperativities C_1, and saturation photon numbers for different transitions in the D_2 line of ^{87}Rb from $F=2 \rightarrow F'=3$ for different drive polarizations (π or σ^+)

4.1.4 Vibrations

We use a method of impedance mismatching in which the stainless steel cavity mount sits atop a stack of materials with very different resonant frequencies, such that vibrations do not easily propagate through the entire stack, to improve the mechanical decoupling of the cavity. The materials include lead, copper, and Sorbothane (a shock absorbing synthetic viscoelastic urethane polymer) [2]. In order to find the optimal configuration of the materials, we place the cavity base atop a test stack and use a PZT attached to the base as a microphone, connecting its output to a spectrum analyzer (Stanford Research Systems SR770 FFT Network Analyzer). We then strike the tabletop with a hammer, delivering controlled "delta function" impulses, several times over a span of ten seconds. We collect PZT voltage and av-

[2]Sorbothane manufacturer's website 06/01/2011 `http://www.sorbothane.com/`

erage the spectrum over a range of frequencies from 0 to 100 kHz, and we compare dozens of different combinations of damping materials.

We obtain a drastic improvement to the effectiveness of the damping stack by altering the geometry of the Sorbothane layer, based on advice from the manufacturers of Sorbothane. Instead of a solid sheet of Sorbothane, we cut the material into twelve roughly 0.25-inch squares, and space the squares out over the area of the damping stack. As shown in Fig. 4.5, the small pieces of Sorbothane make this geometry significantly more effective at damping, as they have more room to deform sideways and dissipate vibrational energy.

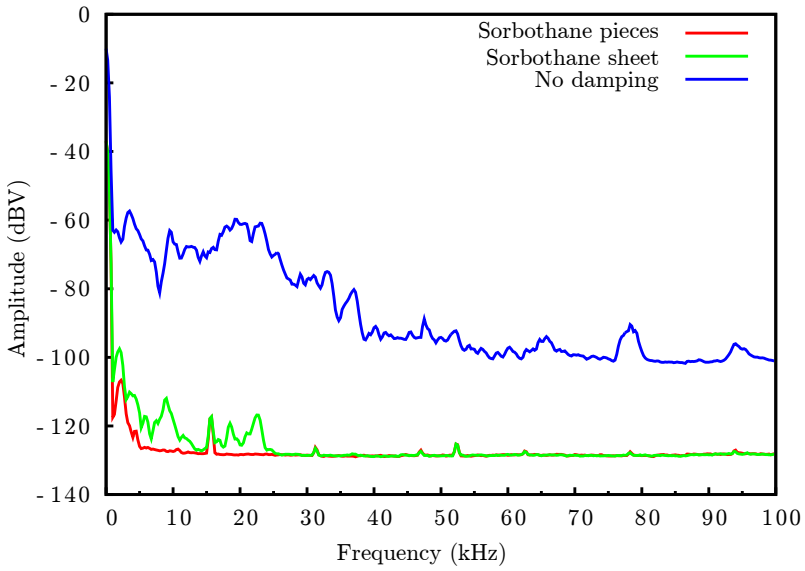

Figure 4.5: Power spectra after impulse excitation. Damping layers: Lead-Sorbothane-Lead.

4.2 Atomic beam

We implement a Low Velocity Intense Source [38] (LVIS) of ^{85}Rb atoms. We achieve this by unbalancing a magneto-optical trap (MOT). The typical MOT requires six laser beams, a pair for each direction. A common setup, for each pair, uses a combination of a QWP and mirror to retro-reflect the incoming beam.

A slow moving atomic beam, under certain circumstances, can transit through a small hole in the QWP and mirror combination of one of the pair of laser beams as shown in Fig. 4.6. There is no light reflected from the hole so the scattering force in that direction vanishes, subjecting the atoms to the scattering force from the push beam. To avoid complications we choose the Z-axis (direction of gravity). This requires that our QWP and mirror with a hole be inside our vacuum chamber.

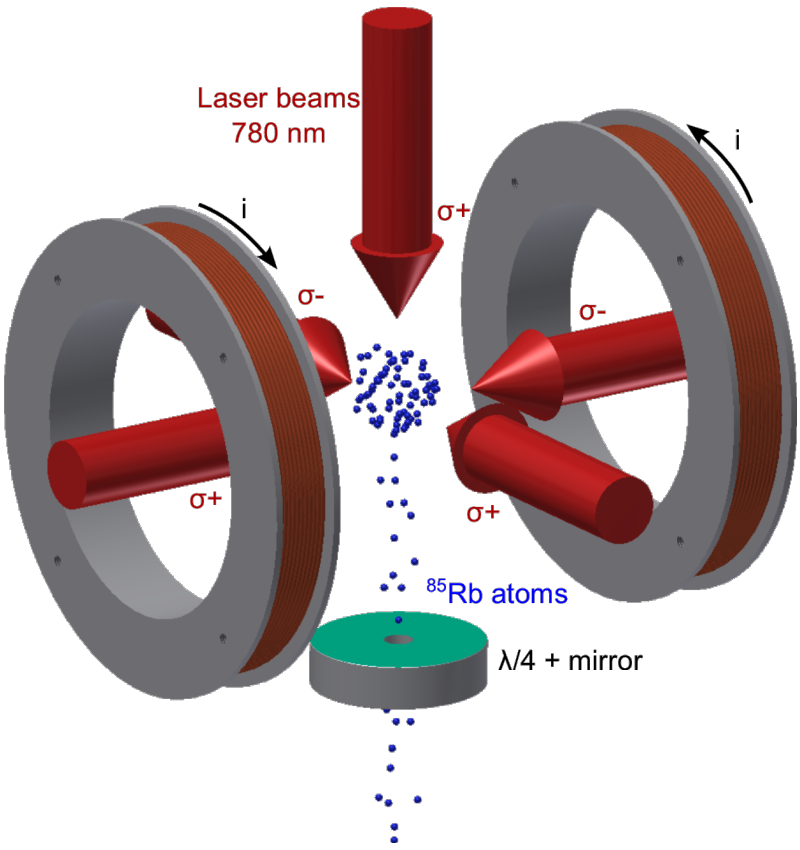

Figure 4.6: Low Velocity Intense Source (LVIS) diagram: An atomic beam can transit through a small gap in one of the trap beams.

4.2.1 Limitations

The old setup allowed us to work under optimal circumstances with one or two effective atoms in the cavity (we were not able to resolve the vacuum Rabi splitting). We started with a rather small MOT; The laser beams forming the trap were no more than 20 mm in diameter, limited by the size of the windows on the vacuum chamber. The gradient of the magnetic field near the trap center was not well known. The vacuum pressure was poor as inferred by observations of trap

lifetimes in the order of hundreds of milliseconds.

The aiming of the atomic beam at a cavity is complicated. In the past setup, the previous students assembled the QWP and mirror combination in the most centered way they could find. Then before closing the vacuum chamber, they introduced a thin rod (0.062" in diameter) through the holes of the optics and reaching between the mirrors of the cavity. This technique is risky because it may damage the surface of the mirrors and it is no longer applicable to our new cavity with a mirror separation of 0.79 mm. Complications also arose from a small tilt in the mounting of the *in vacuo* optics.

All the above issues can hurt the flux of atoms in our beam, leading to reduced atomic intra-cavity interactions. We have tried to address most of these issues in the next generation experimental apparatus.

4.2.2 Large Magneto-optical trap

We emulate to a great extent the optimal experimental parameters for the LVIS found by [38].

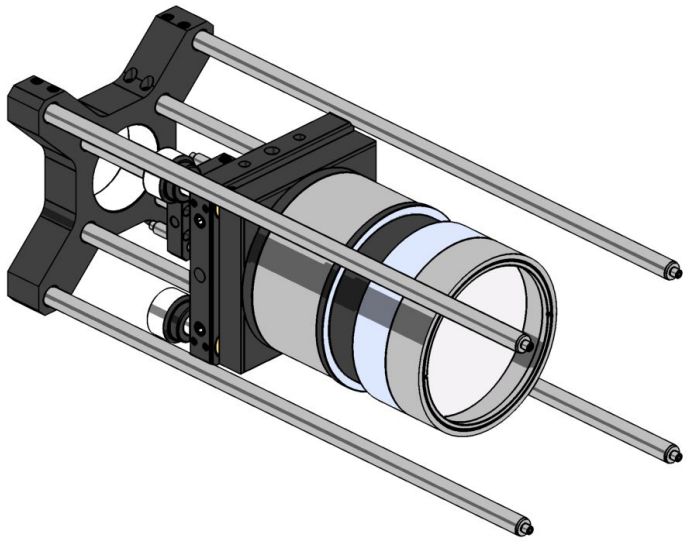

Figure 4.7: 3D CAD exact model of the MOT beam expander system. The kinematic mount in the middle allows tilt even though the mounts firmly attach to our vacuum chamber using the 60 mm cage.

Our first step is to enhance our MOT. We increase the size of our trap beams to 40 mm in diameter, except the top Z-axis beam which we set to 25 mm because of space constraints. We implement an optical system based on work by the research group of Dr. James V. Porto and later refined by fellow graduate student Jiehang Zhang [55] (See Fig. 4.7), to obtain a highly collimated beam of the desired diameter.

We construct a hybrid lens tube and cage mount from easily purchasable items with a few customizations of our own. Figure 4.8 shows a cross section of our mount, displaying several key positions of the optical elements. The optical system starts with a FC/APC PM fiber (based on Corning PM85-U25A) with numerical aperture, NA = 0.12. Shortly after we place a QWP for turning linearly polarized light to

circularly polarized. At a distance from the fiber tip of about 30 mm, we place a 1/2" plano-concave lens with $f = -25$ mm. Then at about 40 mm we put a 2" meniscus lens with $f = 150$ mm followed closely by a 2" plano-convex lens with $f = 150$ mm. We hold the optics in place using retaining rings (not highlighted on image). We use an extra retaining ring as a spacer in the second SM2V10 lens tube that carries the positive meniscus lens. We can buy from Thorlabs, Inc all the parts to assemble this special mount. The only two parts that need customization are KC1-T and SM05T2. The kinematic mount KC1-T does not actually fit inside a 60 mm cage assembly. It is necessary to grind the edges closest to the cage construction rods. The SM05T2 lens tube adapter proves too long, so we can cut it roughly in half.

We use a shear interferometer to optimize the collimation of the beam. We perform adjustments to the position of the SM2V10 variable length lens tube and the fiber output coupler position. We can tweak these two parameters while we monitor the interference fringes and we make them as parallel as possible.

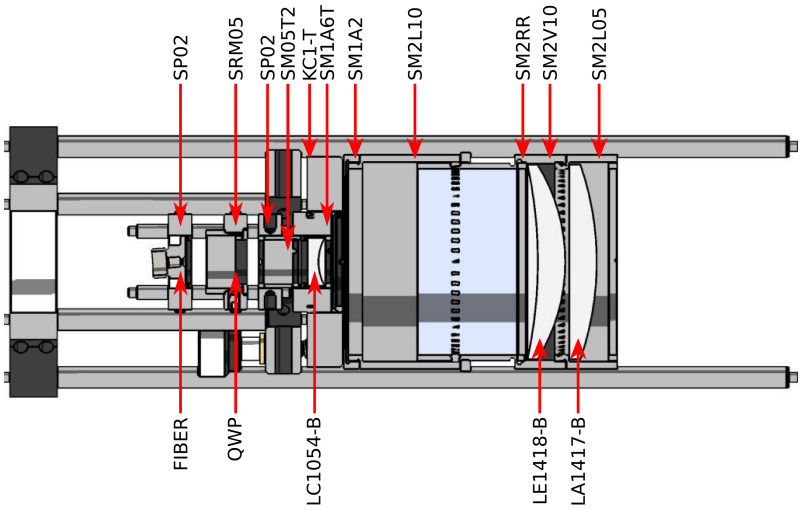

Figure 4.8: Cross section of 3D CAD model of our MOT beam expander optical system.

The 60 mm cage housing the optical system fits into a customized 1/8"-thick "washer" that we pre-attach to the vacuum chamber. This washer, shown in Fig. 4.9, contains machined holes (4-40) for properly mounting both 30 and 60 mm cages as well as some extra 1/4-20 holes not currently in use. This ensures great alignment with the vacuum chamber windows.

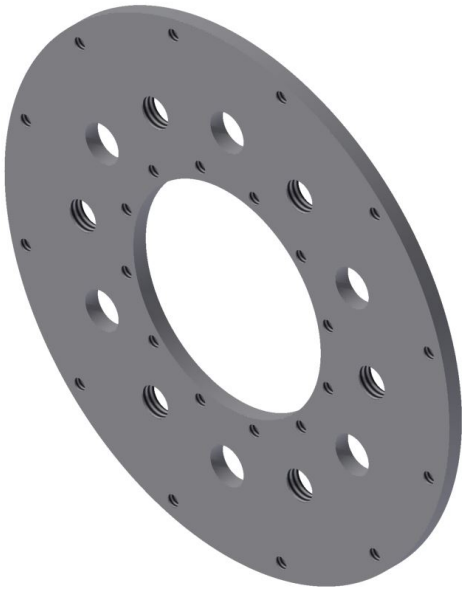

Figure 4.9: Washer for mounting 30/60 mm cage systems to CF 2.75" vacuum viewports.

We use three of these cage optical systems. The other three beams making our MOT come from retro-reflection optics. For the x and y directions we use a simple 60 mm cage holding a 2" large focal length achromatic lens ($f = 1$ m), and also 2" QWP and mirror. We use this lens to help us center our trap, because our reflected beams may have losses despite the anti reflecting coatings in the optics which can shift the position of the trap significantly away from the center.

We have also developed custom-made coils for generating the necessary magnetic fields for a MOT. An aluminum spool holds each of our coils. Figure 4.10 shows a 3D CAD model of the spool and Fig. 4.11 shows detailed dimensions. We

are not concerned now about turning the magnetic coils off and the residual eddy currents that form on the aluminum. We wind two distinct wires in the interest of cutting the resistance of the coil in half, obtaining about 180 turns of 14 AWG wire in total. This comes at the expense of using more current to achieve same field strength. We place them about 14 cm from the center of the chamber along the axis of the coils. Our calculations show an estimated field gradient at the center of the MOT chamber along the coil axis of 3 G/cm and 5 G/cm in the other two directions when using a current of about 7.5 A (on each strand).

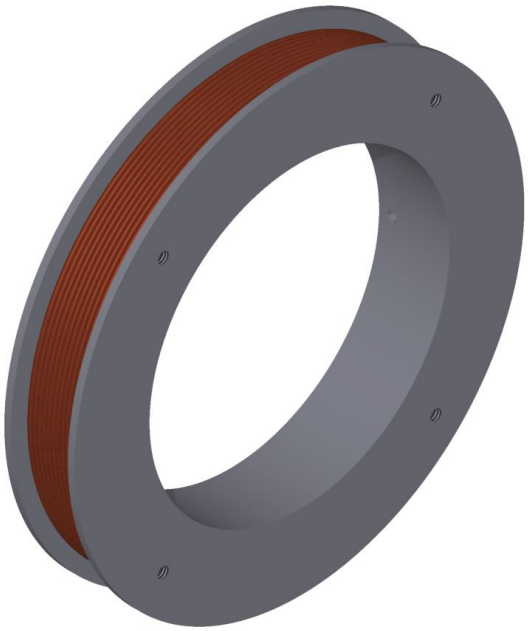

Figure 4.10: 3D CAD exact model of our MOT coil.

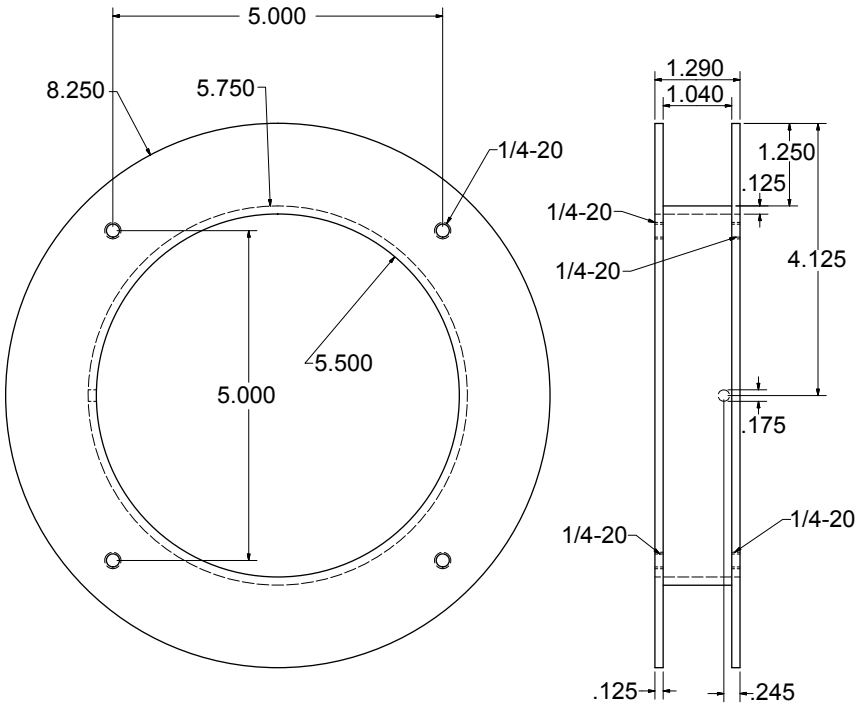

Figure 4.11: Detailed dimensions of MOT coil spool.

4.2.3 Steering

We have limited steering capabilities once we close our vacuum chamber. We have three pairs of large bias coils for shifting the MOT center in each direction and we can steer the laser beams. We are also employing long-focal-length converging lenses in the retro-reflection optics to help us balance the scattering forces and thus allow us to shift the MOT center.

The target for our atomic beam is the mode of the cavity. The dimensions of this target are roughly 0.79 mm by 58 μm. It is crucial to start with a very good initial alignment of the cavity center with the hole in the QWP and mirror and then do the rest by shifting and/or steering the MOT.

4.3 Experimental chamber

Our experiments take place inside a vacuum chamber constructed with commercial pieces from Kimball Physics, Inc. It consists of two main parts or separate chambers: The top chamber that we use to establish our MOT and a lower chamber that houses our optical cavity and where our scientific probes take place. The reasons for requiring a relatively high vacuum (10^{-8} to 10^{-9} Torr) are mainly two: our slow atomic beam (LVIS) can only be realized in an environment with a low collision rate. Our optical cavity, very susceptible to temperature changes, is well insulated from the ever changing environment by the vacuum.

4.3.1 Limitations

Figure 4.12 shows an accurate representation of our old vacuum chamber. It has several significant drawbacks we want to address.

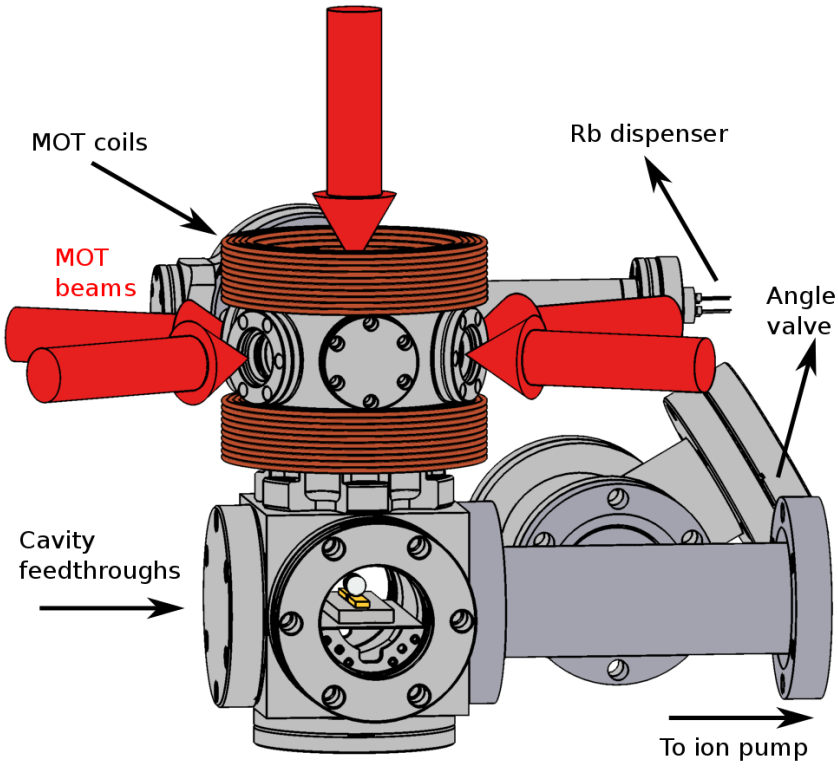

Figure 4.12: Accurate 3D CAD model representation for our first vacuum chamber

One of its greatest problems is the limited optical access. The chamber housing the optical cavity, a 2.75" CF cube, has two of its sides sealed. We use one of this sides for electrical feedthroughs (HV and ground for cavity PZT's) and the other for attaching a Varian 20L ion pump. Also the placement of the optical cavity is not in the center, allowing little to no room for probing the atomic beam before entering the cavity.

We suffer significant problems with stray magnetic fields coming from the pump's magnets, despite our efforts at insulation. This is because our sole ion pump is within its characteristic magnetic dipole size from our cavity chamber, contributing large gradients to the MOT region and to the interaction region where

the cavity resides.

The MOT chamber directly above our cavity chamber (connected by a 2.75" close coupler 1.4" in length - MCF275-ClsCplr-C2-1400) is a small 2.75" spherical hexagon (MCF275-SphHex-C2A6). This leaves small 1.33" viewports for establishing laser beams for a MOT. The flux of the atomic beam is adversely affected by a small trap (small capture rate). The vacuum conductance between this chamber and the cavity chamber is rather small because of the QWP and mirror with a hole. This can hurt the pressure on the top chamber, which also translates into a lower atom flux.

4.3.2 Vacuum

Figure 4.13 shows our new generation vacuum chamber. It addresses the problems of our old chamber and serves to house our new optical cavity whose properties we describe in detail in Sec. 4.1.

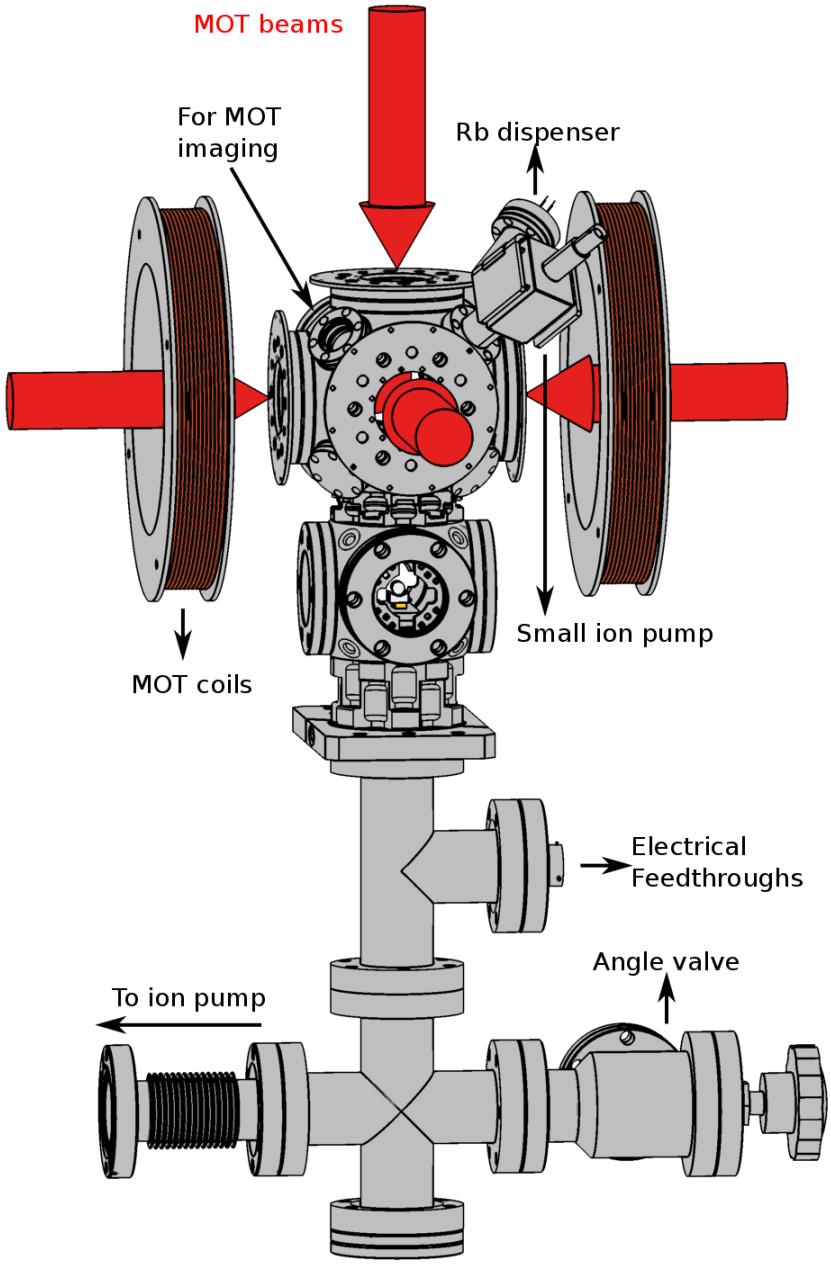

Figure 4.13: Accurate 3D CAD model representation for our new vacuum chamber

Our new chamber provides ample optical access. It is now possible to align a laser beam on the side of our cavity. This is an ideal location for our optical pumping beam (see Sec. 4.4). Additionally the cavity is at a height on the same level as the

center of the viewport. We manage to do this by routing electrical feedthroughs through the bottom instead of the side. We also connect our 20 L ion pump from below using a CF "tee", a four-way cross and a flexible bellow. Placing the ion pump this far away from our cavity chamber greatly reduces the stray magnetic field problem without compromising the vacuum too much. We now have a second vacuum pump on the top chamber. Despite the considerable amount of hardware and wires inside, we still have optical access from below just as before.

The MOT chamber is now an extended spherical cube from Kimball Physics, Inc (MCF275-SphCube-C6A8). This piece has six 2.75"-inch CF ports ideal for our large 40-mm trapping laser beams. It also comes with eight 1.33" CF ports along the cube diagonals. We use the top four ports for imaging the MOT (2), placing our rubidium dispenser rods and adding an extra 3 L ion pump as shown in Fig. 4.14. This small pump is manufactured by Gamma Vacuum and the model number is 3S-CV-1H-5K.

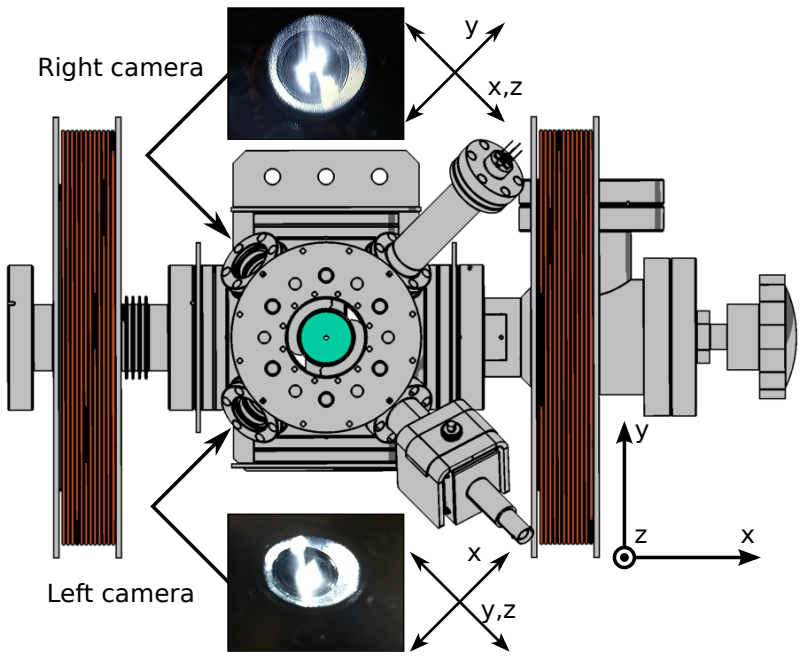

Figure 4.14: Top view of new vacuum chamber showing detail of the mirror with the hole and the orientation of the images we obtain from the MOT

The assembly process requires time and careful work. The first step is to make sure all parts are as clean as possible, following common practices developed at JQI. The most difficult stage is the wiring of the feedthroughs, while maintaining optical access from the bottom. The number of wires we need to route is fifteen. Each RF/Microwave coil needs two, and there are four coils: two along the axis of the cavity, one on its side and one around it. The magnetometer requires four wires and the PZT's of the cavity need the last three. We keep the wires away from the center by constructing a "wall" to guide them. Figure 4.15 shows an accurate representation of it. We make the wall using internal mounting parts and eV parts from Kimball Physics, Inc. The close coupler (MCF275-ClsCplr-C2-1400) provides

the support for a pair of groove grabbers (MCF275-GrvGrb-CB03). These grabbers posses mounting holes for clamping two 6-in stainless steel rods (SS-RO-C-6000). The other two rods are attached to the assembly using a modified screw clamp assembly (SS-SCA-C5). The modification of this part consists in cutting the last clamping hole. We do this by simply grinding the part. This part becomes a clamp for four rods instead of five. Not shown on Fig. 4.15 is the kapton tape we use to cover the holes in between the rods, effectively making a wall and insulating the conductive rods from the wires.

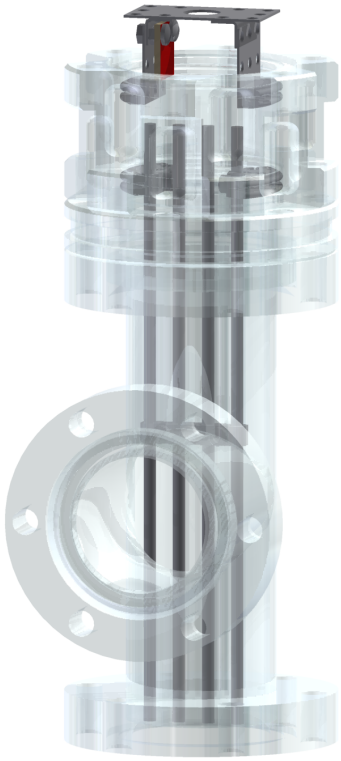

Figure 4.15: Translucent view of the chamber section just below the cavity chamber. "The wall" formed by 6-in long stainless steel rods held in place by groove grabbers holding on to the close coupler part. Pictured also is the magnetometer board (in red) attached to the structure that serves as a base for the cavity.

The detailed wiring order is in Appendix A. Figure 4.16 shows the cavity and coils in place after we finish the wiring and we attach the cavity chamber (MCF275-SphCube-C6). The next step is to hold this part of the chamber to a suspended optical breadboard using an external bracket (MCF275-ExtBrkt-LS). This bracket fits into a mounting flange (MCF275-MtgFlg-C2) located between the close coupler and the "tee". We then attach a 2.75" cross to the "tee", seal the bottom with a

viewport and attach an angle valve to one of the remaining open ends and a flexible bellow to the other. We connect the flexible bellow to our 20L varian ion pump.

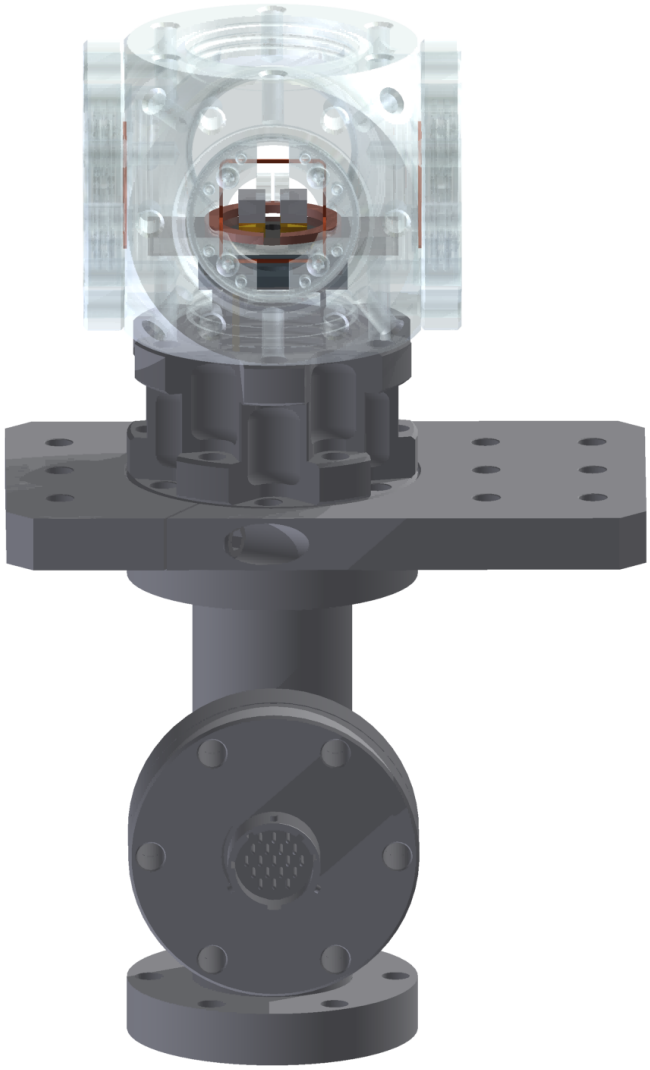

Figure 4.16: Translucent view of the cavity chamber. The cavity rests on three layers of vibration insulation (Pb - Sorbothane pieces - Pb) surrounded by RF/Microwave coils. Note the closed flange with feedthroughs connector and the external bracket for supporting the whole chamber on an optical table.

The last step in the assembly of our vacuum chamber is the joining of our MOT chamber to the cavity chamber. We attach a very long cage system directly above the cavity chamber. This cage system simply helps us implement a very well aligned vertical laser beam. We then use a power meter below our vacuum system to measure the power of the laser beam transmitted in between the cavity mirrors. We maximize the transmitted power by gently moving our optical cavity. This ensures the cavity is reasonably centered with respect to the vacuum chamber. We finally close the cavity chamber using regular 2.75" vacuum viewports with glass AR coated.

We attach a similar cage system to our MOT chamber separately. This takes place on the side directly opposite to the side holding the QWP and mirror with hole. The purpose of this procedure is to ensure that the mechanism holding the optics does not introduce a significant tilt in the reflected beam. We use a cylindrical clamp with nearly one-inch diameter to hold the optics (MCF275-GrvGrb-CYL1000). This special clamp is manufactured by Kimball Physics, Inc. It allows mounting on grabber grooves present in our vacuum chamber parts, also manufactured by the same company. We measure a tilt angle of under one degree. Figure 4.17 pictures the cavity and the hole in the mirror. The separation between the hole and the center of the cavity is about 2 cm. The total approximate distance between the MOT center and the cavity is nearly 10 cm. The thickness of the QWP plus the mirror is 1.3 cm.

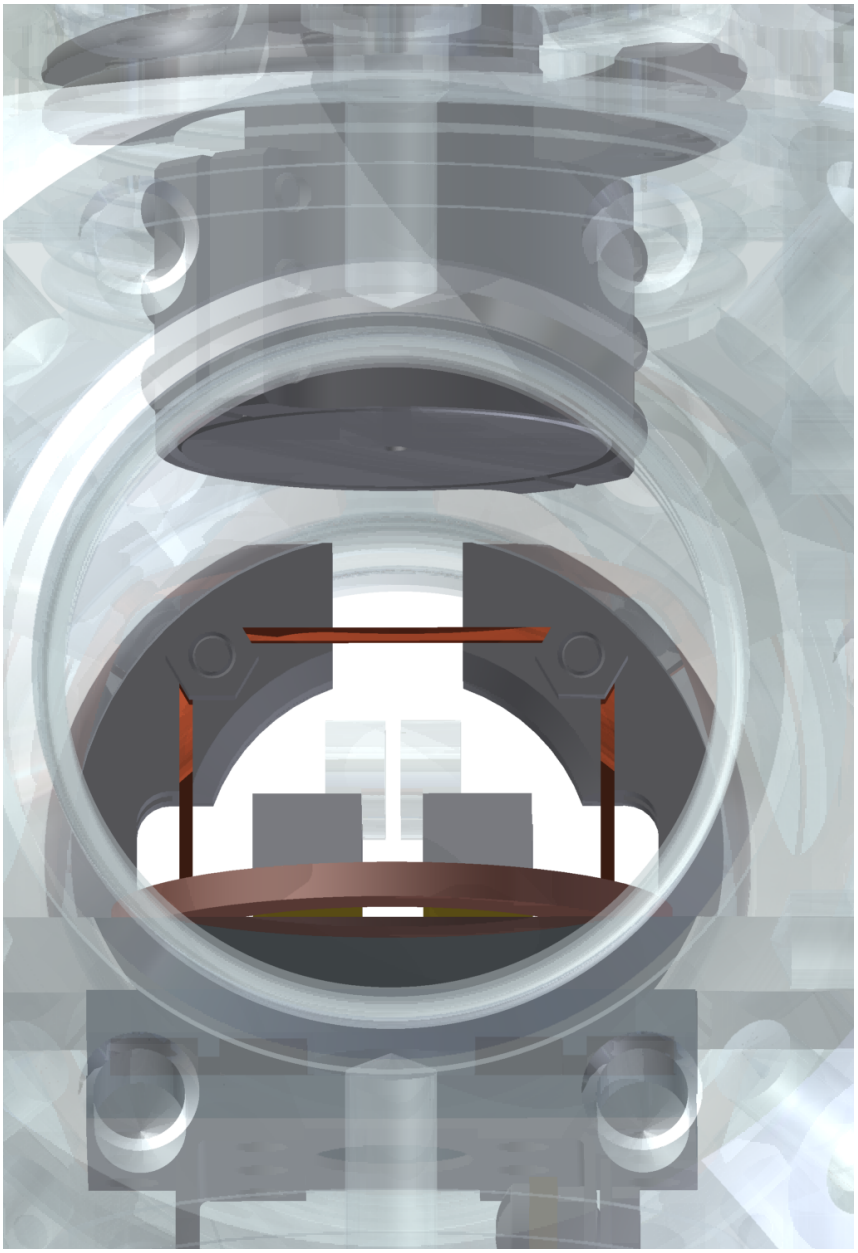

Figure 4.17: Translucent side view of the cavity chamber with MOT chamber attached. The cylindrical clamp holding the QWP and mirror with hole are visible

4.3.3 Magnetic environment

Figure 4.18 shows an approximate model of the magnetic field coils and some permanent magnets present near our vacuum chamber. The cyan rings represent the MOT coils described in detail in sec. 4.2.2. The blue and magenta rings are y-axis and x-axis coils respectively. They consist of 13 to 18 turns of 10-wire flat ribbon cable. The positioning is as close to the physics cavity chamber as possible. The red rings are the z-axis coils. They are made of roughly 19 turns of 6-wire flat ribbon cable. The z-axis coils location is also close to the chamber.

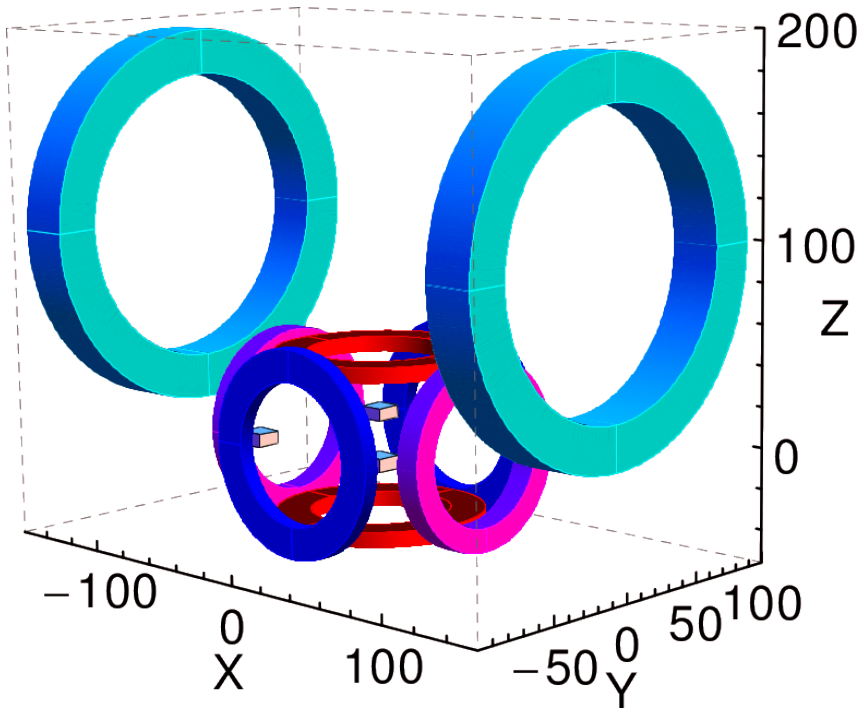

Figure 4.18: Magnetic field sources present in our experiment. The distances are in millimeters and they are accurate to within a few millimeters.

Not included in the model are the magnets attached to the ion pumps. The

small 3 L ion pump by Gamma vacuum comes with an effective shielding. The manufacturer has a magnetic field 3D map of the field near the pump [3]. Two inches away from the surface of the CF 1.33" flange attached to the pump (on axis of the CF 1.33" opening), which roughly corresponds to center of the MOT chamber, the only non-vanishing component of the magnetic field is along this axis at 1.615 Gauss. The field drops off to 0.503 Gauss three inches away (chamber edge along cube diagonal). It is clear this field has little impact on the cavity chamber, but causes a small shift in the MOT.

The strong field the MOT coils generate is of the order of 13 Gauss in the negative z direction near the cavity center (when a current of about 15 A runs through them). The z-axis cancellation coils can provide enough field to counter the strong residual field from the MOT, but this requires high currents of the order of 1 A. The power dissipation of such a large current by the coils in physical contact with our chamber causes very large temperature-induced drifts of the length of our physics cavity.

We solve the problem by placing four Neodymium block magnets (NdFeB, Grade N42), one at each corner of our cavity chamber and at the height of the cavity as shown in Fig. 4.18. These magnets have dimensions of: 1/2"×1/2"×1/4" and are magnetized across their thickness. The surface field is about 4400 Gauss according to the manufacturer. We place them such that the magnetization points in the $-z$ axis. This results in a strong combined field at the center along the z

[3]Magnetic plot for TiTan CV 3S pump with CF 1.33" port (04/25/2014) `http://www.gammavacuum.com/` (login required)

axis of about 7 Gauss. Adding the field from the MOT coils and from the magnets yields a total value of the field at about - 6 Gauss. Fig. 4.19 shows the variation of B_z as a function of z.

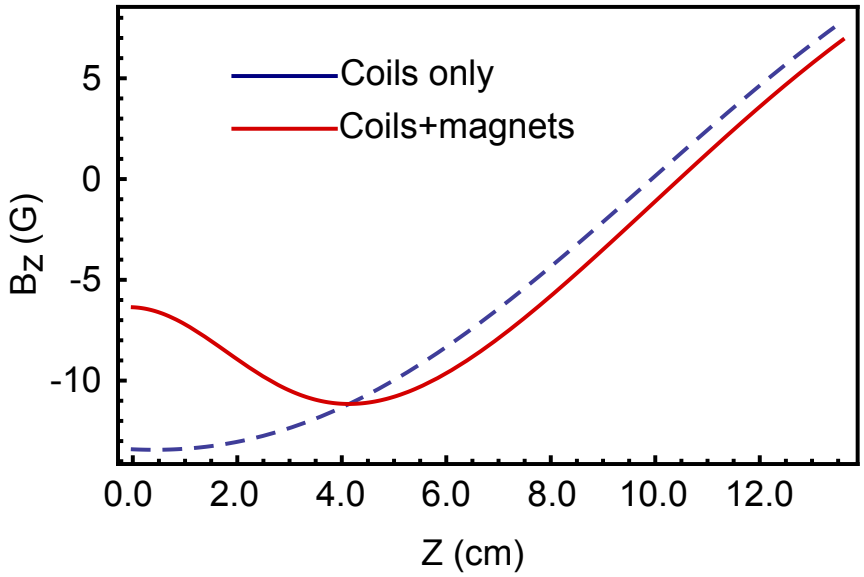

Figure 4.19: B_z as function of z in the cases of only the MOT coils on and the coils and the permanent magnets. A field of zero indicates proximity to the MOT. The position $z = 0$ corresponds to the location of the cavity.

Figures 4.17 and 4.16 both show the RF/microwave antennas we put inside our chamber. They are a few turns of copper wire, except for the z axis coil which we make with a 2.12" CF copper gasket. They are inside the chamber to minimize reflections from the surface of the vacuum chamber with well defined geometries to operate in the near filed regime.They may help understand possible unwanted reflections from the metal surfaces. We did not have any of these in the previous system and we should be able to drive microwaves and rf transitions with them,

using appropriate impedance matching.

Figure 4.15 shows the position of a magnetometer PCB (red square). It comes with a MAG3110 chip from Freescale, capable of measuring magnetic fields in three dimension in the range between ± 10 G, with a sensitivity down to 1 mG.

The position of the magnetometer chip with respect to the center of the cavity chamber is: $(x, y, z) = (0.138, 0.265, -1.256)$ in. The magnetometer has its own left-handed coordinate system as seen in Fig. 4.20.

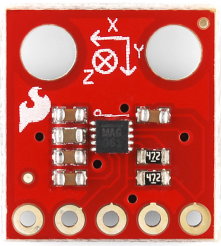

Figure 4.20: Sparkfun's MAG3110 breakout board

These directions map into our coordinate system as follows:

$$X_{lab} = -X_{mag}$$

$$Y_{lab} = Z_{mag}$$

$$Z_{lab} = -Y_{mag}$$

4.4 Laser systems

The experiment hinges on our capability of addressing narrow atomic transitions using lasers. Rubidium atoms have a large set of easily accessible transitions

at a wavelength of 780 nm. A plethora of laser devices, especially diode lasers, operate at this wavelength, making this type of atom very popular in atomic physics experiments.

The D_2 line in ^{85}Rb has many transitions, the excited state lifetime gives it a FWHM of $\gamma/2\pi = 6.06$ MHz. This calls for careful frequency tuning and control of our lasers to avoid straying from resonance. We used methods similar to the Pound-Drever-Hall (PDH) technique [56] to stabilize lasers and the length of our cavities.

It is customary to constrain the atomic population to a two-level system by clever use of other transitions. These secondary transitions often receive the names: repumping, depumping or optical pumping. In the D_2 line of Rb, we do not necessarily require another independent laser system to address these secondary transitions. Devices such as acousto-optic modulators (AOM's) and electro-optic modulators (EOM's) can provide frequency shifts in the order of tens of MHz up to several GHz, respectively from a carrier frequency or reference.

The rest of this section describes our laser systems and our frequency stabilization routines. We also elaborate on our primary and secondary atomic transitions.

4.4.1 Limitations

The increase in the size of our MOT requires a significant increase in laser power used for trapping ($\sim$500 mW). The previous setup produces light of the right frequency after passing twice through an AOM. This results in significant power loss

(40% to 50%) due to imperfections in the beam shape and AOM crystal. Saturation in the crystal can occur at powers near 1 W.

The direction in which we wish to steer the experiment might take advantage of the simpler energy level structure of ^{87}Rb. The D_2 line of this heavier isotope of Rubidium is accessible to 780 nm light. The internal hyperfine energy level structure differs from that of ^{85}Rb in the range between MHz for the excited state and GHz for the ground state.

Our cavities are also quite sensitive to temperature changes. Our main stabilization routine cannot handle slow drifts in the length of the cavity. The implementation of a slow drift digital control on the HV bias PZT mitigates the problem but a more robust solution will be necessary for multi-hour operation, right now the limit is closer to one hour.

We make use of AOM's to get around some of these issues and implement a robust solution for easily switching between isotopes and preserving power for our trap. We also replace problematic pieces of hardware that did not perform reliably and/or stable enough.

4.4.2 Dual isotope scheme

Our experiment employs four lasers. The primary laser is a Titanium-Sapphire laser, specifically an MBR-110 at 780 nm, manufactured by Coherent, Inc. A Verdi V-10 laser (Also from Coherent Inc.) pumps the Ti:Sapph at 532 nm with 10 W of power. We use the Ti:Sapph for a variety of tasks: cavity probe, MOT cooling

beams, optical pumping beam and also as the basis of our frequency stabilization schemes. Figures 4.21 and 4.22 show the appropriate transitions for ^{85}Rb and ^{87}Rb, respectively.

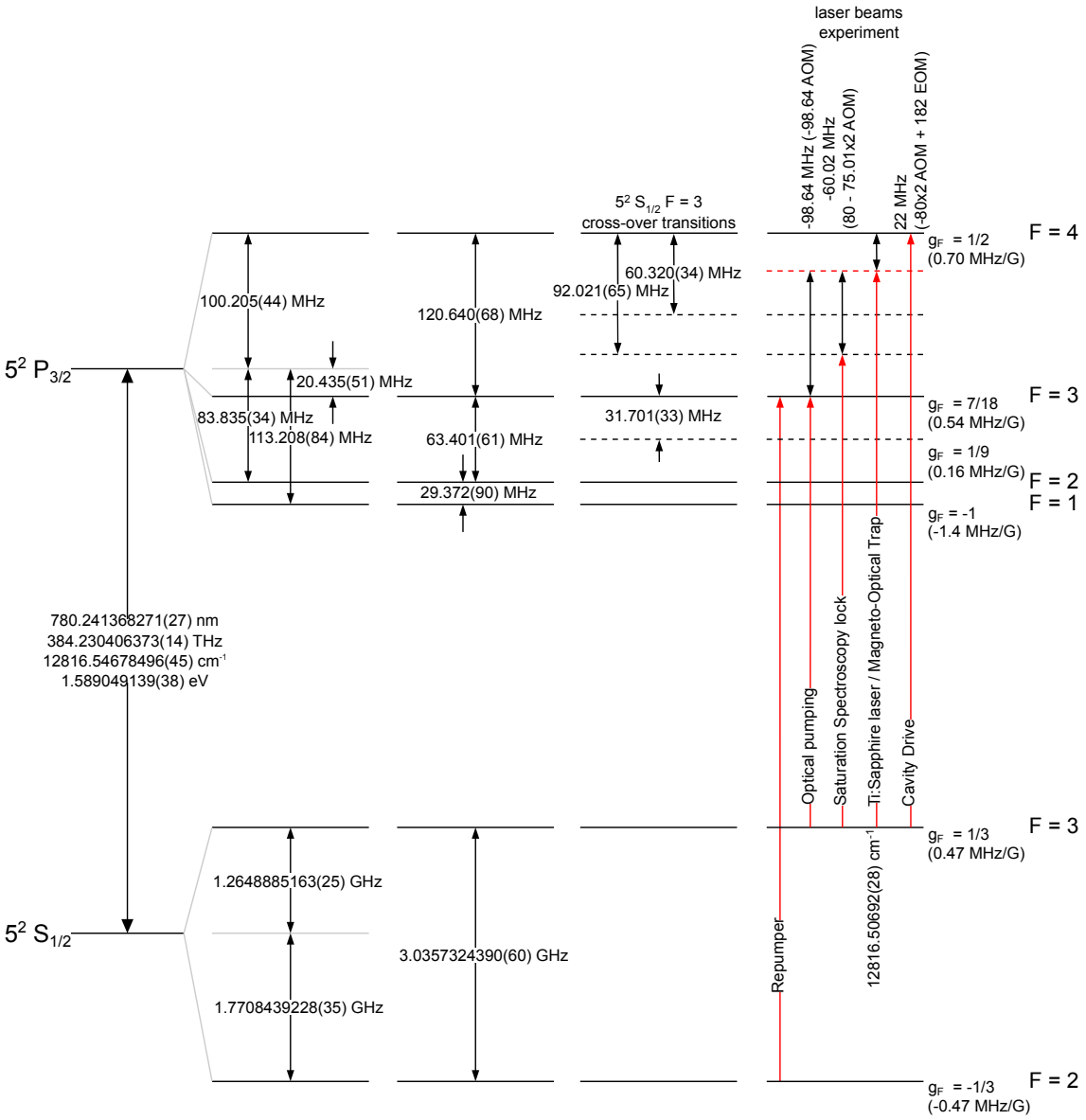

Figure 4.21: Current laser frequencies used for probing, optical pumping, frequency stabilization and cooling of ^{85}Rb atoms using the D_2 line

All these beams have slight differences in frequency, but all are within 270 MHz of the main transition. This proximity makes it possible to use a single laser to address all these beams with the help of acousto-optic modulators (AOM) and/or electro-optic modulators (EOM).

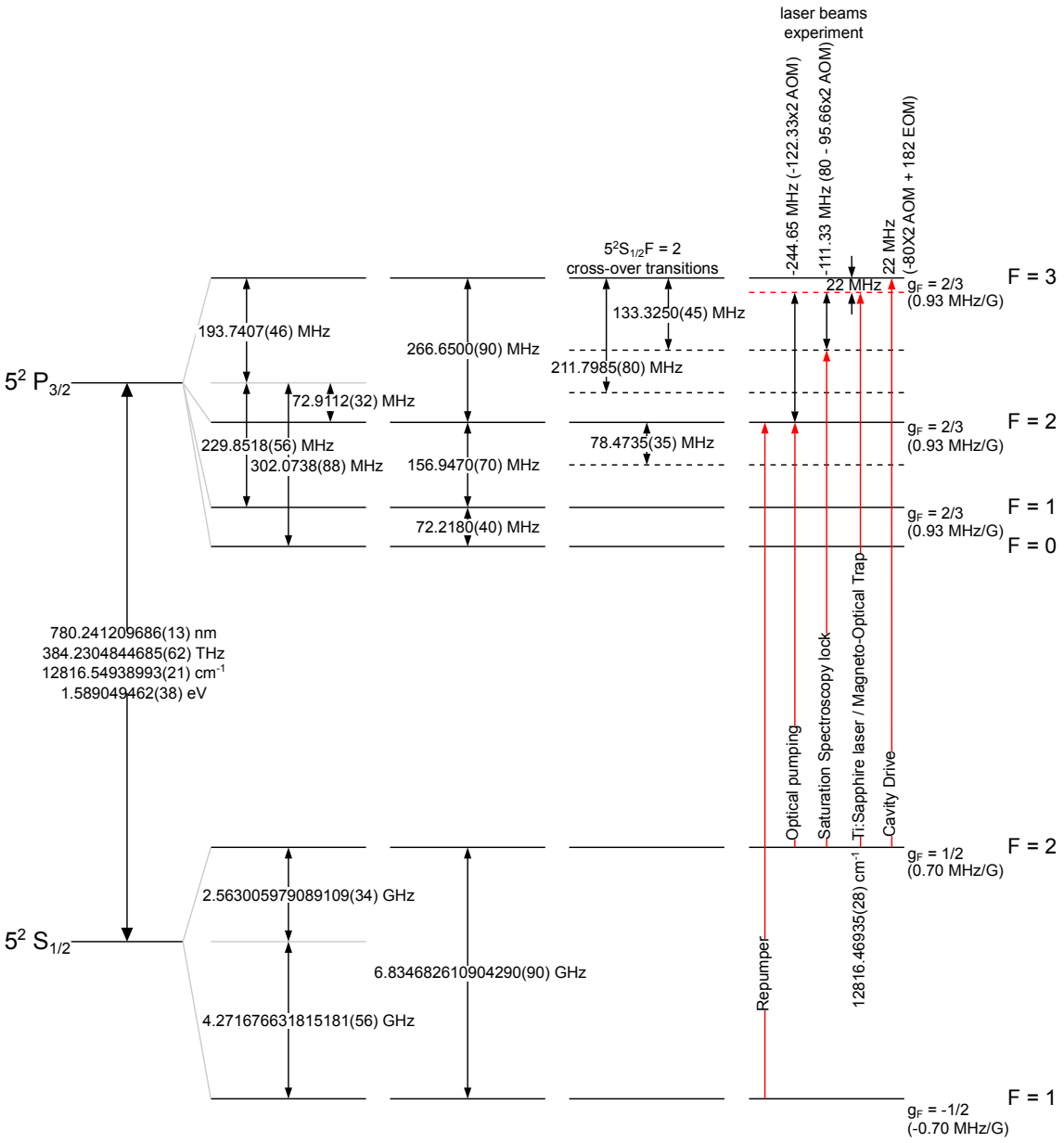

Figure 4.22: Current laser frequencies used for probing, optical pumping, frequency stabilization and cooling of ^{87}Rb atoms using the D_2 line

The 780 nm light coming out of our Ti:Sapph laser is red detuned -22 MHz from the main transition. This is the MOT cooling transition. This solves the problem

of losing power by going through an AOM, at the expense of losing tunability. Figure 4.23 illustrates in detail several beam paths. The optical pumping differs between the two isotopes. Each needs its own path for optical pumping requiring a single pass AOM shift at -98 MHz for ^{85}Rb or a double-pass AOM shift at -122.3 MHz for ^{87}Rb. The most important beam is the cavity drive. We get to near resonance by using a combination of a double pass AOM at 80 MHz and then taking the red side-band of the beam from an EOM (-182 MHz shift). The cavity drive does not change between the two isotopes. The reason is because it is referenced to the Ti:Sapph laser which does change. It would be easier for us to simply use the EOM, because shifting frequencies does not lead to misalignment, but the AOM offers the possibility of variably attenuating the drive beam. The EOM model AZ-0K5-10-PFA-PFA-780, made by EOSpace, provides a fast way of changing the frequency. The reference we use for stabilizing the frequency (frequency lock) is a so-called cross-over transition on the saturated spectrum. The frequency reference for stabilizing the Ti:Sapph laser changes for each isotope, but we can use two AOM's to address both energy levels without realigning. The first AOM provides a 80 MHz shift and the second one operating in double-pass configuration can change between -75 MHz for ^{85}Rb and -95 MHz for ^{87}Rb.

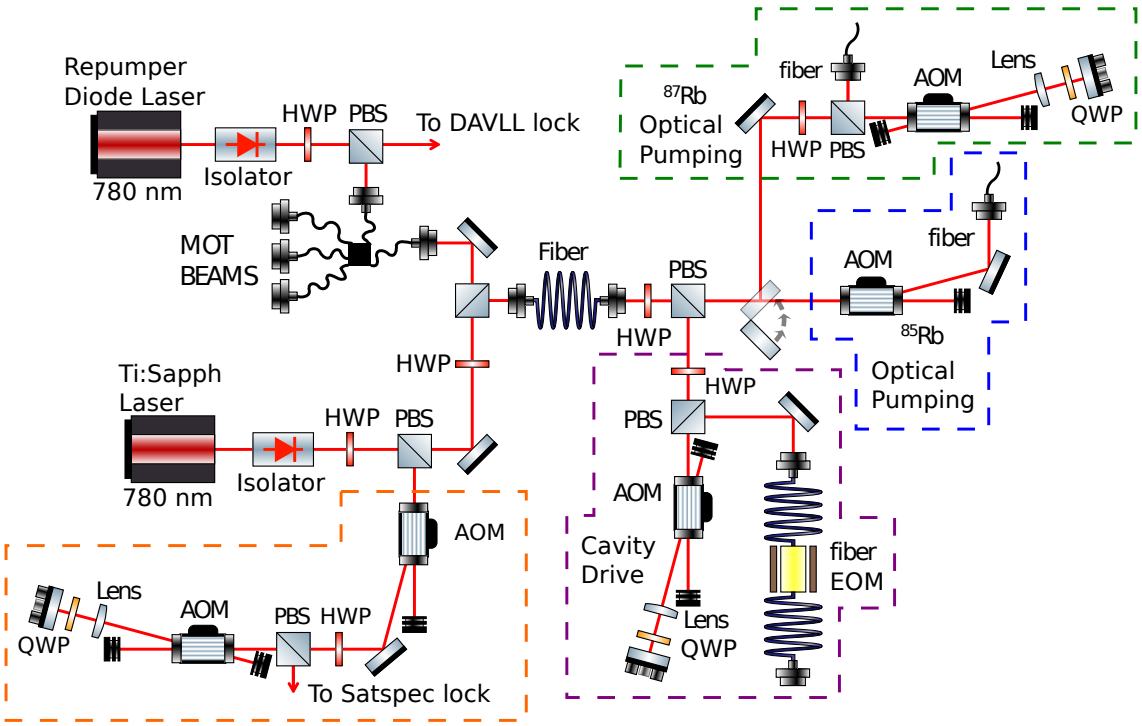

Figure 4.23: Various laser beam paths with the optical systems for frequency shifting. Green dashed section is the optical pumping for ^{87}Rb, blue is optical pumping ^{85}Rb, purple is cavity drive and orange is the lock cross-over transition.

The frequency stabilization for the Ti:Sapph relies on an internal fast cavity-based lock. This can narrow the linewidth of the laser to about 100 kHz. Long-term frequency drifts force us to implement an absolute frequency reference using saturated-absorption spectroscopy in a magnetically-shielded rubidium vapor cell as shown in Fig. 4.24. We derive an error signal from the main transition hyper-fine crossover transition. The steps to generate the signal are similar to those of the Pound-Drever-Hall (PDH) method with a few differences. We use a free-space

EOM to put a frequency modulation on a probe beam at 20 MHz, while keeping a more powerful (about 10x) pump beam without modulation (We send part of the modulated beam to a transfer cavity). Both beams pass through the vapor cell in opposite directions ($\vec{k}_{\text{pump}} = -\vec{k}_{\text{probe}}$), taking great care that they overlap very well. This technique has a two-fold effect: minimizes Doppler broadening and causes saturation in the atoms which leads to reduced absorption by the probe beam, revealing the narrow cross-over resonances. We collect the light of the probe beam with a fast photodiode. We use a BIAS-T circuit to split the RF part of the signal from the DC part. We amplify the RF part prior to mixing it with a local oscillator. The result of the mixing is the error signal which we feed into a SIM960 PID controller. The output of this device, *i.e.* the correction, is routed to the MBR-110E or the MBR controller box. The DC part contains information regarding the saturated-absorption spectrum. This stabilization process forms our *master* lock. Its robustness means we reference almost all other locks to it.

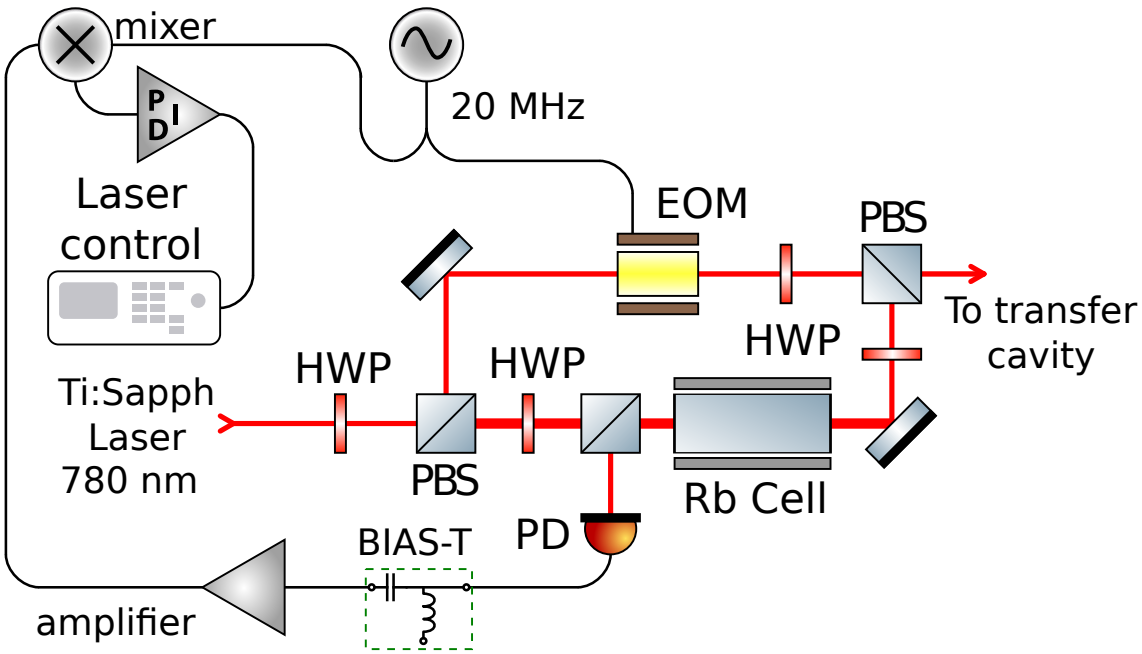

Figure 4.24: Saturated spectroscopy laser frequency stabilization diagram.

A rubidium MOT requires the use of light at another frequency to bring back into the cycling transition atoms that fall into the lower hyper fine state. This is often dubbed "repumper" transition (See Fig. 4.21 and 4.21). It is difficult to use the MBR-110 laser for this purpose. The frequency gap with respect to other transitions is between 3 and 6.8 GHz, out of range of AOM's. Some groups have developed ways of obtaining this frequency using a fiber EOM [57], but the power damage threshold of our available fiber EOM is quite low (circa 10 mW) and they must use a device like a tapered optical amplifier to boost the power after imprinting the appropriate side-bands. We simply use another laser system for this purpose. The previous experiments employed injection locking of Vortex diode laser seeding a

Sharp laser diode. We substitute our repumper laser system for a Toptica DLX-110 diode laser. This change simplifies the system as well as providing enough power to supply our large MOT.

This repumper laser needs to have a stable frequency as well. We use a well-known technique: Dichroic Absorption Vapor Laser Lock (DAVLL) [58] to obtain an error signal that another SIM960 PID Controller can handle and feed back the correction to the diode laser. Figure 4.25 shows our experimental setup.

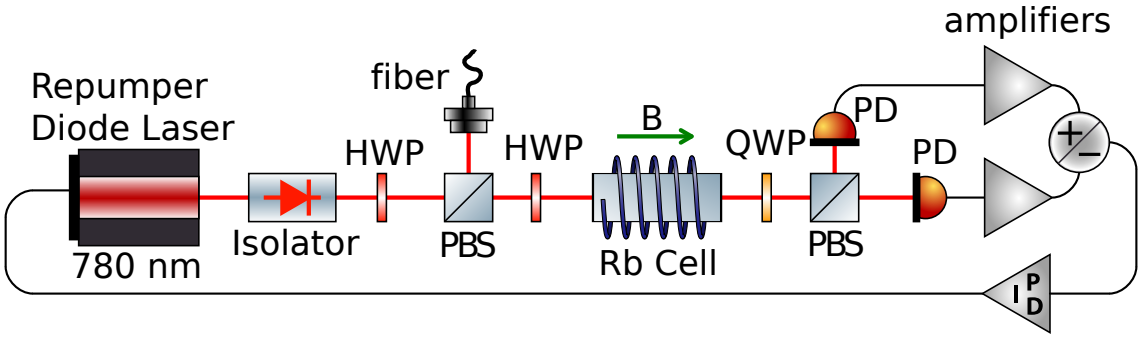

Figure 4.25: Dichroic Atomic Vapor Laser Lock (DAVLL).

We use a Toptica DL-100 diode laser at 820 nm for stabilizing the length of our physics cavity. The interaction of light at this wavelength with the atomic beam is negligible but still provides a strong reflection from the cavity mirrors. We stabilize this laser to the Ti:Sapph frequency with the use of a transfer cavity, prior to stabilizing the physics cavity as shown in Fig. 4.26. We monitor the transmissions of the two wavelengths through both cavities. One of the PZT's of each of the cavities is connected to a HV power supply that serves as a bias and the other PZT's are connected to a HV ramp with an amplitude of about 1 kV. The process starts with

us changing the current to the 820 nm laser diode until both the 780 nm and 820 nm lasers are resonant with the TEM_{00} mode of the physics cavity. Normally it is also necessary to change the length of the cavity by adjusting the HV bias to one of the PZT's and/or the offset of the HV ramp on the other. We then must find a resonance overlap in the transmission of the transfer cavity as well. We do this only by adjusting its length. The Ti:Sapph modulated light at 12.4 MHz is used to stabilize the transfer cavity length using the PDH technique, a SIM960 PID controller and feeding back into the PZT initially connected to a HV ramp. Finally, we stabilize the 820 nm diode laser frequency using the transfer cavity resonance and the PDH method in a similar manner, but this time we use a 9.04 MHz modulation applied directly on the laser diode current.

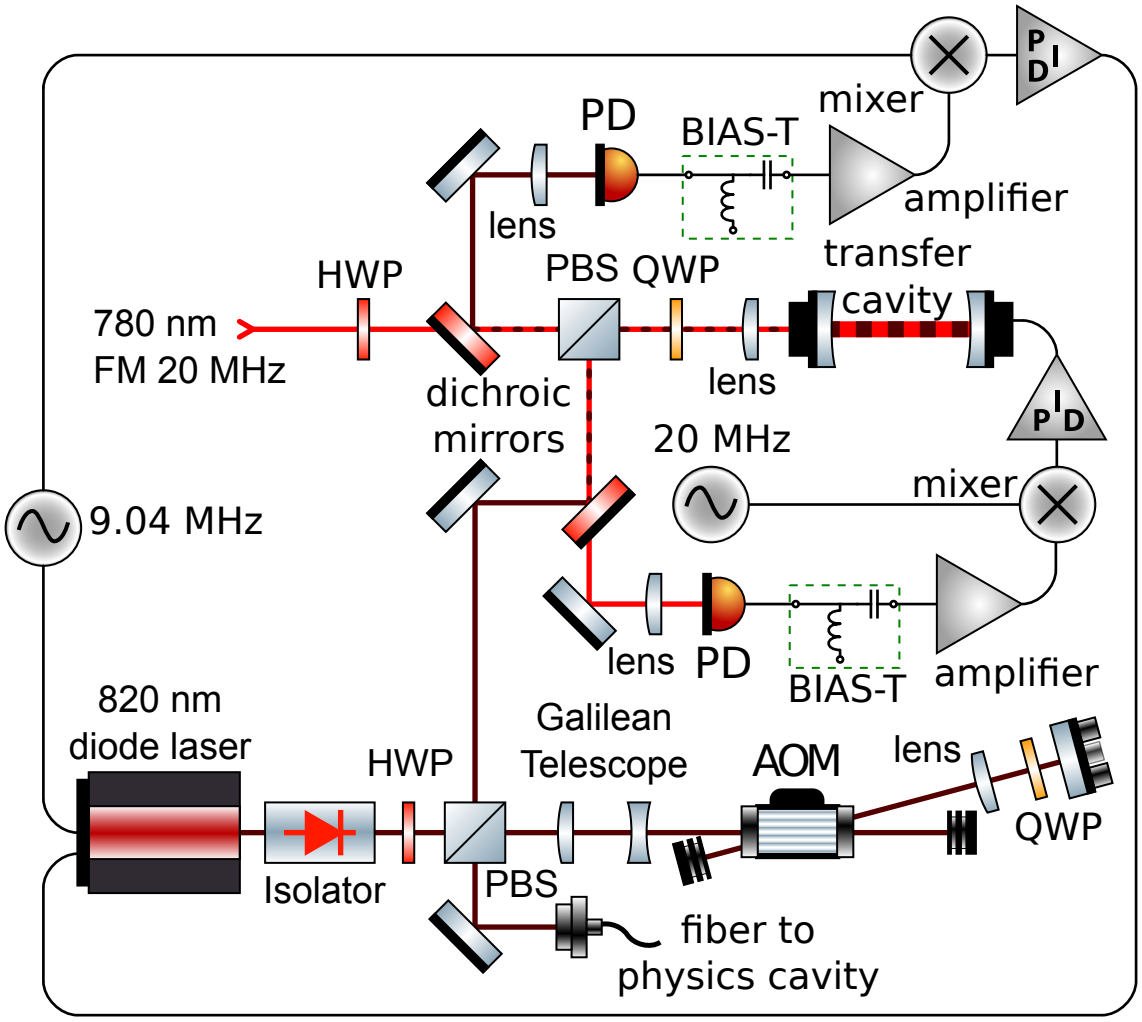

Figure 4.26: Transfer cavity and 820 nm laser experimental diagram. It also shows the AOM we use for scanning the length of the physics cavity.

The final step is to stabilize the length of the physics cavity (See Fig. 4.27). The stable reference is now the 820 nm laser. We use its modulation at 9.04 MHz to produce a PDH signal and feed back into the ramp PZT. Our checks for an effective atomic beam include varying the frequency of the driving laser (780 nm) by shifting the frequency of the RF signal to the EOM. At the same time we need

to keep it in resonance with the physics cavity. We achieve this by shifting the frequency of the 820 nm laser in unison with the drive. The scan for 820 nm takes place before reaching the physics cavity, on a different path as the beam going into the transfer cavity (See Fig. 4.26). The light double-passes through an AOM and then couples into a single mode polarization maintaining fiber. This setup uses a Galilean telescope for compactness and achieves an efficiency circa 80% [59]. It allows a comfortable scan range of ±20 MHz. It is important to monitor the power at the fiber output and keep it constant throughout the scanning process. Our power stabilization scheme is a simple digital PID algorithm that relies on the AM input of the RF driver of the AOM to make appropriate corrections.

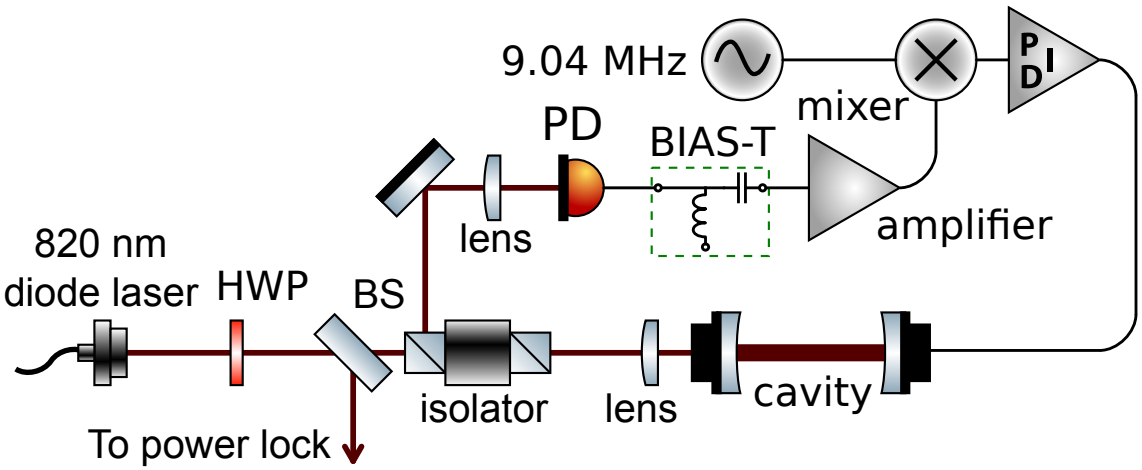

Figure 4.27: Physics cavity PDH technique experimental setup.

The stabilization of the length of both cavities with the PDH method using a PID controller is ineffective at dealing with long term drifts caused by temperature changes throughout the day. A simple control algorithm reads out the correction

drift from our PID controller and imparts a small change in the voltage of the other PZT. This can correct the effects of the drift.

Temperature stabilization of a copper enclosure around the transfer cavity helps distribute heat evenly. We maintain the surface of the copper at about 40^o C, well above room temperature. A plastic box also aids in insulating the environment. This passive control grants us great control of the cavity length. The long term drift is minimal to the point where the slow drift control for the transfer cavity is almost unnecessary.

We also use a helium-neon (HeNe) laser primarily for cavity construction and alignment (See sections 4.1 and 4.3).

4.5 Detection system

Figure 4.28 illustrates a simplified version of the detection apparatus. The output of the cavity gets collimated by a converging lens and goes through a zero-order half-wave plate (HWP). We rotate the HWP to align the polarization with a Wollaston prism (PBS). The vertically polarized light takes a different path than the horizontally polarized light.

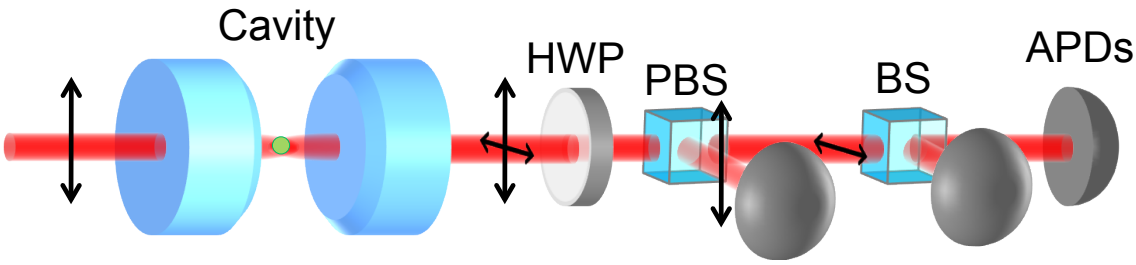

Figure 4.28: Simplified detection apparatus. The HWP plate aligns the polarization to a Wollaston prism (PBS) which separates vertically y horizontally polarized light into separate paths.

The vertically polarized beam carries 780 nm (drive) and 820 nm (cavity lock) light. We monitor the intensity of the transmitted light at 820 nm by splitting a fraction of the vertically polarized beam and sending it to photomultiplier tube (PMT). We use a combination of filters: 780 nm band filter + AR coated RG-9 + Semrock 780 nm MaxLine interference filter, to remove the remaining 820 nm light.

During the warm-up and stabilization sequence initiation we do not use the APD's. We use another PMT to monitor the transmitted intensity of the 780 nm light (vertical polarization). We can toggle between using an APD and a PMT for the vertical polarized path using a remotely controlled motorized flip mirror.

The three APD's are Perkin Elmer SPCM-AQR-12, 13 and another 12. We label APD V the detector in the vertically polarized path, while APD A and B are the labels we use for the horizontally polarized path. The current detection efficiency for all APD's is about 30 % which includes path and quantum efficiency.

The emission of a TTL pulse follows the detection of a photon by an APD. APD V output goes directly to our computer. The output of the rest passes through a pulse splitter. This device creates two similar pulses with smaller amplitude. One travels to a photon counter SR400 for measuring average count rates. The other copy goes to our computer. The computer carries a time-stamp correlator card DPC-230 from Becker and Hickl. It can record up to eight channels of TTL events with a 165 ps resolution.

Our data analysis tool of choice is the intensity correlation function. We can calculate it from a record of photon arrival times (provided by the DPC-230). The size of our datasets prompts us to use C++ code for computing the $g^{(2)}(\tau)$ in the interest of speed and adaptability.

Chapter 5: Environment assisted speedup in an optical cavity

Manipulation of the rate of evolution of a quantum systems by careful tailoring of the environment is desirable in a large number of areas of physics like quantum information [60], and, optimal quantum control and feedback [61]. This chapter contains recent "first light" preliminary results from our new apparatus. We show that increasing the interactions of an optical cavity field with the environment (Number of two-level atoms) can enhance or *speed-up* the rate of re-population of the state of the cavity.

5.1 Introduction

The quantum speed limit is the maximum speed of evolution of a quantum system between two distinguishable states. This concept dates back to the original work of Heisenberg in his time-energy uncertainty relation. Lower bounds on the quantum speed limit time exist for closed or unitary (uncontrolled) quantum systems [62, 63], but only recently there has been theoretical progress [64–66] for more general open quantum systems that can be controlled externally. These developments could prove very useful in quantum information, where efficient processing entails performing gate operations in a time-frame much shorter than the coherence

time. Quantum speed limit bounds provide guidelines for optimal quantum control and feedback protocols.

Recent work at the JQI by the groups of Gorshkov and Monroe [67] shows the maximum speed at which information can propagate in a quantum many-body system. Another study [64] points to the possibility of observing *speed-ups* in the quantum speed limit if a system is subject to environment changes (changing coupling between cavity field and environment - atom). Cavity QED systems in the intermediate and strong coupling regime can exhibit environment-assisted evolution [68], such as non-exponential decay and/or Rabi oscillations in the amplitude associated with one photon in the cavity mode.

Our optical cavity lies in the intermediate coupling regime, with our cavity-atom parameters of the same order: $(g, \kappa, \gamma)/2\pi = (3.2, 4.5, 6.0)$ MHz. We have at our disposal a way to enhance our coupling to the field in the cavity by tailoring the *environment*, different from the traditional way in cavity QED. Our system is the field and the controllable environment is a collection of N two-level atoms under very weak excitation. Our slow atomic beam can provide a large variety of effective number of atoms in the cavity ($N_{\text{eff}} = 0.1 \rightarrow 30$). This makes our "effective" dipole coupling constant scale as the vacuum Rabi splitting, $g\sqrt{N}$. The more atoms, the more channels the cavity field can couple to.

Conditional measurements of the photons leaving the cavity ($g^{(2)}(\tau)$) represent an ideal way of looking at environment effects we hope to unravel. Equation 1.14 offers a clean analytic expression for $g^{(2)}(\tau)$ under weak driving. We are going to be looking at the evolution of a system (quantized cavity mode) as we change the

environment (atomic polarization in the same mode). Eq. 1.16 shows that as N grows, $g^{(2)}(\tau)$ can execute vacuum Rabi oscillations.

This study represents a natural first step towards understanding how we can measure quantum speed limited dynamics in our cavity QED system. We wish to apply these concepts in pursuing optimal quantum control protocols [69] beyond what we show in Chap. 3 for a spontaneously-created coherence.

5.2 Experimental setup

The apparatus description in Chap. 4 is exhaustive. There are some notable differences with the experiment described in this chapter. Figure 5.1 shows the general layout of the physical system. An atomic beam of ^{85}Rb atoms co-propagates along the push/top MOT laser beam and couples to the TEM_{00} mode of our 1 mm optical cavity. The magnetic field points along the $-z$ axis and defines our quantization axis. The MOT coils and an arrangement of four Neodymium permanent magnets generate this field. We estimate a field about $\vec{B} = -7.2$ G $\hat{z}$. The push

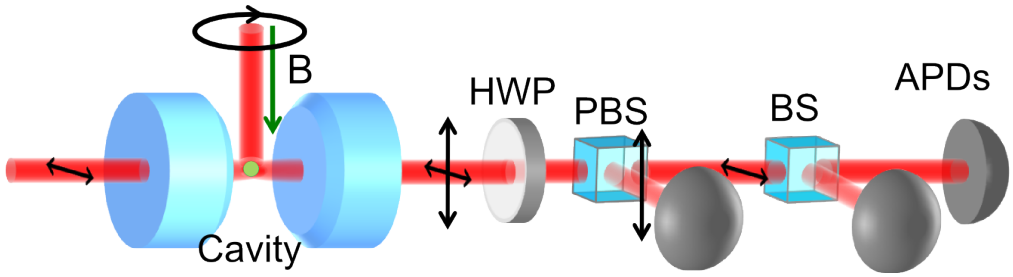

Figure 5.1: Simplified apparatus for measuring driven mode autocorrelations

or top laser beam of the MOT has typical saturation parameter close to 1 and a

detuning from resonance of 22 MHz. It can propagate through the hole in the QWP and mirror assembly and scatter on the cavity mirrors. This is the primary source of background in our photon counting experiment. It can also work to our advantage: The polarization of the push beam is σ^+ and can provide some optical pumping to the $|F = 3, m_F = +3\rangle$ state, despite the Doppler shift of the traveling atomic beam and the large detuning ($\sim$22 MHz). We measure which Zeeman state has the largest absorption for a given polarization and perform the measurements on that. This is not a perfect two-level atom and further work will be needed to clean up the optical pumping and state selection.

The measurements we wish to perform require us to drive weakly, at most with: $n/n_{\rm sat} \sim 0.10$ and also increase the effective number of atoms in the cavity as much as possible. As $N_{\rm eff}$ grows, the resonant absorption count rate on the APD's drops. The large background that comes from the MOT push beam (and the fluorescence of the trap itself) limits our SNR. This trade-off between optical pumping and background forces us to block the MOT push beam using a crude square piece of paper of roughly 4 mm $\times$ 4 mm.

We drive the system with H-polarized light, which in the frame of the atoms appears as a complicated combination of circularly polarized light.

Addressing the atoms in the state where they have been optically pumped to requires us to easily shift the frequency of our driving laser. We accomplish this by changing the RF frequency driving our EOSpace fiber EOM. At 182 MHz, the drive is resonant with the transition $|F = 3, m_F = 0\rangle \rightarrow |F' = 4, m_{F'} = 0\rangle$. A magnetic field of -7 G induces a Zeeman shift of about -10 MHz in the $|F = 3, m_F = +3\rangle \rightarrow$

$|F' = 4, m_{F'} = +4\rangle$ transition. We observe this shift by performing frequency sweeps of the drive laser and the cavity length. We operate our drive at a detuning of -10 MHz (172 MHz RF to EOM).

Our system operates has $n_{\text{sat}} = 1.2$ and $C_1 = 0.37$.

The parameter we use to increase the number of atoms is the current of our Rb dispenser. The size of our MOT increases significantly for as we vary the current from 3.1 A to 4.0 A.

5.3 Connection between theory and experiment

We are looking for a speed-up in the re-population of the state $|1, 0\rangle$ after it has emitted a photon (Eq. 1.5). In other words, we are interested in changing the evolution of $|A_1(t)|^2$. The model of Sec. 1.2 provides a guide, but we are now tracing over the atomic polarization constituting the environment. Such environments can show non-Markovian behavior [70].

Figure 5.2 shows the subsequent evolution of $|A_1(t)|^2$ after the cavity photon leaves but there can be an excitation in the atomic polarization, captured by the $g^{(2)}(\tau)$. Equation 1.14 provides the model based for the second-order auto-correlation function we ought to expect from a collection of two-level atoms in a single-mode optical cavity. It is a intimately related to $A_1(t)$ (See Eq. 1.13)

It clearly shows a significant increase in the rate of "re-filling" one photon in the cavity. We can extract this rate from the slope of the graphs. The slope of the anti-bunching gives us the speed with which the amplitude evolves and returns to

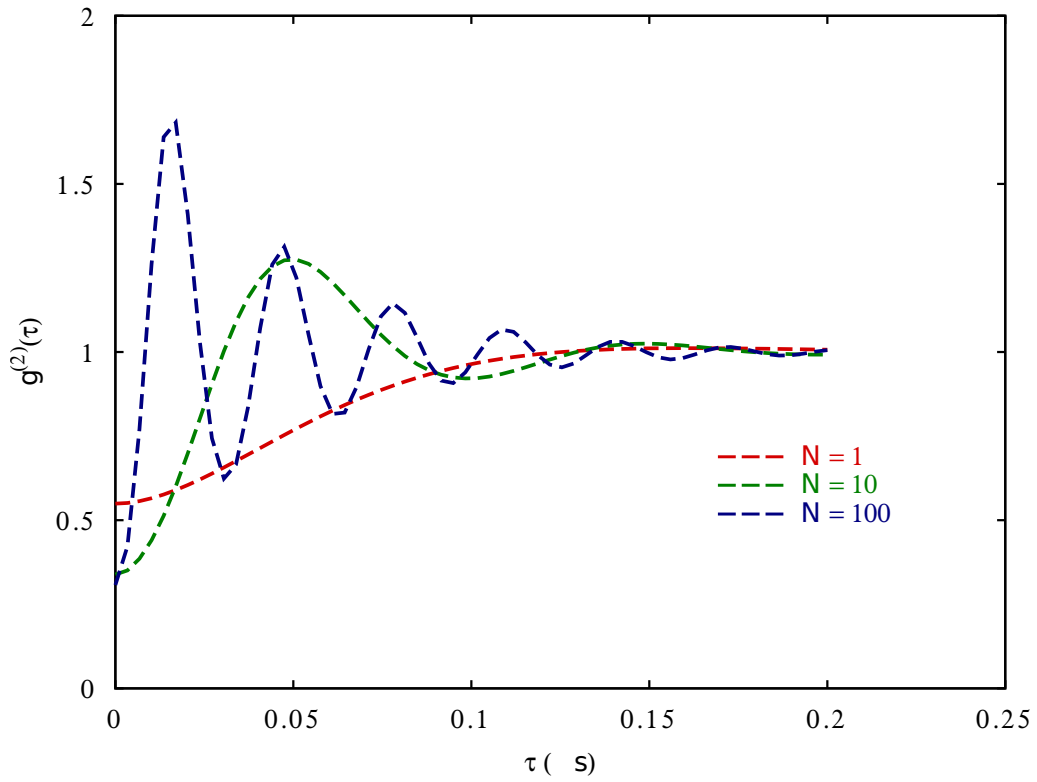

Figure 5.2: Simple model for $g^{(2)}(\tau)$ for the field evolution as function of time for different values of N. Obtained from Eq. 1.14 for $(g, \kappa, \gamma)/2\pi = (3.2, 4.5, 6.0)$ MHz and the values of N shown in the legend

steady state. We can extract the maximum slope easily from the analytic expression for $g^{(2)}(\tau)$ traces and plot them as a function of $g\sqrt{N}$, our effective coupling strength as in Fig. 5.3.

The model of Eq. 1.14 assumes static, maximally coupled atoms to the cavity field. A refined model, where we simulate the atomic beam number fluctuations with a poissonian weight and randomly generate the positions of the atoms in the cavity mode (which is radially Gaussian with a longitudinal standing wave) [71,72], leads to variable dipole coupling strengths as shown in Fig. 5.4. In other words, $g \to g(r, z)$

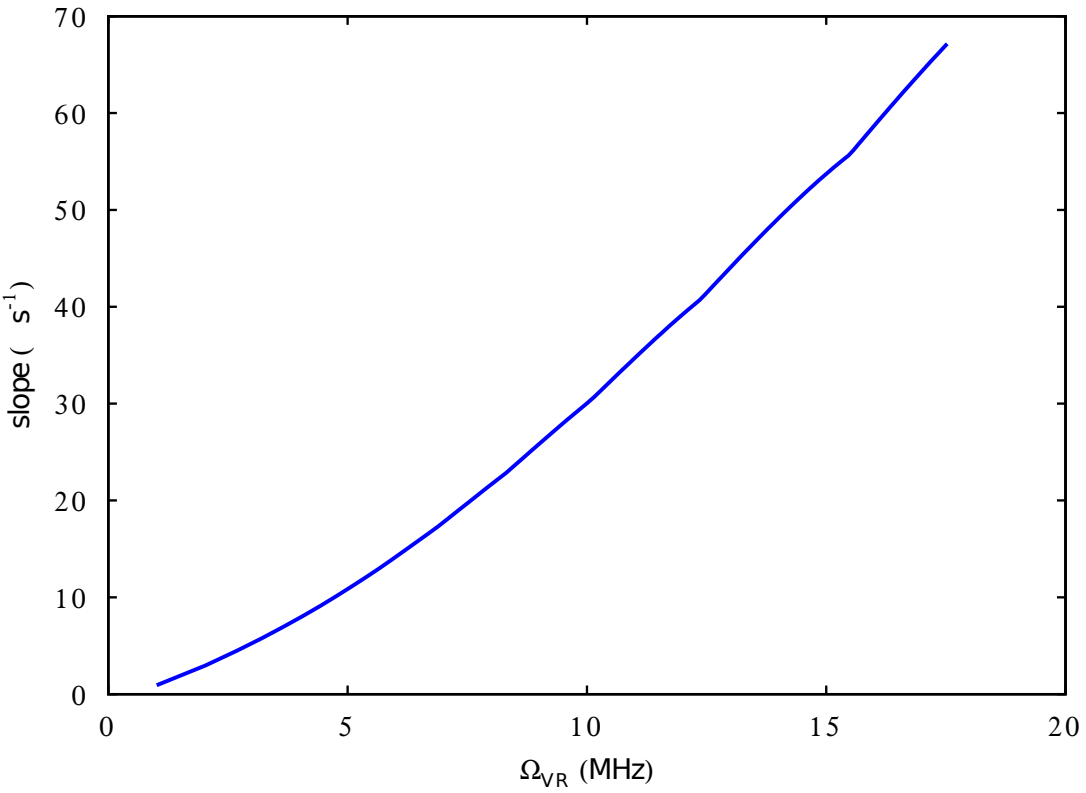

Figure 5.3: Simple model rate of refilling as function of $\Omega_{\mathrm{VR}} = g\sqrt{N}/2\pi$.

where r is the radial position of the atom in the mode and z its longitudinal position along the standing wave. Note that there is no dependence on the velocity of the atoms, a further necessary refinement.

We can extract the maximum slope for the simulated $g^{(2)}(\tau)$ traces in a similar way as with the simple theory and plot them as a function of $g\sqrt{N}$ as Fig. 5.5 shows.

5.4 Results

We show first we can alter the environment to which the cavity field couples by demonstrating we can obtain large vacuum Rabi splittings with our new system,

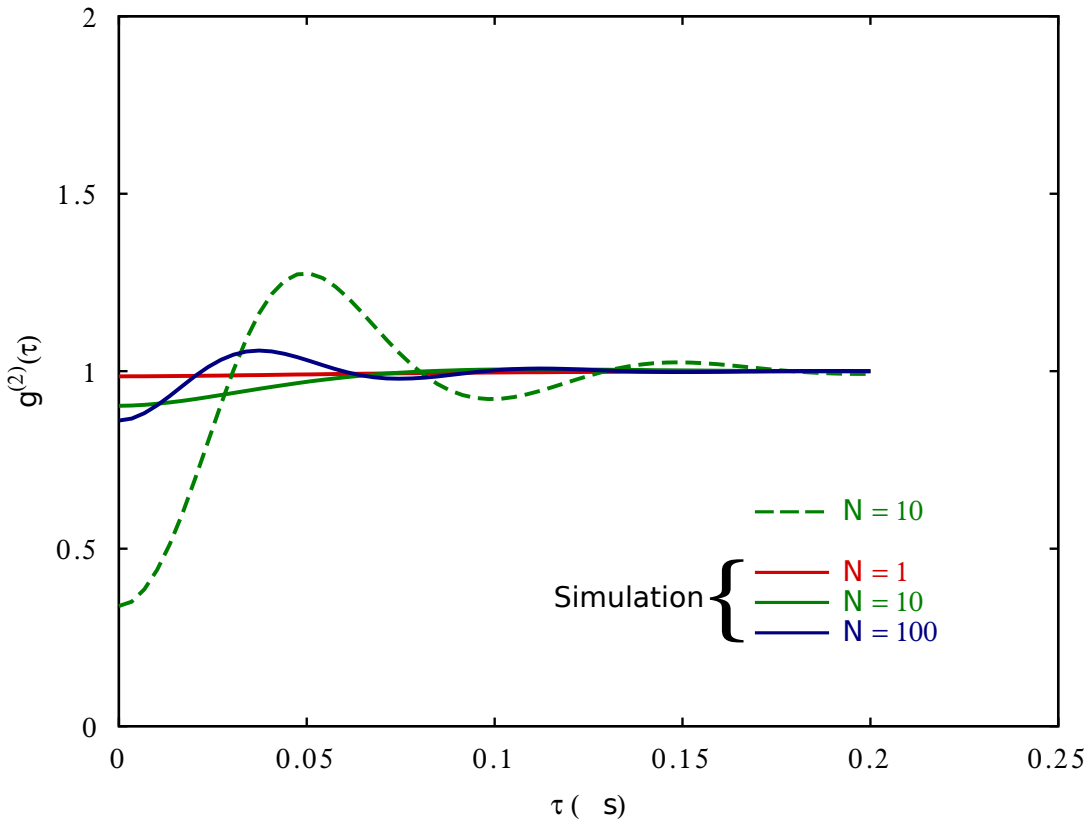

Figure 5.4: $g^{(2)}(\tau)$ for different values of N. Note the clear anti-bunching. Calculated using Eq. 1.14 with a poissonian weight for atomic beam fluctuations and an effective g by randomly generating the position of the atoms in the cavity mode.

leading to potentially a large N_{eff}.

5.4.1 Vacuum Rabi splitting

Our new cavity and atomic beam offer larger g and a larger sampling of N_{eff}. The vacuum Rabi splitting is a signature of good atom-field coupling and can give good predictions for the cooperativity C or the effective number of atoms passing through the cavity N_{eff}. Figure 5.6 shows a sample vacuum Rabi splitting spectra we get when we sweep the frequency around our atomic resonance with our drive

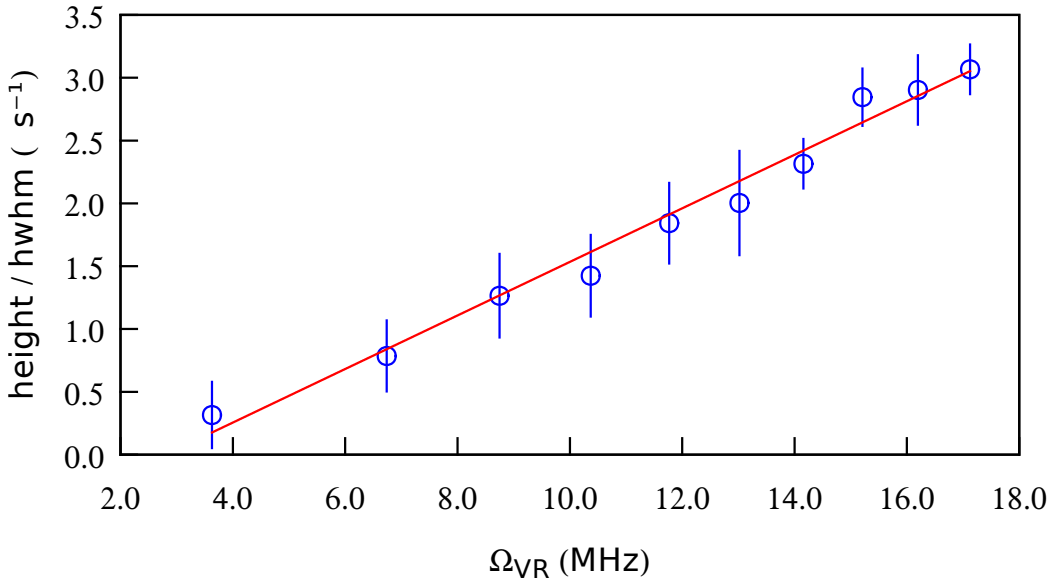

Figure 5.5: Simulation rate of refilling as function of $\Omega_{\mathrm{VR}} = g\sqrt{N}/2\pi$. Linear fit exhibits a slope of 0.21 ± 0.01 μs^{-1}/MHz, an intercept of -0.6 ± 0.1 μs^{-1} with a reduced $\chi^2 = 0.25$

laser $\pm$ 20 MHz at a rate of 2.5 MHz/s. These enhancements in coupling prove invaluable for carrying out our measurements. Our previous cavity system was unable to produce such large Vacuum Rabi splittings.

5.4.2 Preliminary measurement of speedup as function of Ω_{VR}

Figure 5.7 shows a raw dataset. The highlights of this $g^{(2)}(\tau)$ are the classical correlation bump between -10 to 10 μs, showing the transit time of the atoms and the evidence of anti-bunching. This is in contrast to previous results [6, 13], where the transit time was about 5 μs. It gives us the average speed of the atoms in the beam $\sim$ 5 m/s. The zoom of Fig. 5.7 shows a hint of anti-bunching near $\tau = 0$.

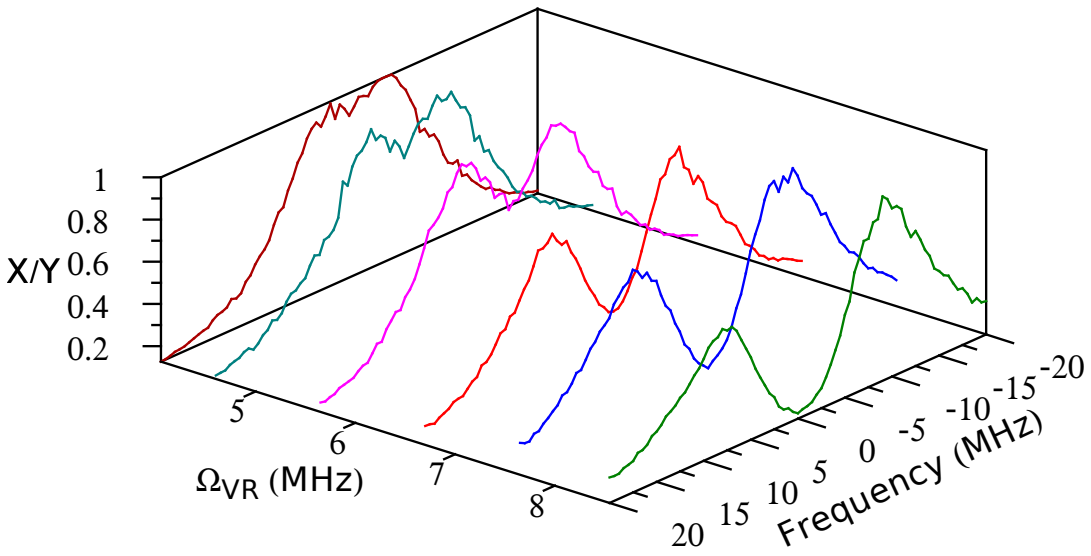

Figure 5.6: Vacuum Rabi splitting for different number of atoms.

Figure 5.8 is a sample of our analyzed experimental traces. We proceed to extract a slope or rate of change from the anti-bunching valley to the region where $g^{(2)}(\tau) > g^{(2)}(0)$. We do not attempt to fit to the exact analytic form from Eq. 1.14 but instead just fit to an inverted Lorezian around unity. This imprecise modeling will show in large reduced χ^2, but gives a quantitative measurement of the slope by taking the ratio of the amplitude and the HWHM.

A current of 4.0 A in our Rb dispenser was used for Fig. 5.8. The rate of detection on our APD's is about 800 kCs^{-1} (with absorption from atoms) and a background count rate of 10 kCs^{-1}. The photon number in the cavity is about $n = 0.10 \pm 0.02$ once we account for our detection efficiency. We estimate the number of atoms to be about $N_{\text{eff}} = 7.1 \pm 0.2$.

Figure 5.9 shows a distinct linear growth of the rate of refilling (antibunching slope) as a function of Ω_{VR}. We expect a rough linear dependence of the slope on

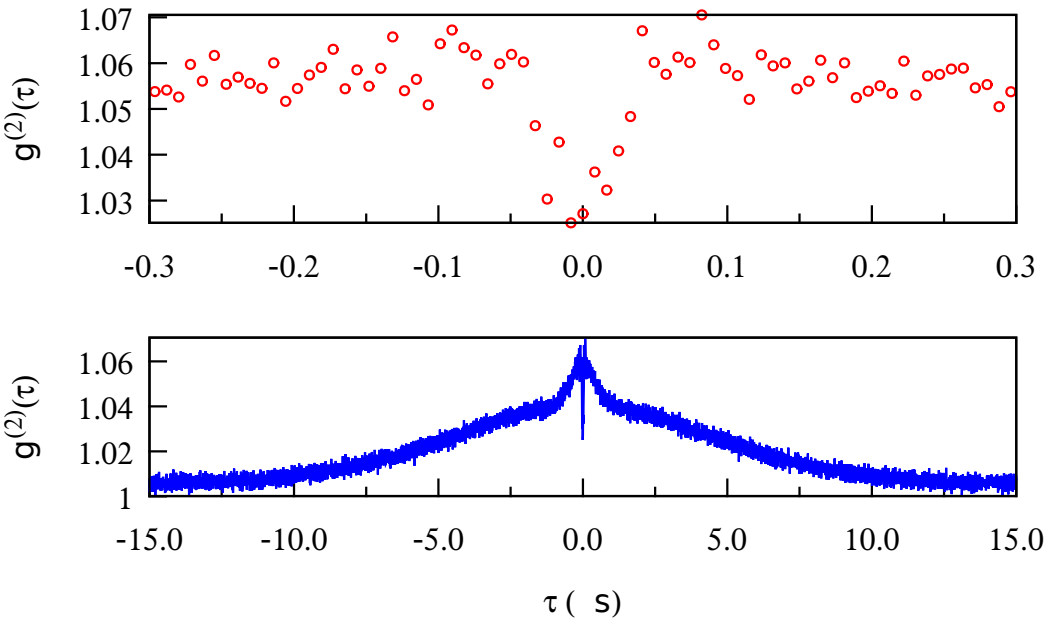

Figure 5.7: Raw $g^{(2)}(\tau)$ of driven mode of cavity showing antibunching for $g\sqrt{N}/2\pi = 8.6 \pm 0.1$ MHz. Bottom part shows the full $g^{(2)}(\tau)$ highlighting the classical correlation bump characteristic of our atomic beam transit time. Top part focuses on the area around the anti-bunching.

$\Omega_{\mathrm{VR}} = g\sqrt{N}/2\pi$ from Eq. 1.16. As the effective coupling to the atomic polarization reservoir grows, it causes faster rate of change. The slope we obtain from Fig. 5.9 is in striking agreement with our simulation: $a_{\mathrm{exp}} = 0.236 \pm 0.029\ \mu\mathrm{s}^{-1}/\mathrm{MHz}$ and $a_{\mathrm{sim}} = 0.21 \pm 0.01\ \mu\mathrm{s}^{-1}/\mathrm{MHz}$. The offsets on both the simulation and the measurements do not have quantitative nor qualitative meaning.

We would like to induce the vacuum Rabi oscillations as seen in Fig. 5.2. We can obtain larger vacuum Rabi splittings as Fig. 5.10 shows (roughly $N_{\mathrm{eff}} = 31.2 \pm 0.2$) which lead to oscillations as seen in Fig. 5.11. We have yet to understand quantitatively these results.

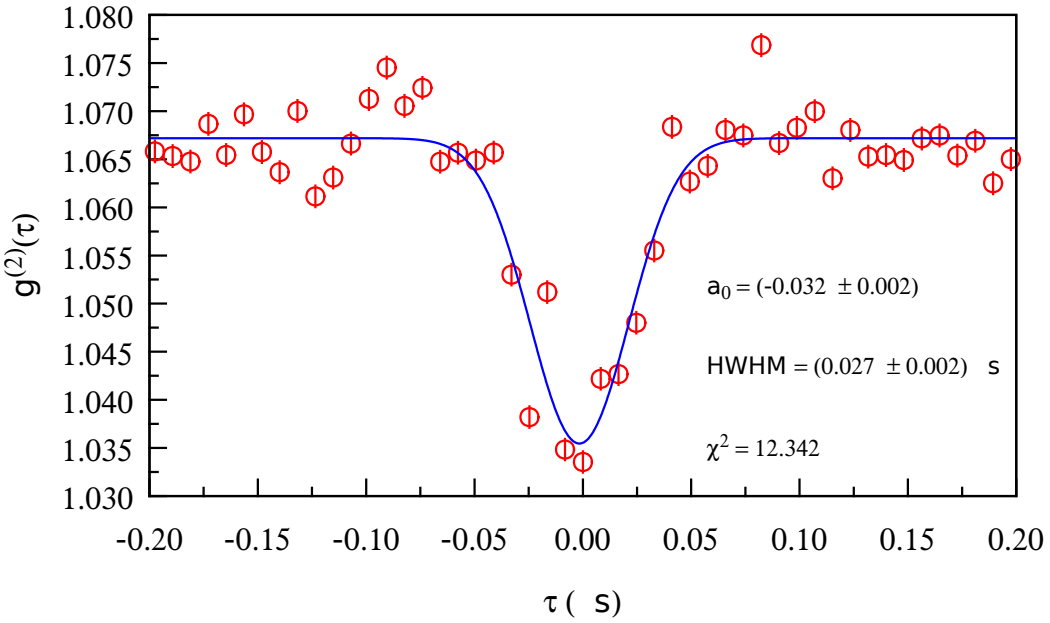

Figure 5.8: Zoomed in $g^{(2)}(\tau)$ of driven mode of cavity showing antibunching for $g\sqrt{N}/2\pi = 8.6 \pm 0.1$ MHz.

The results indicate a clear trend of enhanced evolution speed as a function $g\sqrt{N}$. This is in agreement with theoretical predictions [64] that observe a speedup as the coupling g increases in a cavity QED system. We realize this by using the coupling not to one atom but to N atoms as $g\sqrt{N}$.

5.5 Future improvements

A two-level atom realization in our geometry requires the magnetic field to point along the y direction (parallel to $\vec{k}$) and $\sigma^{\pm}$-drive. This is possible, but only in the presence of efficient optical pumping.

We intend to implement efficient optical pumping. Our trials indicate that the push MOT beam is too strong. Construction of an optical system with an axicon

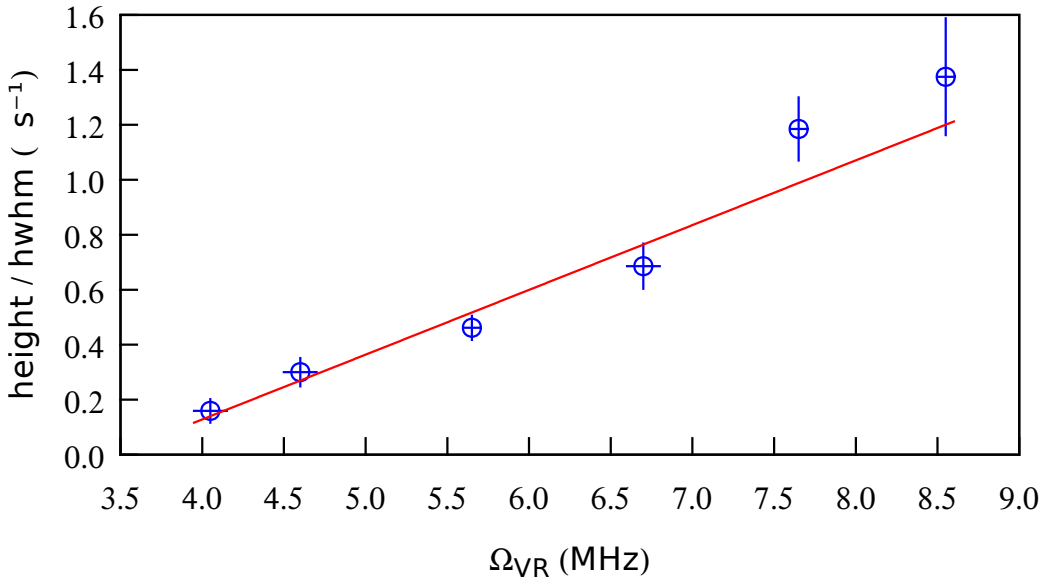

Figure 5.9: Speed-up as function of Ω_{VR}. We show a simple linear fit $y = ax + b$, with $a = 0.236 \pm 0.029$ μs^{-1}/MHz, $b = -0.8 \pm 0.2$ μs^{-1} and reduced $\chi^2 = 1.67$

lens can realize a "hollow" push MOT beam or imaging of a dark spot. We believe this would alleviate our background problem and permit our optical pumping.

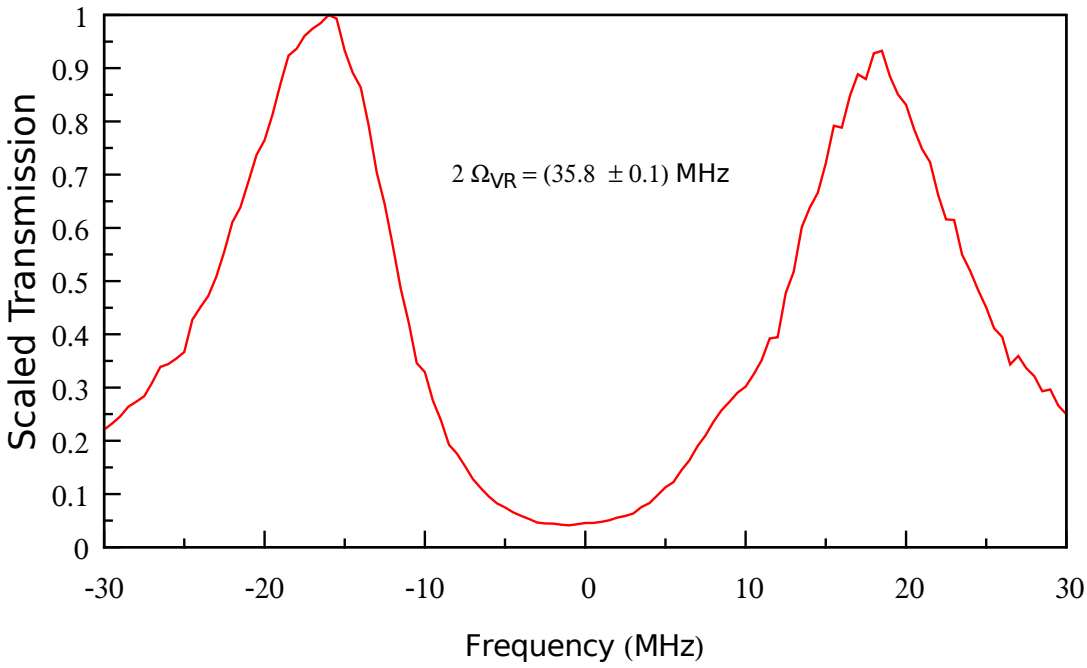

Figure 5.10: Vacuum Rabi splitting of $2g\sqrt{N}/2\pi = 35.8 \pm 0.1$ MHz. The center frequency is -7 MHz from the $|F = 3, m_F = 0\rangle \rightarrow |F' = 4, m_{F'} = 0\rangle$ atomic transition.

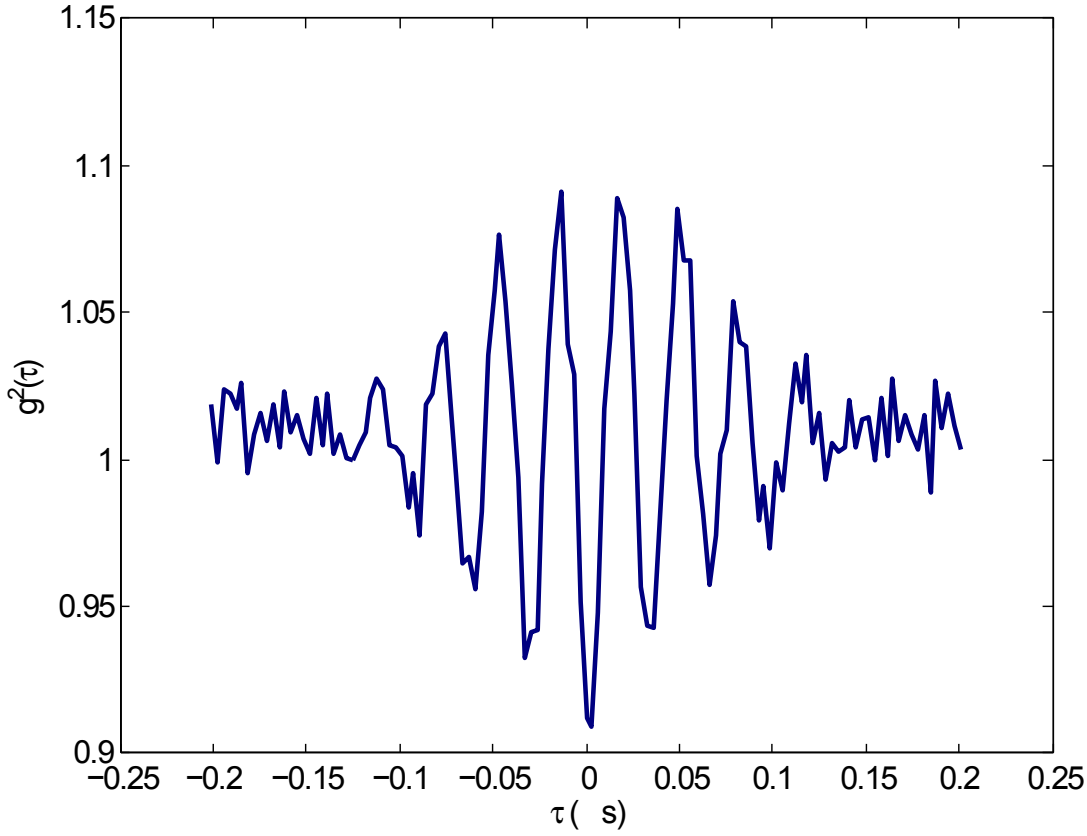

Figure 5.11: Zoomed in $g^{(2)}(\tau)$ of driven mode of cavity for large N showing anti-bunching and vacuum Rabi oscillations

Chapter 6: Conclusions

We have shown two different approaches for controlling a system consisting in an optical cavity and an ensemble of atoms. First we show control through active feedback of an atomic coherence, using the modes of the cavity as part of our detection system. On the other hand, we show preliminary measurements of the change in the fill up time of the cavity mode as a function of the number of atoms interacting with the mode of the cavity.

Our control of an atomic coherence employs a cavity as a convenient detection tool and interaction enhancer, but we manipulate the driving field to correct the subtle effects of Rayleigh scattering. We have demonstrated this by implementing a quantum feedback procedure following the detection of the photon that heralds the creation of the ground-state coherence. We turn off the drive and let the coherence evolve in the dark. In this way we avoid the quantum jumps associated with Rayleigh scattering that, although of small enough effect individually, occur sufficiently frequently to produce measurable frequency shifts and faster decoherence.

The last part of this thesis shows preliminary results on the rate of refilling of the conditional field of a cavity immediately after a photon is detected. Contrary to an empty cavity that will follow just the exponential decay and for a coherent state

will show no change in the $g^{(2)}(\tau)$ since it always has Poissonian statistics, here we use the coupling to N atoms that scales with $g\sqrt{N}$ to measure the response time.

This way of thinking about the cavity QED system, as a cavity mode coupled to a reservoir of N atoms implies that the rate at which the cavity mode can replenish has a dependence on the number of atoms it can couple to. Increasing the number of atoms brings a speed-up in the evolution of the cavity mode after a photon escapes it. We have shown, through conditional measurements that capture precisely the dynamics of the field inside the cavity, that under this weak driving regime, the field shows non-classical effects, such as anti-bunching (the field increases after the detection of a first photon). The rate of increase changes with the number of atoms.

A number of possible protocols come to mind to begin strong control of this field. Would it be possible to apply RF and/or microwave pulses to change the atomic state of the atoms? We have the antennas in the new system, but certainly the required amplitudes of the fields will be large and require careful engineering. Other alternatives include excitation from the side of the cavity using the D_1 line to also change the number of atoms interacting with the mode of the cavity. Again, the new system has the access necessary to implement this protocol.

New avenues open for strong quantum control of this simple system where one or two modes of the electromagnetic field couple to a collection of N atoms in the presence of dissipation, which allows us to probe, create, and control superposition and dynamics of an open quantum system.

Appendix A: Feedthroughs

Instructions to know which wires correspond to the coils, magnetometer, and cavity. The way the cables are organized is the following: we use color beads, each one of then corresponding to some element. For the RF coils we use as a reference the "Tee" of the chamber, specifically the feedthroughs flange. So "right" means right of the flange if looking directly at the feedthroughs (this right also coincides with the output mirror of the cavity).

1. RF coils:

    - Z axis: Black and blue beads, Yellow (A) and black (B) cables (pair 1).
    - Left: White and blue beads, Brown (C) and black (D) cables (pair 2).
    - Right: White and gray beads, Orange (E) and black (F) cables (pair 3).
    - Side: Green and gray beads, Red (G) and white (H) cables (pair 4).

2. Magnetometer:

    - Ground (GND): one green bead, Red (J) pair 5.
    - VCC: one blue bead, Black (K) pair 5.
    - SDA: one gray bead, Blue (L) pair 6.

- SCL: one white bead, Black (M) pair 6.

3. Cavity:

    - Input piezo (left): two white beads, Green (N) pair 7.
    - Output piezo (right): two blue beads, Black (P) pair 7.
    - Ground: two green beads, Red (R) pair 8.

The color / letter and pair coding corresponds to a 19-way air service cable manufactured by Accu-Glass Inc.

Bibliography

[1] Paul R. Berman, editor. *Cavity Quantum Electrodynamics.* Advances in Atomic, Molecular, and Optical Physics. Academic Press, Boston, 1994. Supplement 2.

[2] Q. A. Turchette, C. J. Hood, W. Lange, H. Mabuchi, and H. J. Kimble. Measurement of conditional phase shifts for quantum logic. *Phys. Rev. Lett.*, 75:4710, 1995.

[3] J. I. Cirac, P. Zoller, H. J. Kimble, and H. Mabuchi. Quantum state transfer and entanglement distribution among distant nodes in a quantum network. *Phys. Rev. Lett.*, 78:3221, 1997.

[4] K. M. Gheri, C. Saavedra, P. Törmä, J. I. Cirac, and P. Zoller. Entanglement engineering of one-photon wave packets using a single-atom source,. *Phys. Rev. A*, 58:R2627, 1998.

[5] T. Wilk, S. C. Webster, A. Kuhn, and G. Rempe. Single-atom single-photon quantum interface. *Science*, 317:488, 2007.

[6] D. G. Norris, L. A. Orozco, P. Barberis-Blostein, and H. J. Carmichael. Observation of ground-state quantum beats in atomic spontaneous emission. *Phys. Rev. Lett.*, 105:123602, 2010.

[7] D G Norris, E J Cahoon, and L A Orozco. Atom detection in a two-mode optical cavity with intermediate coupling: Autocorrelation studies. *Phys. Rev. A*, 80:043830, 2009.

[8] M. L. Terraciano, R. Olson Knell, D. G. Norris, J. Jing, A. Fernández, and L. A. Orozco. Photon burst detection of single atoms in an optical cavity. *Nature Phys.*, 5:480, 2009.

[9] L. S. Bishop, J. M. Chow, J. Koch, A. A. Houck, M. H. Devoret, E. Thuneberg, S. M. Girvin, and R. J. Schoelkopf. Nonlinear response of the vacuum rabi resonance. *Nature Phys.*, 5:105, 2008.

[10] C. Guerlin, J. Bernu, S. Deléglise, C. Sayrin, S. Gleyzes, S. Kuhr, M. Brune, J. M. Raimond, and S. Haroche. Progressive field-state collapse and quantum non-demolition photon counting. *Nature*, 448:889, 2007.

[11] S. Haroche and J. M. Raimond. *Exploring the Quantum: Atoms, Cavities, and Photons*. Oxford University Press, Oxford, 1 edition, 2006.

[12] M. Hennrich, A. Kuhn, and G. Rempe. Transiton from antibunching to bunching in cavity qed. *Phys. Rev. Lett.*, 94:053604, 2005.

[13] D. G. Norris, A. D. Cimmarusti, L. A. Orozco, P. Barberis-Blostein, and H. J. Carmichael. Spontaneous creation and persistence of ground-state coherence in a resonantly driven intracavity atomic ensemble. *Phys. Rev. A*, 86:053816, 2012.

[14] H. J. Carmichael, R. J. Brecha, and P. R. Rice. Quantum interference and collapse of the wavefunction in cavity QED. *Opt. Commun.*, 82:73, 1991.

[15] P. D. Drummond. Optical bistability in a radially varying mode. *IEEE J. Quant. Electron.*, QE 17:301, 1981.

[16] M. O. Scully and K. Drühl. Quantum eraser: A proposed photon correlation experiment concerning observation and 'delayed choice' in quantum mechanics. *Phys. Rev. A*, 25:2208, 1982.

[17] A. G. Zajonc. Proposed quantum-beats, quantum-eraser experiment. *Phys. Lett. A*, 96:61, 1983.

[18] H. Uys, M. J. Biercuk, A. P. VanDevender, C. Ospelkaus, D. Meiser, R. Ozeri, and J. J. Bollinger. Decoherence due to elastic rayleigh scattering. *Phys. Rev. Lett.*, 105:200401, 2010.

[19] D. G. Norris, A. D. Cimmarusti, L. A. Orozco, P. Barberis-Blostein, and H. J. Carmichael. Anomalous light shift through quantum jumps in quasiresonant rayleigh scattering. *Phys. Rev. A*, 85:021804, 2012.

[20] H. J. Carmichael. *Statistical Methods in Quantum Optics 1: Master Equations and Fokker-Planck Equations*. Springer-Verlag, Berlin, 1999.

[21] H. J. Carmichael. *Statistical Methods in Quantum Optics 2: Non-Classical Fields*. Springer, Berlin, 2008.

[22] H. M. Wiseman and G. J. Milburn. *Quantum Measurement and Control*. Cambridge University Press, Cambridge, 2009.

[23] Ivan H. Deutsch and Poul S. Jessen. Quantum control and measurement of atomic spins in polarization spectroscopy. *Opt. Commun.*, 283:681, 2010.

[24] P. Barberis-Blostein, D. G. Norris, L. A. Orozco, and H. J. Carmichael. From quantum feedback to probabilistic error correction: Manipulation of quantum beats in cavity qed. *New J. Phys.*, 12:023002, 2010.

[25] H. J. Kimble, M. Dagenais, and L. Mandel. Photon anti-bunching in resonance fluorescence. *Phys. Rev. Lett.*, 39:691, 1977.

[26] Greg A. Smith, Andrew Silberfarb, Ivan H. Deutsch, and Poul S. Jessen. Efficient quantum-state estimation by continuous weak measurement and dynamical control. *Phys. Rev. Lett.*, 97:180403, 2006.

[27] Anne E. B. Nielsen and Klaus Mølmer. Atomic spin squeezing in an optical cavity. *Phys. Rev. A*, 77:063811, 2008.

[28] W. P. Smith, J. E. Reiner, L. A. Orozco, S. Kuhr, and H. M. Wiseman. Capture and release of a conditional state of a cavity QED system by quantum feedback. *Phys. Rev. Lett.*, 89:133601, 2002.

[29] W. P. Smith and L. A. Orozco. Quantum feedback in a non-resonant cavity qed system. *J. Opt. B: Quantum Semiclass. Opt.*, 6:135, 2004.

[30] J. E. Reiner, W. P. Smith, L. A. Orozco, H. M. Wiseman, and J. Gambetta. Quantum feedback in a weakly driven cavity qed system. *Phys. Rev. A*, 70:0238119, 2004.

[31] H. M. Wiseman. Weak values, quantum trajectories, and the cavity-QED experiment on wave-particle correlation. *Phys. Rev. A*, 65:032111, 2002.

[32] G. G. Gillett, R. B. Dalton, B. P. Lanyon, M. P. Almeida, M. Barbieri, G. J. Pryde, J. L. O'Brien, K. J. Resch, S. D. Bartlett, and A. G. White. Experimental feedback control of quantum systems using weak measurements. *Phys. Rev. Lett.*, 104:080503, 2010.

[33] Kurt Jacobs. Feedback control using only quantum back-action. *New J. Phys.*, 12:043005, 2010.

[34] G. T. Foster, L. A. Orozco, H. M. Castro-Beltran, and H. J. Carmichael. Quantum state reduction and conditional time evolution of wave-particle correlations in cavity QED. *Phys. Rev. Lett.*, 85:3149, 2000.

[35] H. J. Carmichael, H. M. Castro-Beltran, G. T. Foster, and L. A. Orozco. Giant violations of classical inequalities through conditional homodyne detection of the quadrature amplitudes of light. *Phys. Rev. Lett.*, 85:1855, 2000.

[36] G. T. Foster, W. P. Smith, J. E. Reiner, and L. A. Orozco. Time-dependent electric field fluctuations at the subphoton level. *Phys. Rev. A*, 66:033807, 2002.

[37] S. Gerber, D. Rotter, L. Slodička, J. Eschner, H. J. Carmichael, and R. Blatt. Intensity-field correlation of single-atom resonance fluorescence. *Phys. Rev. Lett.*, 102(18):183601, 2009.

[38] Z. T. Lu, K. L. Corwin, M. J. Renn, M. H. Anderson, E. A. Cornell, and C. E. Wieman. Low-velocity intense source of atoms from a magneto-optical trap. *Phys. Rev. Lett.*, 77:3331, 1996.

[39] T. Wilk, S. C. Webster, H. P. Specht, G. Rempe, and A. Kuh. Polarization-controlled single photons. *Phys. Rev. Lett.*, 98:063601, 2007.

[40] B. Weber, H. P. Specht, T. Müller, J. Bochmann, M. Mücke, D. L. Moehring, and G. Rempe. Photon-photon entanglement with a single trapped atom. *Phys. Rev. Lett.*, 102:030501, 2009.

[41] C. Sayrin, I. Dotsenko, X. Zhou, B. Peaudecerf, T. Rybarczyk, S. Gleyzes, P. Rouchon, M. Mirrahimi, H. Amini, M. Brune, J. M. Raimond, and S. Haroche. Real-time quantum feedback prepares and stabilizes photon number states. *Nature*, 477:73, 2011.

[42] X. Zhou, I. Dotsenko, B. Peaudecerf, T. Rybarczyk, C. Sayrin, S. Gleyzes, J. M. Raimond, M. Brune, and S. Haroche. Field locked to a fock state by quantum feedback with single photon corrections. *Phys. Rev. Lett.*, 108:243602, 2012.

[43] Seth T. Merkel, Poul S. Jessen, and Ivan H. Deutsch. Quantum control of the hyperfine-coupled electron and nuclear spins in alkali-metal atoms. *Phys. Rev. A*, 78:023404, 2008.

[44] Brian E. Mischuck, Seth T. Merkel, and Ivan H. Deutsch. Control of inhomogeneous atomic ensembles of hyperfine qudits. *Phys. Rev. A*, 85:022302, 2012.

[45] M. L. Terraciano, R. Olson Knell, D. L. Freimund, L. A. Orozco, J. P. Clemens, and P. R. Rice. Enhanced spontaneous emission into the mode of a cavity qed system. *Opt. Lett.*, 32:982, 2007.

[46] D. G. Norris, A. D. Cimmarusti, and L. A. Orozco. Conditional control of quantum beats in a cavity qed system. *J. Phys.: Conf. Ser.*, 274:012143, 2011.

[47] Norman F. Ramsey. A molecular beam resonance method with separated oscillating fields. *Phys. Rev.*, 78:695, 1950.

[48] G. Rempe, R. J. Thompson, H. J. Kimble, and R. Lalezari. Measurement of ultralow losses in an optical interferometer. *Opt. Lett.*, 17:363, 1992.

[49] Christina J. Hood, H. J. Kimble, and Jun Ye. Characterization of high-finesse mirrors: Loss, phase shifts, and mode structure in an optical cavity. *Phys. Rev. A*, 64:033804, 2001.

[50] M. L. Terraciano. *Cross-Correlations and Entanglement in Cavity QED*. PhD thesis, U of Maryland, College Park, 2006.

[51] D. G. Norris. *Experiments in Two-mode cavity QED*. PhD thesis, U of Maryland, College Park, 2011.

[52] A. D. Cimmarusti, J. A. Crawford, D. G. Norris, and L. A. Orozco. Enhancements to cavity quantum electrodynamics system. *Rev. Mex. Fis. S*, 57:0029, 2011.

[53] A. Yariv. *Quantum Electronics*. Wiley, New York, 3rd edition, 1989.

[54] D. A. Steck. Rubidium 85 d line data http://steck.us/alkalidata, 2013.

[55] M. Tandecki, J. Zhang, R. Collister, R. Aubin, Behr J. A., E. Gomez, G. Gwinner, L. A. Orozco, and M. R. Pearson. Commissioning of the francium trapping facility at triumf. *J. Instrum.*, 8:P12006, 2013.

[56] R. W. P. Drever, J. L. Hall, F. V. Kowalski, J. Hough, G. M. Ford, A. J. Munley, and H. Ward. Laser phase and frequency stabilization using an optical resonator. *Appl. Phys. B*, 31:97, 1983.

[57] V. M. Valenzuela, S. Hamzeloui, M. Gutiérrez, and E. Gómez. Multiple isotope magneto-optical trap from a single diode laser. *J. Opt. Soc. Am. B*, 30:1205, 2013.

[58] K. L. Corwin, Z. T. Lu, C. F. Hand, R. J. Epstein, and C. E. Wieman. Frequency-stabilized diode laser with the zeeman shift in an atomic vapor. *Appl. Opt.*, 37:3295, 1998.

[59] F. Levi M. O. Tataw E. A. Donley, T. P. Heavner and S. R. Jefferts. Double-pass acousto-optic modulator system. *Rev. Sci. Instrum.*, 76:063112, 2005.

[60] S. Lloyd. Ultimate physical limits to computation. *Nature*, 406:1047, 2000.

[61] T. Caneva, M. Murphy, T. Calarco, R. Fazio, S. Montangero, V. Giovannetti, and G. E. Santoro. Optimal control at the quantum speed limit. *Phys. Rev. Lett.*, 103:240501, 2009.

[62] L. Mandelstam and I. Tamm. The uncertainty relation between energy and time in nonrelativistic quantum mechanics. *J. Phys.*, 9:249, 1945.

[63] N. Margolus and L. B. Levitin. The maximum speed of dynamical evolution. *Phys. D*, 120:188, 1998.

[64] Sebastian Deffner and Eric Lutz. Quantum speed limit for non-markovian dynamics. *Phys. Rev. Lett.*, 111:010402, 2013.

[65] A. del Campo, I. L. Egusquiza, M. B. Plenio, and S. F. Huelga. Quantum speed limits in open system dynamics. *Phys. Rev. Lett.*, 110:050403, 2013.

[66] M. M. Taddei, B. M. Escher, L. Davidovich, and R. L. de Matos Filho. Quantum speed limit for physical processes. *Phys. Rev. Lett.*, 110:050402, 2013.

[67] P. Richerme, Z.-X. Gong, A. Lee, C. Senko, J. Smith, M. Foss-Feig, S. Michalakis, A. V. Gorshkov, and C. Monroe. Non-local propagation of correlations in long-range interacting quantum systems. *arXiv:1401.5088 [quant-ph]*, 2014.

[68] K. H. Madsen, S. Ates, T. Lund-Hansen, A. Löffler, S. Reitzenstein, A. Forchel, and P. Lodahl. Observation of non-markovian dynamics of a single quantum dot in a micropillar cavity. *Phys. Rev. Lett.*, 106:233601, 2011.

[69] Sebastian Deffner. Optimal control of a qubit in an optical cavity. *arXiv:1404.3137 [quant-ph]*, 2014.

[70] H.-P. Breuer and F. Petruccione. *The Theory of Open Quantum Systems*. Oxford University Press, Oxford, 2007.

[71] R. J. Thompson, G. Rempe, and H. J. Kimble. Observation of normal-mode spliting for an atom in an optical cavity. *Phys. Rev. Lett.*, 68:1132, 1992.

[72] H. J. Carmichael and B. C. Sanders. Multiatom effects in cavity QED with atomic beams. *Phys. Rev. A*, 60:2497, 1999.